MAGNETISM AND ELECTRON TRANSPORT IN MAGNETORESISTIVE LANTHANUM CALCIUM MANGANITE

A DISSERTATION

SUBMITTED TO THE DEPARTMENT OF APPLIED PHYSICS

AND THE COMMITTEE ON GRADUATE STUDIES

OF STANFORD UNIVERSITY

IN PARTIAL FULFILLMENT OF THE REQUIREMENTS

FOR THE DEGREE OF

DOCTOR OF PHILOSOPHY

G. Jeffrey Snyder

June 1997

I certify that I have read this dissertation and that in my opinion it is fully adequate, in scope and in quality, as a dissertation for the degree of Doctor of Philosophy.

_____

Theodore H. Geballe
(Principal Adviser)

I certify that I have read this dissertation and that in my opinion it is fully adequate, in scope and in quality, as a dissertation for the degree of Doctor of Philosophy.

_____

Malcolm R. Beasley

I certify that I have read this dissertation and that in my opinion it is fully adequate, in scope and in quality, as a dissertation for the degree of Doctor of Philosophy.

_____

Robert L. White
(Materials Science Department)

Approved for the University Committee on Graduate Studies:

_____

Abstract

It is the goal of this thesis to understand the physical properties associated with the large negative magnetoresistance found in lanthanum calcium manganite. Such large magnetoresistances have been reported that this material is being considered for use as a magnetic field sensor. However, there are many variables such as temperature, magnetic field, chemical composition and processing that greatly influence the magnitude of the magnetoresistance. After introducing the problem in Chapter 1, Chapters 2 and 3 describe the materials synthesis and physical property measurements used in this work. In Chapter 4, the intrinsic magnetic and electron transport properties of lanthanum calcium manganite are distinguished from those that depend largely on the chemical synthesis and processing. Chemical substitution of lanthanum by gadolinium, discussed in Chapter 5, not only induces ferrimagnetism, but also dramatically alters the electron transport because of slight structural changes. The physical mechanisms and empirical relationships found among the resistivity, magnetoresistance and magnetism in Chapters 3 and 4 are studied in greater depth in Chapters 6 and 7 and compared with theoretical predictions. This analysis provides a useful method for predicting the magnetoresistance as a function of temperature, magnetic field and transition temperature. The related perovskite, strontium ruthenate, proves to be a model compound for the study of metallic ferromagnets. The results of this work is presented in two appendices, and compared with the manganite results throughout the text.

Preface

Looking back at the many years at Stanford, there are many people I would like to thank for helping me along the long, windy path to a Ph.D. thesis. My dad, papa Schneider, Dr. Demin, and Frank DiSalvo deserve the credit for getting me interested in science: chemistry, engineering, materials science and physics.

The graduate first year classes at Stanford would have been far too unbearable without the support of my first year commiserators Weber, Jim and Shelly. My time at the Max Planck Institute in Stuttgart, Germany could not have been more productive or pleasant thanks to Prof. Dr. Arndt Simon, the whole Abteilung Simon and foreign student ghetto especially Paul Rauch, Thomas Braun and Chris Ewels.

Having nothing to do with superconductivity, much of my work at Stanford was outside the KGB headquarters in Ginzton Lab. The materials synthesis for this project was done at the Center for Materials Research in the McCullough building. Bob Feigelson and his group deserve a special thanks for advice and use of equipment, such as the laser heated crystal growth apparatus. Some of the crystal samples used in this thesis were grown by Vlad Beffa, a Stanford undergraduate working as a CMR summer student. I would also like to thank the CMR support staff: Tracy Tingle with the SEM microprobe, Glen and Waldo for keeping up the x-ray facility, Ann Marshall for TEM studies, and Thomas Carlson and Mark Gibson for knowing how to get everything done in McCullough. I would especially like to thank Bob White, Shan Wang and their students for teaching me about magnetic and magnetoresistive materials in their group meetings.

Thanks also to the KGB group, especially Ted and Mac for helping me get started. K. A. Moler performed most of the experiment and much of the analysis of the heat capacity experiment in Appendix B. Lior Klein was the

inspiration behind the irreversibility line plot in section 3.2.2.2.9. Thanks also to Khiem, Steve, Daniel & Jenny, Laurent and the rest of the curry club for great conversations at lunch.

Much of this work was done in collaboration with Hewlett-Packard in Palo Alto. The MOCVD films of the manganites were made by Ron Hiskes and Steve DiCarolis. The XAFS studies in Chapter 5 were performed at the Stanford Linear Accelerator by Corwin Booth and Bud Bridges from U. C. Santa Cruz.

This work could not have been completed without the support of friends, housemates, parents but particularly Sossina — thank you very much.

Funding for this research was generously provided by The Fanny and John Hertz Foundation, the Air Force Office of Scientific Research, and the Stanford Center for Materials Research under the NSF-MRL program

Table of Contents

List of Figures

List of Tables

MAGNETISM AND ELECTRON TRANSPORT IN MAGNETORESISTIVE $LA_{0.67}CA_{0.33}MNO_3$

1. Introduction

The development of new materials for technological applications has opened many doors to innovation in the 20th century. New electronic and magnetic materials in particular have helped bring about the information revolution. Much of the progress is due to materials processing. Technological applications often have strict compositional and microstructural requirements for their materials. An integrated circuit for instance must have several compatible semiconductor, dielectric, and metallic materials with specific properties in precise locations. Improvements using well understood materials such as these are usually incremental.

A risky but potentially more revolutionary method for advancing technologies is to find a different materials which have inherent properties superior to those currently in use. There are many known materials which need to be better understood before it would be clear that their use would be a significant advancement. In some cases a previously unknown class of compounds (such as the cuprate superconductors) may have to be discovered. It is also important to consider other aspects of the material, such as chemical and thermal stability, toxicity and availability.

The study of new materials physics can have different emphasis. Many physicists are interested in new materials because they can be used to study a new physical phenomenon. An example of this is the study of heavy fermion metals and superconductors which have little potential application

in themselves, but the physics learned from their study may be quite useful. Conversely, one can use physics to help understand new materials for potential applications. The physics may be well established but will give valuable insight into the uses and limitations of the material. The emphasis of this dissertation is on the latter: what physics can reveal about a material as opposed to what the material can tell you about physics.

1.1 Motivation

This dissertation has been motivated by the desire to understand the basic transport and magnetic properties and the physics behind them in metallic, ferromagnetic perovskite oxides. The manganites in particular show a wealth of complex properties. It has been useful to characterize these properties as either common to ferromagnetic metals in general or unique to the manganites. For this reason, the study of $SrRuO_3$ has been quite useful in understanding the properties of the manganites. For example, $SrRuO_3$ and the manganites shows similar magnetic critical behavior and low temperature magnetic excitations. It has also been advantageous to further classify the properties of the manganites as those which are intrinsic to the material and those affected by processing. The physics of the intrinsic properties are easier to study, while the extrinsic properties can be easily modified. Once the inherent properties of the material are understood, properties which depend strongly on processing can then be tuned for used in a device with particular characteristics.

In this chapter some background on the manganites is presented, focusing in the recent interest in "Colossal magnetoresistance" (CMR). Chapter 2 briefly summarizes the materials synthesis and characterization. In chapter 3 the magnetism and transport experimental procedures are given as well as the pertinent analysis and theory. In chapter 4 the results of the intrinsic electrical and magnetic properties of $La_{0.67}Ca_{0.33}MnO_3$ are presented. In chapter 5 the ferrimagnetism and structure-transport correlations are shown

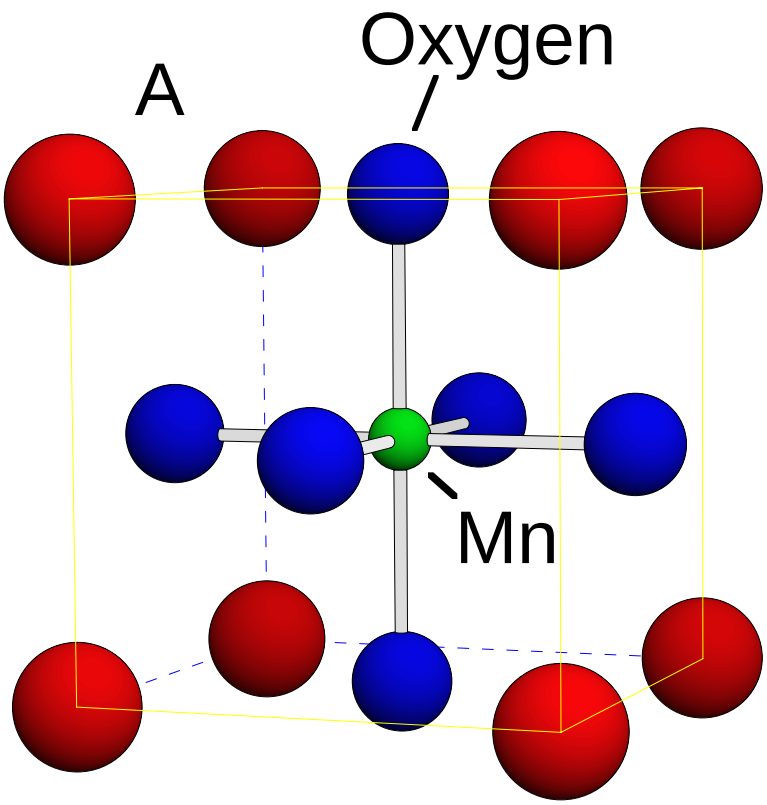

Figure 1-1 The Perovskite structure $AMnO_3$ where A is a mixture of rare earth and alkaline earth elements *e.g.* $La_{0.67}Ca_{0.33}$.

for the related compound $Gd_{0.67}Ca_{0.33}MnO_3$. Chapter 6 introduces the magnetoconductivity analysis of the magnetotransport phenomena studied here. In Chapter 7 this analysis is used to examine the relationship bewteen the magnetization and the magnetoresistance.

1.2 $AMnO_3$

The $R_{1-x}A_xMnO_3$ perovskite manganites, where R and A are some rare earth and alkaline earth elements respectively and $0.2 < x < 0.5$, display the unusual property of being paramagnetic insulators at high temperatures and ferromagnetic metals at low temperatures [1-4]. Perovskite is the name of the structure type, Figure 1-1, containing corner sharing MnO_6 octahedra. Both end members of $La_{1-x}A_xMnO_3$ are antiferromagnetic insulators [5], but become

ferromagnetic metals upon doping. The theory of double exchange [6-8], described in section 1.3, has been developed in order to explain this phenomenon and correctly predicts $x = 1/3$ to be optimal doping [9]. Recent calculations show that a second mechanism such as a Jahn-Teller distortion may be required to explain the magnetoresistance within the double exchange model [10-12].

Until recently, much of the experimental work on the manganites has been motivated by their utility as a cathode materials in solid oxide fuel cells [13]. Thus many compounds of the type $R_{1-x}A_xMnO_{3+\delta}$ have been studied in polycrystalline form [14-17]. Much has been learned about their defect chemistry and high temperature electronic and ionic conductivity. Most of these compounds are not metallic above room temperature but have electronic conductivity, presumably due to (small) polaron hopping, sufficient to make good electrodes.

Interest in the perovskite manganites has expanded since their fabrication as epitaxial thin films [18, 19]. Some films have shown the insulator to ferromagnetic metal transition at lower temperatures with a large magnetoresistance near this transition [20, 21]. $\Delta R/R(H)$ of greater than $10^6\%$ has been reported for fields of several Tesla [22-25]. Since Giant Magneto Resistance (GMR) films have a $\Delta R/R(H)$ of typically 20% (which saturates in a few thousand Oersted), the manganite films have been proposed as possible replacements for GMR read heads in the magnetic recording industry. However, since magnetic recording devices work at room temperature with low magnetic fields, the temperature range and field sensitivity of the manganites in their present state do not make them competitive with GMR materials. Nevertheless, the rather imprecise term "Colossal Magneto Resistance" (CMR) has been coined for this phenomenon.* However, since it

* It should be noted however, that such a large magnetoresistance is not

has been widely adopted it will be employed it here where CMR is defined as $\Delta R/R(H) > 10$. CMR materials often refers to all manganite perovskites.

Although the films are quite stable and the measurements reproducible even after several months, it is clear that growth and annealing conditions greatly influence the properties of the manganite films [27]. Furthermore, the electrical and magnetic properties of the CMR films are often very different than those of the materials produced by bulk ceramic techniques or single crystals with the same nominal composition. Thus, in order to understand these materials, one should distinguish between the properties intrinsic to perfect crystalline $R_{1-x}A_xMnO_3$ and those caused by microstructure, strain, disorder and/or compositional variations.

From the work described in chapter 4, it is concluded that the low temperature, CMR phenomenon is not intrinsic to the thermodynamically stable phases with composition $La_{0.67}Sr_{0.33}MnO_3$ or $La_{0.67}Ca_{0.33}MnO_3$.

In chapter 5 the effect of the rare earth magnetism is shown for the case R = Gd in $Gd_{0.67}Ca_{0.33}MnO_3$. The possibility of structural distortions at T_C are considered for this compound.

1.3 Double Exchange

The theory of double exchange is concerned with the exchange process involving *d*-band carriers in a mixed valent oxides. First postulated by Zener [6] to explain the properties of $(La^{3+}_{1-x}A^{2+}_x)(Mn^{3+}_{1-x}Mn^{4+}_x)O_3$ [1, 2, 4], the theory of double exchange was formulated by Anderson and Hasegawa [7] and DeGennes [8]. The compounds at the two ends of the series are

---

unique to the manganates. Doped EuO and EuS show magnetoresistances of 10^4%, using the above definition, and therefore can be considered a CMR material. Furthermore, it has been shown that in some Chevrel phase compounds [26], a magnetic field makes the material superconducting - which would make them "super-magnetoresistance" (SMR) materials.

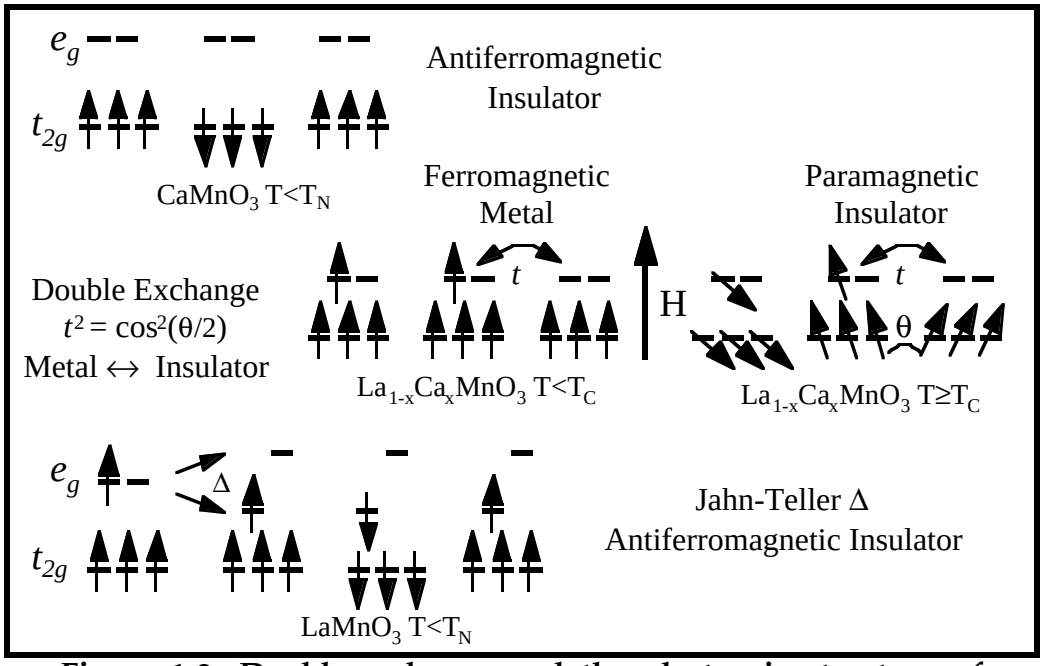

Figure 1-2 Double exchange and the electronic structure of $AMnO_3$.

antiferromagnetic insulators. For x near 1/3, the compounds become ferromagnetic and metallic below the Curie temperature. This correlation can be qualitatively explained with the theory of double exchange.

For $x = 1$, the insulating properties can be understood assuming a very large Hund's rule, exchange splitting, which is about 3 eV [28]. The $x = 1$ compounds ($CaMnO_3$ for example) contain entirely Mn^{4+} which has 3 d electrons. For a transition metal in an octahedral environment, as is the case in the perovskites, the five degenerate d orbitals are split into a low energy, triply degenerate t_{2g} set and a higher energy, doubly degenerate e_g set (Figure 1-2). The t_{2g} and the e_g orbitals are split by the crystal or ligand field (by about 5eV), while the spin-up and the spin-down halves are split by the exchange energy (> 5eV). The three Mn^{4+} d electrons entirely fill the spin-up t_{2g} orbitals while leaving the e_g and the spin-down t_{2g} orbitals entirely empty. For large enough crystal-field and exchange splittings, there is no overlap with the occupied spin-down t_{2g} band, and the material is expected to be an insulator.

For $x = 0$, the situation is slightly more complex. Most reports claim that stoichiometric $LaMnO_3$ is an antiferromagnet insulator [29]. It is apparently difficult to prepare stoichiometric $LaMnO_3$ which likes to lose oxygen or be rich in lanthanum. Off-stoichiometric $LaMnO_3$ will contain mixed-valent manganese and could then be metallic and ferromagnetic. Stoichiometric $LaMnO_3$ contains entirely Mn^{3+} which has 4 d electrons. The first 3 fill the spin-up t_{2g} band, as in $CaMnO_3$, while the remaining electron half-fills the spin-up e_g band. The e_g band is apparently further split, resulting in an insulator. There are several ways the band could be split, any or all of which may be the cause of the insulating behavior. First of all, a half-filled band is susceptible to splitting due to the Mott correlation effect – producing a Mott insulator. Secondly, the structure is not entirely cubic particularly for the end members. Such a distortion raises the degeneracy of the t_{2g} and e_g orbitals. This is known as a Jahn-Teller splitting. Finally, the unit cell relevant to the electronic structure may be doubled, which will split the e_g band in half. The magnetic structure, by virtue of the antiferromagnetism, has a doubled cell, which may affect the electronic structure.

At finite values of x there will be x holes (or 1 - x electrons) in the spin-up e_g band. These holes should be free to move and provide a large conductivity. If, however, the intra-atomic exchange, which holds the spins of all the d electrons on a given ion parallel, is stronger than the "hopping integral," then the hopping can only take place between pairs of ions on which the t_{2g} spins (Mn^{4+} core) are parallel. Otherwise the two sites have different energies. The difference in energy is proportional to $-\cos(\theta/2)$, where θ is the angle between the neighboring core spins. Since free carriers gain kinetic energy by being itinerant, this provides a type of exchange mechanism which holds the two core spins parallel. Conversely, the more parallel the core spins are aligned, the easier it is for the carriers to become itinerant. Since a magnetic field has a large effect of aligning ferromagnetically coupled magnetic spins

near T_C (magnetic susceptibility becomes large), the application of a magnetic field should increase the conductivity near T_C. This gives a simple qualitative explanation for the large negative magnetoresistance observed near T_C.

It has been suggested the double exchange mechanism alone cannot provide such a large effect on the resistance [10]. It is proposed, that the electron-phonon coupling which localizes the conduction electrons as polarons at $T > T_C$, augments the double exchange mechanism to provide the observed effects [11, 12]. This conclusion is not universally accepted [9, 30-32].

The polaronic mechanism alone may account for similarly large magnetoresistance in ferromagnetic semiconductors [30, 33, 34]. The stable state of a electron donor in a ferromagnetic semiconductor can abruptly shift from being a shallow to a deep donor as the temperature is raised toward T_C. The increasing spin disorder destabilizes the large-radius donor, which collapses into a well localized small-polaronic donor. The electron-lattice interaction plays a pivotal role in this phenomenon. The magneto-resistance arises because the temperature of the donor-state collapse and the accompanying metal-insulator transition are increased by the application of a magnetic field. Other explanations for magnetoresistance in ferromagnetic materials are discussed in chapter 6.

When superexchange is of comparable magnitude to the double exchange, a canted antiferromagnetic ground state is expected. This is because superexchange favors an antiferromagnetic ground state with energy proportional to $\cos(\theta)$ while the double exchange is proportional to $-\cos(\theta/2)$. The minimum of these two energies is in general some $\theta \neq 0$ [8].

2. Materials Synthesis and Characterization

In order to find or understand new physical phenomena, samples for measurement need to be made. The advantage of a materials physicist who is also a materials chemist is that he/she has more control over the material. There are many synthetic details which may effect the properties. Also, being able to make one's samples makes it much easier to chose what materials to study and get the research started rapidly. A materials chemist who is also a materials physicist understands what properties of the material is of interest and what measurements are simple enough to characterize the samples so that chemical improvements can be made efficiently and effectively.

2.1 Sample Preparation

Sample preparation is sometimes viewed as a black art, or as simple as making breakfast. Indeed some materials require an immense amount of time and equipment. However, both of these requirements can be limited if the sample requirements are not too stringent. Much time and effort can be saved if the type of sample made just exceeds the sample requirements. Bulk polycrystalline samples are usually quite easy to make while growing crystals is more risky and time consuming [35]. When looking for isotropic properties, polycrystalline samples usually suffice.

2.1.1 Bulk Polycrystalline Samples

The most widely used method for preparing polycrystalline oxides is the direct reaction, in the solid state, of a mixture of solid starting materials. Powder solids are formed which can then be pressed and sintered to form dense polycrystalline pellets. Even though the desired phase is thermodynamically favored, solids do not usually react together at ambient temperature over laboratory time scales and it is necessary to heat the reactants at high temperatures to overcome the kinetic barriers. For such

reactions, the rate limiting step is usually the solid state diffusion of the cations across the interface between the starting materials. In order to supply sufficient thermal energy to enable the ions to jump out of their normal lattice sites and diffuse through the crystal, high temperatures usually greater than 1000°C are required. Even at these temperatures, diffusion lengths are usually quite short. To facilitate this process, the starting materials are usually ground to a fine powder, which both decreases the length the ions must travel and increases the surface area for reaction. The powders are often pressed into a pellet before heating to increase the contact between particles. Reaction times are usually several days and it is best to repeat the process to insure homogeneous samples.

Starting materials are usually single cation oxides, carbonates, nitrates or hydroxides — materials which decompose to form oxides when heated. Carbonates are popular for the alkali and alkaline earth elements because they are not hydroscopic and therefore can be weighed accurately in air. On the initial heating or calcination of carbonate containing mixtures, carbon dioxide is produced and escapes from the solid. This prevents good sintering of the material into a dense ceramic, requiring an additional heating.

At such high temperatures, the reactivity of the crucible material must be considered. Common crucible materials for high temperature reactions are alumina, zirconia, magnesium oxide and platinum. These materials may contain other impurities to help in their processing. So, contamination of the desired product by the crucible may not necessarily be by Al, Zr, or Mg.

2.1.2 Single Crystals

Many measurements of materials properties are easier to interpret if single crystal samples are used. Transport measurements, which require a contiguous transport pathway across the sample, can therefore be greatly influenced by the presence of grain boundaries, interfacial impurity phases and voids which obstruct or alter the paths. For instance, an impurity phase

(of too little volume fraction to detect by many of the characterization techniques described in section 2.2) located in the grain boundaries may unknowingly dominate the resistivity.

Furthermore, many properties of interest are tensorial in nature and therefore have some degree of anisotropy. The properties of polycrystalline samples are artificially isotropic due to the random orientation of the crystallites. This may give a easy way to measure the average property of a material but may be misleading in two ways. First, the physics of the material may depend largely on the anisotropy. For example, some materials such as graphite are metallic in one direction and insulating in another. Secondly, for practical applications most anisotropic materials experience some kind of orientation during the materials processing *e.g.* rolling, extruding, thin film deposition. Thus, the properties of the final product may strongly depend on the processing, because of the anisotropy.

2.1.2.1 Flux Growth

The use of a homogeneous, amorphous solution may greatly facilitate formation of the crystalline product, since convection not diffusion will transport the ions, and the product will form at much lower temperatures than by solid state reaction. Flux growth can also sometimes yield metastable phases which are difficult or impossible to prepare by other means. The solvent or flux can be any material which dissolves and precipitates the desired material (solute). At the beginning of the crystal growth, the solute is entirely dissolved in the solvent. The solubility of the solute in the solvent is then decreased (usually by decreasing the temperature), causing crystals to nucleate and grow. Knowledge of the solute-solvent phase diagram will help determine appropriate concentrations and temperature ranges for crystal growth. The cooling rate and temperature gradient regulate the number and size of the crystals grown. If a gaseous transporting agent is used (vapor phase transport), the crystals will not have to be physically separated from the flux.

Otherwise one has to seriously consider how to remove the solvent after the crystals are grown. One should also be aware of possible contamination in the crystal by the flux or crucible material.

For instance, crystals of $SrRuO_3$ and $CaRuO_3$ can be grown from $SrCl_2$ or $CaCl_2$ molten salts respectively [36]. The magnetic properties of such $SrRuO_3$ crystals is described in Appendix A. During some of the growths, crystals with very different morphologies were found. Microprobe analysis showed significant platinum contamination in these crystals, presumably from the crucible. The Pt containing crystals from the $SrRuO_3$ growth were pyramidal and paramagnetic not ferromagnetic.

The Pt containing crystals from the $CaRuO_3$ (denoted "$CaRu/PtO_3$") had cubooctahedral or rhombohedral morphologies. X-ray diffraction of selected single $CaRu/PtO_3$ crystals had a perovskite unit cell. X-ray diffraction of powdered crystals showed both perovskite and possibly $Ca_4(Ru/Pt)O_6$ [37]. This different phase was discovered also from an attempted crystal growth with $CaCl_2$ in a Pt crucible.

2.1.2.2 Float Zone

Congruently melting compounds (materials which melt before decomposing) are ideal for float zone crystal growth. In this method no flux or crucible is used, preventing possible contamination problems. A polycrystalline source rod is made stoichiometricly. A molten zone then slowly moves down the rod. The molten zone is small enough that the surface tension of the liquid keeps it suspended between the two solid sections. The composition can be adjusted for growing non-congruently melting compounds. In this case, the traveling molten zone would have a composition different (perhaps containing a flux) from the desired material. The system used for the work reported here, uses a CO_2 laser focused to about $1mm^2$ to heat the molten zone.

2.1.2.3 Thin Films

Related to vapor growth, is the growth of thin films. Thin films are easy to manipulate and therefore can be much more useful to electronics technologies than single crystals. The transport of the material to the substrate usually takes place in the gas phase or a vacuum. Once the atoms or molecules hit the substrate they diffuse only until they lose energy and are incorporated into the solid film. These atoms have a relatively short time to grow crystals and cannot usually return to the vapor phase. This is in contrast to standard crystal growth which relies on the solid-fluid equilibrium to grow single crystals. Nevertheless, single crystal films can be grown when the substrate is itself a single crystal.

The various thin film deposition techniques differ primarily by the way the material is transported and how it gets into the vapor phase. The most common methods used in research transport the material in a vacuum or low pressure gas. The atoms, ions, or small inorganic molecules are ejected into the gas phase by evaporation, sputtering or laser ablation of a target. Chemical vapor deposition uses volatile precursors which can easily be transported in the gas phase to the hot substrate where they decompose to make the film. Many of the films used in this work were produced using solid-source MOCVD. In this case, a solid organometallic compound is evaporated, transported in the vapor phase to the substrate where it decomposes to form the film. Oxide films can also be produced by first spin-coating a sol-gel mixture of the desired metal stoichiometry. During heating, the sol-gel decomposes and crystallizes to form the film.

2.1.3 Reactive Samples

Many compounds react with water, oxygen or nitrogen present in air. Materials such as the subnitrides of barium [38, 39] or alkali intercalated C_{60} [40] decompose rapidly in air. Thus the synthesis and analysis of these materials is much more complicated since it must be done in an inert

atmosphere or vacuum. A glove box or Schlenck apparatus allows the manipulation of samples in an inert (usually argon gas) atmosphere. Samples can then be sealed in glass for analysis.

Even if the sample is reasonably stable in air at room temperature, almost all non-oxides will react with oxygen if heated to high temperatures. Thus compounds such as sulfides [41, 42] or nitrides [43] must be sealed in glass before heating to solid-state diffusion temperatures.

2.2 Characterization

2.2.1 Elemental Analysis

There are various ways to confirm or measure the elemental composition of a sample. Most of these methods utilize properties of the core electrons or nuclei and tend to be insensitive to the light elements. For elements heavier than neon, there exists several accurate and common procedures: The electron microprobe detects characteristic X-rays produced after excitation by an electron beam in an electron microscope. The characteristic light emission or absorption of gaseous elemental species can be used for elemental analysis – one common method uses an inductively coupled plasma (ICP). Rutherford back scattering (RBS) detects the weight and depth of atoms by elastic scattering of alpha particles off their nuclei. X-ray diffraction can in principle be used for elemental analysis since it gives essentially an electron density map. Wet chemical methods such as iodometric titration can be used to measure the oxidation state of individual elemental species, allowing the inference of the oxygen stoichiometry.

2.2.2 Structural Analysis

The physical properties of a material may depend as much on the structure as the elemental composition: graphite is quite different from diamond. The regular periodic structure can be determined from the elastic scattering of neutrons or X-rays. Wavelengths approximately equal to the

interatomic spacings (measured in Å) are needed. Synchrotron and neutron sources usually have tunable wavelengths as well as high intensity. For many purposes, however, laboratory scale X-ray diffraction is often adequate.

2.2.2.1 Neutron diffraction

Neutrons, having a magnetic moment, are sensitive to the magnetic structure as well as the atomic structure. For example, an antiferromagnet which has a larger magnetic unit cell than the atomic cell, will cause extra neutron diffraction peaks not seen in X-ray diffraction. Polarized neutrons are also sensitive to the orientation of these magnetic moments. Since magnetic measurements only give the net moment, which is often zero for an antiferromagnet, neutron diffraction is far superior in determining magnetic structures. Inelastic neutron diffraction can provide further information concerning the structure dynamics. For instance phonon and magnon (spin wave) dispersions can be measured.

2.2.2.2 X-ray diffraction

X-ray diffraction (XRD) can be used both to quickly determine which phases are present in an unknown sample and to perform a detailed structural investigation. The difference lies more in the sample preparation and data analysis than the measurement apparatus. Although synchrotron source x-ray diffraction experiments are quicker, much of what is desired can be learned from a standard laboratory experiment.

X-rays scatter off the periodic arrays of atoms in a crystal lattice. The scattered x-rays produce a pattern unique for a particular substance. This pattern can be used for either phase identification or it can be analyzed to determine the position of the atoms in the cell. The orientation of the crystal with respect to the incoming x-rays determines the orientation of the diffracted x-rays. So, either a single crystal must be precisely oriented to detect

a particular diffraction peak, or many crystallites randomly oriented can be used to get an orientation independent response.

2.2.2.2.1 Powder X-ray diffraction

In powder x-ray diffraction, the sample consists of many small crystallites which are assumed to be randomly oriented. This produces rings of diffracted x-rays, defined by the angle between the incident and diffracted beams, 2θ. The diffraction condition is determined by the atomic unit cell. In this way, the structure type of a material and unit cell size can easily be determined. If more than one type of material is present, the diffraction pattern will be a superposition of each of the components. If only phase identification is desired, this often provides enough information. Reference [40] gives a good example of how this is done.

The intensities of each diffraction line is determined by the atomic constituents, and their placement in the unit cell. In principle, both of these can be determined from the intensities. In practice, this is difficult to achieve. A primary concern is texturing, or preferred orientation of the crystallites. If the crystallites are plate or needle like, they will tend to lay in the sample holder in a non-random orientation. This will cause a variation in the intensities. Also, individual diffraction peaks often overlap one another in a powder pattern. Since the determination of the structure depends on how much intensity is associated with each peak, having overlapping peaks complicates the solution process. It is often easiest to do structural analyses on single crystal samples.

Powder diffraction sample holders are usually for flat, planar samples. If the incident angle of the incoming x-rays with respect to the sample plane is equal that of the diffracted beam being detected, the x-ray beam is partially focused (Bragg-Botano parafocusing) to give a narrower diffraction peak. For this reason, the sample plane is usually rotated (by an angle $\omega = \theta$) as the

detector rotates (by angle 2θ). Plate-like crystallites can be highly oriented in such a sample holder. The Guinier method utilizes a different focusing technique for samples placed in a capillary tube. This is ideal for air sensitive samples which can be easily sealed in a tube. Needle like crystallites are easily oriented when placed in a tube.

2.2.2.2.2 Single crystal and films

Single crystals diffract an x-ray beam to produce spots as opposed to line. A particular spot appears only when the crystal is in a particular orientation. For this reason, three additional angles are used to orient the crystal. If the crystal is very large, it will absorb much of the x-ray intensity. Small crystals, about 0.2mm diameter, are usually used for structure determination since they absorb little and have a constant volume of sample in the x-ray beam at all time. The crystal can be rotated and the intensity of each diffraction spot measured. This usually provides enough data so that the independent data to free parameters ratio is about 10. Examples of structure determinations using single crystal x-ray diffraction can be found in [38, 39, 41, 42, 44-48]. If there are many smaller crystals in the x-ray beam, they can be effectively ignored by measuring x-ray intensity only at positions where a diffraction peak from the larger crystal is expected. This technique is used in [38, 39, 45, 46].

Single crystal films also produce diffraction spots as opposed to lines. However, the intensities are small compared to those from the substrate. It is usually only possible (and only of interest) to determine film's unit cell size, orientation and texturing. The difference in cell size of the film compared to a bulk sample gives an indication of the strain on the film.

2.2.2.3 X-ray Absorption Fine Structure

X-ray Absorption Fine Structure (XAFS) gives essentially the pair distribution function of atoms around a particular element in the sample.

Thus XAFS probes the local structure, as compared to X-ray diffraction which gives average structure over hundreds of angstroms.

X-ray absorption spectra in this study were collected by Corwin Booth and Bud Bridges from U. C. Santa Cruz in transmission mode on beam line 4-3 at the Stanford Synchrotron Radiation Laboratory (SSRL) using powder samples (grain size less than 30μm). The sample temperature was regulated using an Oxford helium cryostat system within 0.1 K (absolute temperature may be as much as 2 K warmer). Data for this experiment were collected above and below T_C, at T=69 K and T=40 K. Data reduction and analysis followed standard procedures reported previously [49].

3. Electronic and Magnetic Measurements

3.1 Transport Properties

Transport properties: Resistivity, dielectric constant, thermalconductivity, thermopower, Hall effect, etc. are often a prime concern when engineering a new material for a particular use. Even if the purpose of the material is not related to transport, the material may still be required to have certain transport characteristics. For example, the liquid crystal in a liquid crystal display should have a low electrical conductivity to minimize resistive losses.

3.1.1.1 Ohm's Law

Most materials, whether metals, semiconductors or insulators, obey Ohm's law to a good extent: the current I flowing in a wire is proportional to the potential drop V along the wire $V = IR$ (linear response). R is the resistance of the wire and it depends on the size and shape of the wire. One generally prefers to use intensive quantities to characterize a material. Thus Ohm's law can be used to define the resistivity ρ which is defined to be the proportionality constant between the electric field $\mathbf{E}$ and the current density $\mathbf{j}$ that it induces: $\mathbf{E} = \rho\mathbf{j}$. Since $\mathbf{E}$ and $\mathbf{j}$ are vectors, ρ is a second order tensor. Any deviations of Ohm's law can be easily described by adding terms with higher powers of $\mathbf{j}$. The conductivity σ is the inverse of the resistivity ($\sigma = \rho^{-1}$) such that $\mathbf{j} = \sigma\mathbf{E}$. In an isotropic or cubic substance the resistivity tensor ρ has off diagonal elements equal to zero and three equal diagonal elements ρ (a scalar), then the conductivity tensor σ has the same form with diagonal elements σ where $\sigma = 1/\rho$. For an orthorhombic substance (for which ρ and σ have no nonzero off diagonal terms in the appropriate coordinate system), the conductivity along a principle direction is equal to the inverse of the resistivity along the same principle direction. Because of these simple

relationships resistivity and conductivity are commonly described as if they were scalars. Some other properties of the conductivity and resistivity tensors are described in section 6.2.1.

3.1.1.2 Magnetoresistance

Magnetoresistance is simply the change in resistivity as the magnetic field is applied. For nonmagnetic metals, the magnetoresistance ratio $\Delta R/R$ is only a few percent in large ~1Tesla fields. For symmetry reasons discussed in section 6.2.1, the magnetoresistance is proportional to H^2 for small H in these metals. Since this magnetoresistance arises from the complicated orbits of the electrons on the Fermi surface, the magnetoresistance has large crystallographic anisotropy.

Even in an isotropic conductor, there exists two possible configurations for magnetoresistance. When the current is parallel to the applied magnetic field the longitudinal magnetoresistance is measured. If the magnetic field is perpendicular to the current path, then the transverse magnetoresistance is being measured.

If the material itself is not isotropic, different crystallographic orientations will have distinct longitudinal and transverse magnetoresistances. For example, a cubic material grown as a thin film may have growth induced crystallographic anisotropy. Since for practical purposes, the current is usually constrained to the plane of the film, there are three easily reportable magnetoresistances: longitudinal and transverse magnetoresistance with both the current and magnetic in the plane of the film, and transverse magnetoresistance with the magnetic field perpendicular to the film. The two different magnetic field orientations will also affect the demagnetization field and domain size and motion which must be taken into account.

Magnetoresistance that is actually proportional to the magnetization rather than the magnetic field is called anisotropic magnetoresistance (AMR). In low fields, the magnitude of M does not change, only the orientation. If M

is aligned parallel (or antiparallel) to the current, the resistance is different than if M were perpendicular to the current. This difference is the anisotropic magnetoresistance. AMR in $La_{0.67}Ca_{0.33}MnO_3$ will be discussed further in sections 6.1.

3.1.1.3 Drift velocity, mobility, relaxation time and mean free path

It is often useful to think of transport in terms of particles moving with an average velocity in a field because of collisions with the surroundings. Some of the basic relationships are given below for electrical conductivity, and can be easily generalized for other transport phenomena. The electrical current **j** (charge per cross-sectional area per time) is related to the number density of carriers n, the charge of each carrier $-e$ (for electrons), and the average drift velocity **v**.

$$\mathbf{j} = -ne\mathbf{v}.$$

The drift mobility μ (a tensor like the conductivity) is defined by the relationship between the drift velocity and the electric field **E**.

$$\mathbf{v} = \mu\mathbf{E}$$

Thus the conductivity is proportional to the number of carriers and their mobility

$$\sigma = -ne\mu$$

The relaxation time can also be used to relate the drift velocity and the electric field. The electric force accelerates the carrier, of mass m, for an average time τ between collisions (the relaxation time) to provide the drift velocity.

$$\mathbf{v} = \frac{-e\tau}{m}\mathbf{E} \text{ so } \sigma = \frac{ne^2\tau}{m}$$

The mean free path l, the average distance the carrier travels between collisions, is a useful quantity. If the mean free path is smaller than the interatomic spacing a, then clearly a model based on atomic collisions is

inadequate. $l \approx a$ is known as the Ioffe-Regel limit. To calculate l, the average speed (not velocity) must be known. Unfortunately, this is the Fermi velocity which depends strongly on the band structure. For an electron gas of density n with a spherical Fermi surface, the Fermi velocity v_F is

$$v_F \approx 3.09\frac{\hbar}{m}\sqrt[3]{n} \text{ so that } l \approx 3.09\frac{\hbar}{e^2}\frac{\sigma}{n^{2/3}}.$$

3.1.1.4 Hall effects

The Hall effect is the transverse electric field that is produced by the presence of a magnetic field perpendicular to the flow of charged carriers. This can be described by antisymmetric off diagonal terms in the resistivity tensor which are a function of the magnetic field. The Hall effect is normally linear with respect to an applied field. For an isotropic substance $E_y = j_x R_H H$, where H is the magnetic field, j_x is the current along the x direction and E_y is the transverse electric field. R_H is known as the Hall coefficient. An internal magnetic field due to a nonzero magnetization of the material may cause a Hall effect. This anomalous Hall effect is proportional to the internal magnetization M, $E_y = j_x R_A M$. The angle between **E** and **j** caused by the Hall effect is known as the Hall angle.

For simple metals and semiconductors, the Hall effect (combined with other data) can reveal the sign and density of the charge carriers. The Hall coefficient for an electron gas is $-1/nec$. If there is more than one type of carrier, the Hall effect is the weighted average of the Hall effect of the individual carriers and becomes nonlinear in H. This nonlinearity can be used to determine the sign and density of the individual carriers – assuming field independent mobilities and Hall coefficients for each carrier type [50].

3.1.2 Measurement

The primary concern for reliable transport measurements of new materials is the identification and elimination of systematic errors. Thermal and electrical noise lower the precision but usually not to an important extent

when characterizing new materials. The danger is finding a new effect or result that is reproducible but none the less spurious. Since measurements of new materials have usually not been previously performed, it is often impossible to compare with previous results. Some considerations and solutions are outlined below.

3.1.2.1 Linearity

Most transport measurements assume some sort of linear response. Conductivity measurements assume I is linearly proportional to V. Experimentally this is never exactly true. A test for linearity should always be made before measuring a new sample. The resistance over several orders of magnitude should be constant within a few percent. Even if I *vs.* V is linear, thermal or contact voltages usually add a nonzero offset voltage V_0 so that $V = IR + V_0$. Using wires from the same spool, pure copper contacts and shielding may help but will not totally eliminate V_0. This offset voltage is easily subtracted. The easiest method is by measuring the voltage at I and $-I$. The resistance is then $R(I) = (V(I) - V(-I))/2$. The best method is to take a full I *vs.* V curve and measure the slope. This may take more time and therefore introduce other errors such as those caused by temperature drift. The current range used for measurement should be well within the Ohmic regime. A current too small may have V_0 comparable to V; it is best not to rely heavily on the subtraction of V_0. Large currents may produce I^2R heating of the sample, in which case the measured resistance should look like it has an additive term proportional to I^2. AC measurements are ideal for extracting only the linear response; in this case, the frequency dependence should also be checked, and compared to the DC value.

Thermopower S measurements similarly assume the linearity of the voltage with the temperature difference: $V = S\Delta T$. These measurements also, however, have an offset voltage V_0 that should be subtracted.

Hall effect measurements have several assumptions which need to be considered. First, since it is basically a resistance measurement, the *I vs. V* curve should be checked and V_0 subtracted as above. Second, it is often assumed that the Hall voltage is linear in the applied magnetic field $E_y = j_x R_H H$. This is often not the case, as described above (section 3.1.1.4) for magnetic materials or semiconductors with more than one type of carrier. Finally, the effect of the magnetoresistance needs to be subtracted. Traditionally, and theoretically this can be done by balancing the Hall voltage so that it reads zero at $H = 0$, and then the magnetoresistance should also be subtracted for $H \neq 0$. In practice, this does not work. There is usually some magnetoresistive component in the measurement perhaps due to some anisotropy or inhomogeneity in the material. Since the magnetoresistance is an even function of H while the Hall effect is an odd function of H, I have found it easiest to examine the Hall effect by plotting $V_y(H)$ - $V_y(-H)$ as a function of H. This give the antisymmetric portion of the Hall voltage (subtracting the symmetric magnetoresistive contribution) without assuming a Hall effect which is linear in the applied field H.

3.1.2.2 Geometry

In order to calculate the resistivity from the measured resistance, the geometric ratio relating the two must be known. Most analyses are based on some temperature or field dependence, and therefore it is more important that this geometric factor does not change during the experiment than it is to know the value precisely. The geometrical factor can change if the sample has internal cracks or if the contacts are flowing or cracking.

For resistivity measurements, the resistance of the entire circuit must be taken into account. A tiny metallic sample may have a resistance much smaller than that of the contacts or even the wires leading to the voltmeter. For this reason, four probe measurements are used. A known current is applied through the sample from two of the contacts. The voltage across a

portion of the sample is sensed with two other contacts. The voltmeter has a high input impedance so that very little current is drawn from the voltage contacts. If there is almost no current flowing through the voltmeter circuit, then there is almost no voltage drop across the contacts or contact wires. In this way, the voltage measured is the voltage across the sample. Since the voltage contacts are separated from the current contacts, one must be cautious of the tacit assumption that the current flows uniformly through the entire sample. If the current avoids the voltage contacts, the results will be spurious. For high resistance samples, two probe measurements, where the voltage contacts are the same as the current contacts, can be used. The resistance due to the contacts and grain boundaries can be determined with AC impedance spectroscopy. Extremely high resistance measurements can be done with an electrometer where a constant voltage is applied and the electrometer measures the tiny trickle of current that passes through.

The simplest geometry is the bar sample. The resistivity of a bar is the resistance times the cross-sectional area divided by the length between the voltage contacts. Samples can either be shaped into bars or rods, or films can be patterned. Patterned films can be ideal for transport measurements since the geometric ratio is well known, and the effects of the contacts can be minimized by patterning small contact wires in the film. Unfortunately the patterning process can damage the films.

For isotropic two-dimensional samples, the physical dimensions (other than the thickness) need not be measured. In some cases the geometric ratio can be calculated analytically using conformal mappings. The geometric ratio has been calculated for a sheet where four collinear and equally spaced contacts are in the center of a sheet [51]. The Van der Pauw [52, 53] configuration uses four contacts placed anywhere on the edge. By switching one of the current and voltage leads, the geometric ratio can be calculated. The Van der Pauw configuration can also be used for the Hall effect.

3.1.2.3 Contacts

Bad contacts are often the cause of problems in a transport experiment. Making good contacts is the closest I've come to producing fine art in the laboratory. Contacts need to be strong and durable yet small. The thermal stresses of temperature cycling can weaken or break a contact. A weak contact is worse than a broken one because a weak contact always seems to work at room temperature, give unusual results at some other temperature and then return to normal at room temperature. A good contact is not delicate, it should be able to withstand some mechanical stress at room temperature.

Contacts need to be small when it is assumed that they are point contacts or if the sample is physically small. If the size or shape of the contact affects the geometry of the measurement (section 3.1.2.2) any sintering, melting, cracking, etc. of the contact will affect the measurement. Unfortunately, the smaller the contact, the weaker it usually is.

The contact wires can also cause stress in the contact since they also will expand and contract with temperature. Contact wires should have bends to minimize the strain on the contacts. Contact wires should, if possible, also be plastically deformed so that they will stay at the desired position without any mechanical force, before the contact material is applied.

Indium metal makes good contacts for measurements at temperatures less than 400K. Indium is quite ductile and therefore can withstand considerable strain before breaking. Freshly cut indium can be pressed onto most flat sample surfaces. The contact wire can then be sandwiched between a second piece of indium. In this way, contacts a fraction of a millimeter can be made. For surfaces which are difficult to adhere to, an ultrasonic soldering iron usually helps. Shiny, ultrasonically vibrating, liquid indium will stick to almost anything and can be drawn out into long wires. Any yellow, oxidized surface of the molten indium will hinder the adhesion to a sample.

Silver paint contacts can be made quite small if the suspension has the appropriate viscosity. These contacts can be used to low temperatures but are often unreliable. I have had better results with the two component silver epoxy (epo-tek® 417).

Polyimide based silver epoxy (epo-tek® P1011) can be used well above its recommended maximum temperature of 300°C. It requires only a low temperature curing and works almost up to the melting point of silver. This was used for measurements to 1200K. A platinum paste is available for high temperature contacts that requires a high temperature sintering.

3.1.2.4 Reproducibility

It is obviously important to only report reproducible data. Important data should always be reproduced and claims about general properties of a material should be reproduced on other samples or even types of samples. It is best to simply not collect irreproducible data. If there is anything unusual in the above checks, it is probably not worth the time collecting the data.

Extensive automation of the data collection system may actually help increase the consistency of the measurement. If the temperature is changed in a uniform way, the data tends to be more consistent than if points were taken at random temperatures. This is probably due to temperature gradients in the sample or sample chamber, that depend on the heating or cooling rate. Measurements as a function of temperature should generally be measured while heating and cooling in case there is some temperature differential between the sample and the thermometer. Some contacts break easily when rapidly cooled, requiring the slow cooling of an automated system. With enough automation so that the experiment can be left unattended for several hours or days, extra data can be collected. This allows more frequent checks for linearity and reproducibility.

3.1.2.5 Apparatus

Transport measurements for this work were made in DC allowing a few seconds for the current and voltages to stabilize. A constant current source (Keithley model 220 or 224) was used to supply the current and a separate voltmeter (Keithley model 181, 182, 196 or 197) used to measure the voltages. Current is not usually measured independently but can be with the addition of an electrometer into the circuit. A computer controlled the current source, read the voltages and temperatures and recorded the data. Typically, 5 pairs of $R(I) = (V(I) - V(-I))/2$ were measured at slightly different currents (e.g. 20% variation) to estimate the precision. For resistances greater than $10^6\Omega$ (often $T < 100$K) two point resistance measurements were made using an electrometer.

Most of the low temperature and all the magnetoresistance and Hall effect measurements were made in the cryostat of the Quantum Design $MPMS_2$ SQUID magnetometer described in section 3.2.1.1. The computer that controls the SQUID magnetometer can also operate subroutines that can control GPIB compatible devices. These EDC (External Device Control) subroutines can be quite general, but have a limited number of available commands. It is necessary to further process the data recorded from the EDC subroutine in order to use it in a graphing or spreadsheet program. The standard SQUID magnetometer software controls the temperature and magnetic field. The thermometer is not very near the sample, so reliable data must be taken after the temperature has stabilized. This usually takes about 5 minutes for routine measurements or 30 minutes if any temperature drift is to be avoided. Since the measurement can run for several days unattended, time is usually not much of a problem.

A 10 wire transport probe prefabricated at Quantum Design was used for the measurements. A special tip was made out of 8 bore alumina rod to provide a surface perpendicular to the magnetic field. Films can then be

attached to this surface with double-sided sticky tape to measure the Hall effect and transverse magnetoresistance. A simple copper plate attached to the tip of the transport probe provides a surface parallel to the magnetic field for longitudinal and transverse magnetoresistance measurements. One limitation of the SQUID magnetometer is its relatively small sample chamber (8mm diameter).

High temperature (300K < T < 1200K) measurements were performed in a furnace (in air) with a slowly varying temperature (≈ 1 K/min.). The temperature was recorded using a Type-K thermocouple positioned a few millimeters from the sample. The sample holder was made from an 8 bore alumina rod. The 2 thermocouple wires and 4 platinum wires which contact the sample were fed through the bores of the alumina rod. The wires are positioned to facilitate changing the sample and attaching new contacts. The furnace was programmed to heat and cool using a standard Eurotherm (model 818) power regulator and temperature controller. Data were continuously recorded by a computer using LabView software as the furnace heated and cooled. Lower temperature measurements can be similarly made by dipping the probe into a dewar of liquid nitrogen or liquid helium.

3.1.3 Analysis

Careful transport measurements can help identify transport mechanisms. Knowledge of transport mechanisms not only helps us to understand the microscopic nature of the material but also allows us to predict other properties using previous theoretical or empirical knowledge of other materials with the same transport mechanism. For example a few percent impurity due to processing may not affect the room temperature resistivity of a metal while greatly decreasing that of a band semiconductor.

Some of the common transport mechanisms and their predicted transport properties are given below. Since there is not much overlap of mechanisms or properties between metals and insulators, it is convenient to categorize

materials as metals or insulators-semiconductors. Using the room temperature resistivity for this definition is attractive since metals are supposed to have low resistivity while insulators have high resistivity, but imprecise since a dirty semiconductor may have a lower resistivity than a poor metal at some high temperature. Even though theoretically metals have zero or low resistivity as the temperature approaches zero while insulators have infinite resistivity at $T = 0$, such a definition is impractical for materials which undergo a metal-insulator transition. Here, a metal is defined to be a material with a metallic slope in the resistance *vs.* temperature curve: $d\rho/dT > 0$ while a insulator/semiconductor has $d\rho/dT < 0$ This definition is consistent with most microscopic models of metals and insulators.

3.1.3.1 Metals

The resistivity of a metal is best described in terms of elastic and inelastic scattering mechanisms. Without scattering the itinerant electron wavefunctions would allow electron transport without loss or transfer of energy. In the relaxation time approximation, Matthiessen's rule applies, which states that the total resistivity is the sum of each of the individual resistivity contributions. The different scattering mechanisms usually depend on temperature with a particular power law. Thus the total resistivity is often a polynomial in T.

3.1.3.1.1 Impurity scattering

Impurities and defects disrupt the disrupt the Bloch wavefunctions and scatter electrons. Since this perturbation of the crystal lattice is unaffected by temperature, the resistivity is temperature independent. The impurities can be in the form of elemental substitutions on an atomic site, interstitial atoms or vacancies - anything that disrupts the periodic electronic structure. Since a

grain boundary is a plane of defects, grain boundary resistance is similarly temperature independent and often quite large.

3.1.3.1.2 Electron-electron scattering

The strong Coulomb interaction between electrons provides a mechanism for electron-electron scattering. The exclusion principle limits the scattering to electrons in partially occupied levels near the Fermi surface. For two electrons to scatter, both must be in this shell of partially occupied levels with width $k_B T$ about the Fermi level. This leads to a scattering rate and therefore resistivity proportional to $(k_B T)^2$.

3.1.3.1.3 Electron-phonon scattering

Other than impurities, lattice vibrations or phonons can disrupt the periodic structure of the lattice. This will scatter the electrons and lead to an intrinsic source of resistivity present even in a sample free of crystal imperfections. The most widely employed expression for this resistivity is the Bloch-Grüneisen formula [54]: $\rho = \frac{KT^5}{\Theta_D^6} \int_0^{\Theta_D/T} \frac{z^5 dz}{(e^z - 1)(1 - e^{-z})}$ where K is a constant characteristic of the metal, and Θ_D is the Debye temperature (see section 3.3.2.2).

At high temperatures $T/\Theta_D > 0.5$, this gives a resistivity proportional to T: $\rho \approx KT/4\Theta_D^2$. At low temperatures $T/\Theta_D < 0.1$ the resistivity follows the Bloch T^5 law: $\rho \approx 124.4\, KT^5/\Theta_D^6$.

3.1.3.2 insulators/semiconductors

A material is insulating or semiconducting when $d\rho/dT < 0$. The mechanisms described below predict this behavior because the conduction must be thermally activated. The conducting species must overcome some energy barrier for conduction. Thermal energy supplies the energy to

overcome the barrier and therefore an increase in temperature increases the conductivity.

3.1.3.2.1 Band insulators/semiconductors

The electron transport in a semiconductor with an energy gap E_g between the conduction and valence bands is limited by the number of excited carriers. In the intrinsic regime (low doping concentrations and high temperatures), the chemical potential lies in the middle of the gap so that the thermal energy required to excite a carrier is $E_g/2$. The carrier concentration n thus increases exponentially with temperature $n \approx \exp(E_g/2k_BT)$. The drift mobility $\mu = v/E$ defined by the drift velocity v in an electric field E in a semiconductor can be complicated and depends on the doping [55]. At low temperatures, impurity scattering is expected to dominate giving $\mu \propto T^{3/2}$. Above about 100K lattice scattering will dominate with an approximate temperature dependence $\mu \propto T^{-3/2}$. Thus the conductivity of an intrinsic semiconductor is $\sigma = ne\mu \approx T^{\nu}\exp(E_g/2k_BT)$. For elemental semiconductors, the experimentally observed mobilities have an exponent $\nu = -1.5$ or larger (more negative) [55]. The Hall effect is more complicated to determine *a priori* for an intrinsic semiconductor since the concentration of electron and hole carriers are the same.

In the extrinsic regime (doped semiconductors at lower temperatures) the carrier concentration is determined by the thermal excitation of carriers from donor or acceptor impurities. The carrier concentration retains the form $n \approx \exp(\Delta E/k_BT)$ where ΔE is determined by the difference in energy between the donor and band energies and the temperature regime of interest [56]. For example, ΔE is one half the band gap ($E_g/2$) for an intrinsic semiconductor or $\Delta E = E_g - E_d \approx E_g$ for an extrinsic semiconductor with donor (or acceptor) energy levels E_d from the band edge. Since usually one type of carrier (hole or electron) is dominant, the Hall effect $R_H = 1/nec$ is quite large since n is small,

varies exponentially with temperature and can be used to determine the sign of the carrier and the carrier concentration.

3.1.3.2.2 Polarons

A localized electron will always distort its surroundings relative to an unoccupied site simply because of the coulombic interaction of the electron and the surrounding atoms. The potential well produced by this distortion acts as a trapping center for the *self-trapped* carrier. The quasiparticle composed of a self-trapped electronic carrier taken together with the pattern of atomic displacements that produces the self-trapping became known as a *polaron* because self-trapping was first considered in ionic (polar) materials. The quasiparticle can move as a whole, the electron and the distortion moving together.

The spatial extent of the self trapped states depends on the range of the interaction. Long-range electron-lattice interactions [57] produces *large polarons* with a finite radius. In such an instance, the self-trapped electronic carrier extends over multiple sites. The radius of the large polarons decreases continuously as the strength of the electron-lattice interaction is increased. The multi-site extension of the large polaron results in its itinerant motion.

In contrast, *small polarons* are confined to a single lattice position due to strong short-range electron-lattice interaction. If the electron-lattice interaction is too weak, the carriers remain unbound. The extreme confinement of the small polaron typically leads to its moving by thermally assisted hopping.

One of these two different types of polarons will be stable when both long-range and short-range electron-lattice interactions coexists. The presence of long-range interactions eases the requirements for forming a small-polaron, but only once the interactions are sufficiently strong will the polaron change from large to small.

The dichotomy between the two types of polarons seems unnecessary when considering their spatial extent, but the conductivity of the two types of polarons are vastly different. Large polarons move with significant mobilities $\mu > 1$ cm^2/V sec, that decrease with increasing temperature (metal-like). In contrast, small polarons move with very low mobilities, $\mu << 1$ cm^2/V sec, that increase with increasing temperature (semiconductor-like).

Polaron formation is frequently studied within the adiabatic limit [58-60] in which the electron carrier adjusts instantaneously to the positions of the atoms. When the phonon forms an excited state where an occupied and a neighboring unoccupied site are equivalent, the adiabatic polaron can move freely move back and forth between the two sites before the system relaxes. At temperatures below $\Theta_D/2$, where Θ_D is the Debye temperature, it is predicted that the polaron behaves like a free particle with greatly increased effective mass. In the high temperature regime ($T > \Theta_D/2$) the electrical conductivity is predicted [58] to be $\sigma = 3ne^2\omega a^2/2k_B\ T^{-1}\exp(-E_A/k_BT)$. Here n is the number density of charge carriers, a is the site-to-site hopping distance, ω is the longitudinal optical phonon frequency and e is the electronic charge. The Hall mobility may behave like the drift mobility with 1/3 of the activation energy, but in the adiabatic approximation the form is much more complicated [58].

In the theory of small polaron hopping, it was found that the motion of the polaron is only weakly dependent on the magnetic order, and changes little as the temperature is raised above the Curie temperature [61, 62].

Small polarons were first studied in the non-adiabatic regime, where the electron transfer integral and hence the bandwidth is small [60, 63-65]. In the high temperature limit this gives a factor of $T^{3/2}$ instead of a T in the drift and Hall mobilities. There are some unphysical assumptions required for the non-adiabatic analysis to be valid. The assumptions behind the adiabatic

polaron formation are more physically plausible and therefore the adiabatic analysis is preferred.

3.1.3.2.3 Diffusive Conductivity

The same form of the conductivity derived for adiabatic small polaron hopping is found more generally for diffusion limited conduction. If the charge carrier must overcome an activation energy, E_A, to hop to a neighboring site, the probability for hopping will be proportional to $\exp(-E_A/k_BT)$. From the theory of the random walk, the diffusion constant D can be estimated using this hopping probability, the frequency, ω, with which an attempt to hop is made (usually the frequency of the optical phonon which provides the lowest barrier to hopping at some instant), and the site to site distance, a: $D = \lambda\omega a^2\exp(-E_A/k_BT)$. λ is a geometrical factor approximately equal to 1. The mobility is related to the diffusivity via the Nernst-Einstein relation $\mu = eD/k_BT$. Thus the conductivity, $\sigma = ne\mu$, of a general, activated, diffusive process is $\sigma = ne^2\omega a^2/k_B\ T^{-1}\exp(-E_A/k_BT)$. The transport of ions in a crystal is diffusive, and therefore the ionic conductivity is often analyzed assuming this form of the conductivity [66]. The transport of small polarons is very similar and has also been described in this way [67-69].

3.1.3.2.4 Variable range Hopping

For a semiconductor or insulator at low enough temperatures, the predominant conduction mechanism may no longer be by excitation of carriers to the mobility edge or by thermally activated hopping to the nearest neighbor but by variable range hopping. At low temperatures, the mechanism with the lowest barrier energy will dominate. Due to any randomness in the sample, the hopping site with the lowest barrier energy will not in general be the nearest neighbor. The increased hopping distance will of course reduce the probability that the carrier will tunnel to this

position; however, this is always offset by the lower barrier energy at sufficiently low temperatures.

The simplest quantitative derivation of the form of variable range hopping is the following. For a given site, the number of states within a range R per unit energy is $(4\pi/3)R^3N(E_F)$, where $N(E_F)$ is the density of localized states. Thus the smallest energy difference for a site within a radius R is on average the reciprocal of this $\Delta E = 1/[(4\pi/3)R^3N(E_F)]$. Thus, the further the carrier hops, the lower the activation energy.

The carrier has an electronic wave function exponentially localized on a particular site with a decay or localization length of ξ. The tunneling probability that the electron will hop to a site a distance R away will contain a factor $\exp(-2R/\xi)$. The further the distance, the lower the tunneling probability.

Since the hopping favors large R while the tunneling favors small R, there will be an optimum hopping distance R for which the hopping probability proportional to $\exp(-2R/\xi)\exp(\Delta E/k_BT)$ is a maximum. This will occur when $1/R^4 = 8\pi N(E_F)k_BT/\xi$. Substituting this value for R, the hopping probability and thus the conductivity is proportional to $\exp(-(T_0/T)^{1/4})$ where $T_0 = C\xi^3/k_BN(E_F)$. C is a constant which in this derivation is $24/\pi \approx 7.6$, but other values of C are obtained from more sophisticated analyses. $C \approx 21$ is recommended by Shklovskii and Efros.

The conductivity for variable range hopping is usually given the form $\sigma_0 \exp(-(T_0/T)^\nu)$, $\nu = 1/4$. The exact form of σ_0 depends on the model and may have a power law temperature dependence of its own. For example $T^{0.33}$ has been found [70].

Other values of ν can be obtained theoretically using different assumptions. The above derivation assumes a three dimensional system. In

general, $\nu = 1/d+1$ where d is the dimension of the system. In particular this gives $\nu = 1/2$ and $\nu = 1/3$ for one and two dimensional systems respectively. The exponent $\nu = 1/2$ is also found when the Coulomb interaction between the electrons is taken into account [71]. This interaction produces a gap in the density of states. If this gap is larger than the bandwidth of the hopping carriers, $\nu = 1/2$ is found. If polarons are the charge carriers, the range of validity for $\nu = 1/d+1$ may be reduced to lower temperatures than normally expected [72].

3.1.3.3 Poor Metals / Heavily doped semiconductors

Some materials which would normally be considered metals, have $d\rho/dT < 0$ over a significant temperature range. Amorphous metals and metallic glasses, which can be prepared by rapid cooling, film deposition, or irradiation, for example, can show a resistivity which decreases slightly with temperature. Most examples are transition metal alloys with zero temperature resistivities approaching the Ioffe-Regel limit, where the mean free path is equal to the interatomic distance, corresponding to about 1 mΩcm [69]. Heavily doped semiconductors can show similar behavior described below.

The physics behind this phenomenon is not completely understood, and the data is usually interpreted on a case by case basis. The theoretical conductivity is generally described as a power series with respect to temperature where the power ranges from zero to one, e.g. $\sigma = \sigma_0 + mT^n$, $n < 1$, and m can be positive or negative. $n = 1/2$ or 1 is often observed and can be explained theoretically. For example, Altshuler and Aronov predict an $n = 1/2$ correction for the effect of long-range interaction between electrons [70]. For semiconductors doped near the metal-insulator transition, $n = 1/3$ has been observed and explained theoretically [70].

Complex materials often have resistivities that are inadequately described by the simple models given above. For example the cuprate superconductors and $SrRuO_3$ show a linear resistivity well above the Ioffe Regel limit [73]. A more extreme example is $Ba_6Co_{25}S_{27}$ which not only has a resistivity minimum but a less than linear resistivity above the minimum [42]. As more materials with complex electronic structures are examined, such non-standard behavior will certainly become more common.

3.1.3.4 Phase transitions

Any precise measurement as a function of temperature can usually detect or be influenced by a phase transition. Conductivity data in particular can be quite precise but can also be greatly influenced by subtle electronic, magnetic or structural changes. Thus one should be cautious when fitting data to very similar functional forms. Electronic transitions such as metal-insulator transitions and charge ordering (charge density wave formation) obviously change the conductivity at the ordering temperature. Magnetic transitions are also easily observed in the conductivity since local moments act as scattering centers, or may even help localize/delocalize carriers. Ferromagnetic metals for instance always show a decrease in resistivity as the temperature goes below the Curie temperature [73]. Structural phase transitions usually change the symmetry and volume, which affects the conduction paths and density of the charge carriers. This will subtlety change the conductivity at the transition temperature even if the conduction mechanism remains the same, as shown in section 4.2.5.

Careful measurements can help determine the nature of such phase transitions. If the phase transition is reversible and not hysteretic, i.e. the data are the same upon warming and cooling, then the phase transition is probably a single second order process. If the data is hysteretic then a first order process is involved. For example, the ferromagnetic and accompanying metal insulator transition in the manganites appears to be of second order.

The charge ordering transition in the nonmagnetic manganites is also not hysteretic and probably second order. However, in samples where both ferromagnetism and charge ordering occur, the conductivity and magnetic susceptibility are hysteretic, indicating a more complex transition. In this case, there is no subgroup-supergroup relationship between the two ordered phases; so to go from the magnetically ordered phase to the charge ordered phase requires a first order (hysteretic) phase transition [74, 75].

In the region near a second order phase transition (critical regime) physical quantities such as electronic transport are often best described by a power law about the critical point, *e.g.* $(T - T_C)^n$ where T_C is the critical temperature and n is the critical exponent. For example, the resistivity of a ferromagnet near the Curie temperature should be described by a critical exponent (α) equal to that of the heat capacity [73]. Magnetic critical exponents are described in more detail in section 3.2.2.2.4

3.2 Magnetism

The magnetism of a material is usually dominated by the electrons near the Fermi level. Unpaired, localized electrons in insulators have very different magnetism than paired or itinerant ones. Thus, magnetic measurements can detect the subtle electronic structure of a material. Since these measurement do not require contacts, they can be quite easy to perform – and have made them quite standard in characterizing new materials.

3.2.1 Measurement

There are various ways to measure a magnetic field and thus magnetization. The most common instruments to measure D.C. magnetization are the vibrating sample magnetometer, Faraday balance and SQUID magnetometer. Surface magnetization can be accurately measured by the Magneto-optical Kerr effect (MOKE). The apparatus used in this study is a Quantum Design MPMSR$_2$ SQUID magnetometer.

3.2.1.1 Apparatus

The Quantum Design SQUID (Superconducting Quantum Interference Device) MPMS (Magnetic Property Measurement System) is a commercially available "turn-key" magnetometer. The device runs on liquid He and can reach temperatures of 2 K to 400 K and fields up to 7 Tesla. A sample heater is available to achieve temperatures 300 K to 800 K but the sample space diameter is reduced from 8 mm to about 3 mm. The revision 2 ($MPMSR_2$) improves the software, allowing simple programming for measurements lasting several days without requiring maintenance.

The SQUID coils detect the longitudinal component of the magnetization as the sample is pulled through them. The coils are wound in a second-derivative configuration in which the upper and lower single turns are counter wound with respect to the two-turn center coil. This configuration strongly rejects interference from nearby magnetic sources and allows the system to function without benefit of a superconducting shield around the SQUID sensing loops. The raw data are a set of voltage readings taken as a function of position as the sample is moved upward throughout the sensing loops. The data are normally fit to a theoretical signal to calculate the magnetic moment. Several vertical scans are averaged to obtain a standard deviation.

The two important data reduction algorithms are compared in Figure 3-1 for a standard Yttrium Iron Garnet (YIG) sample. The "linear regression" assumes the sample is properly centered. If the sample is not exactly centered (longitudinally), the measured moment will be noticeable different. The "iterative regression" iterativly finds the center, so if the sample is off-center the reported moment does not change. When doing temperature scans, the length of the sample rod will significantly change. The iterative regression is clearly superior for these measurements. The precision of these two algorithms are the same (Figure 3-1). The "full scan" algorithm is simply the

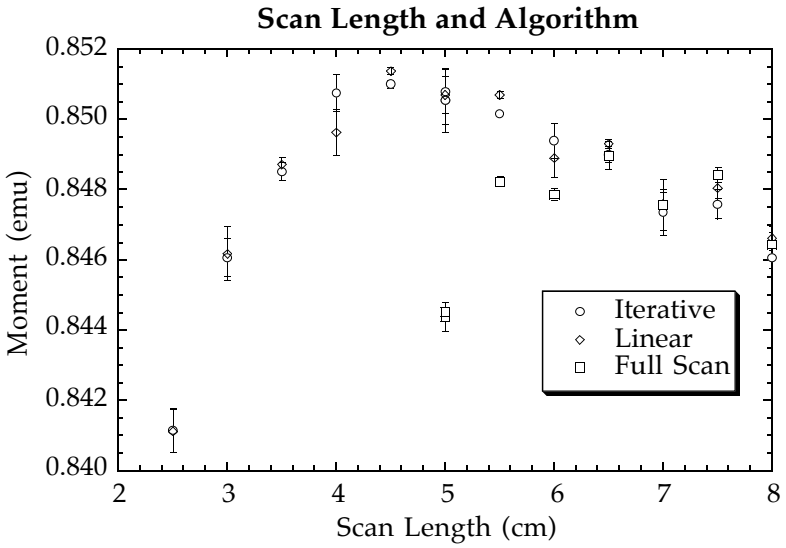

Figure 3-1 Effect of changing the scan length for magnetization measurements. A YIG crystal is used. The three data reduction schemes are also compared. The results for the full scan algorithm with scan length less than 5 cm are off scale.

sum of the squares of the raw data and does not fit the data to any particular curve.

The distance the sample is pulled through the coils, called the scan length, can be varied. The effect of the scan length is shown in Figure 3-1. Long scan lengths are not ideal since field and temperature gradients exist in the sample chamber. Very long (> 6 cm) will even destabilize the chamber temperature, requiring several minutes to stabilize before each scan. Field gradients will cause irreversible flux motion in superconductors - changing the magnetic moment. Short scans can drastically reduce the accuracy of the moment without affecting the precision (Figure 3-1). Ferromagnetic and paramagnetic substances are not very irreversibly affected by field gradients, so a medium scan length of about 5 cm is used to ensure good accuracy.

The second-derivative configuration of the SQUID coils will, in principle, not pick up the magnetization of the sample holder if it has a uniform magnetization. For this reason, a plastic straw with the sample wedged in the center makes an ideal sample holder. Shrink wrap tubing, shrunk around the sample also makes a good, but less rigid, sample holder. If string or grease is used to hold the sample, then there will be an additional contribution to the magnetization due to the sample holder. Similarly, if the sample is between two quartz rods, there will be a paramagnetic contribution to the magnetization due to the gap between the diamagnetic quartz. Materials not containing transition elements have a diamagnetic susceptibility of about -0.5×10^{-7} emu/g, so light sample holders (plastic) are somewhat preferable to heavier ones (quartz glass).

The measured moment is also somewhat affected by the horizontal centering of the sample. Rotating the sample along the field axis should have no effect on the moment. However, it may very slightly change the horizontal position of the sample. For whatever reason, the moment can change a few percent with the sample rotator. Such a sensitivity on orientation probably results in some of the unexpected jumps in the data.

The YIG sample has a moment 96.6% of that expected. Before an experiment the sample is rotated to give the maximum moment. This is to minimize the possible underestimation of the moment and usually provides a region where the moment is less sensitive to small changes of the rotation.

The transverse SQUID coils can in principle also measure the net transverse magnetic moment. A longitudinal component to the magnetization will affect the transverse measurement. The sample can be rotated along the axis of the sample rod, which in combination with the transverse measurements can be used to measure the transverse-only moment.

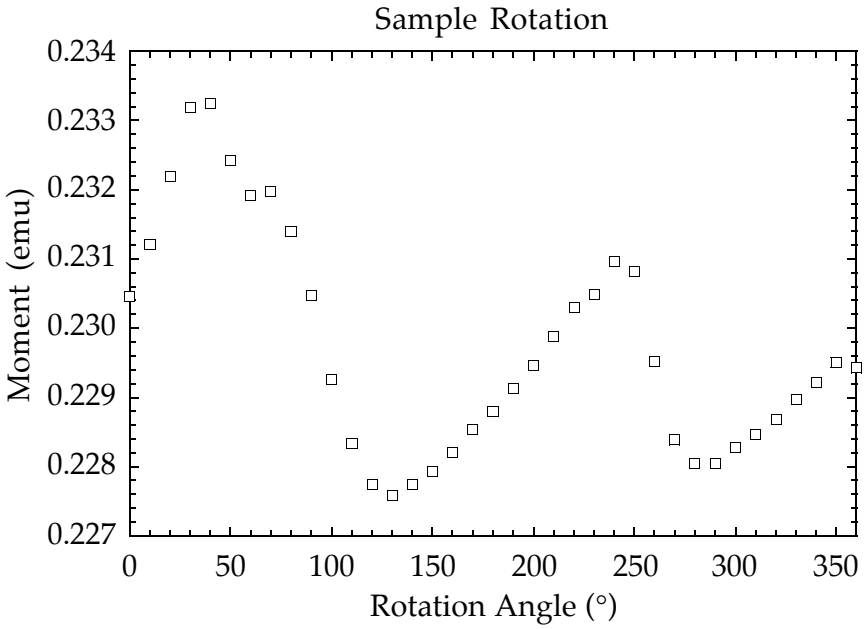

Figure 3-2 Magnetization of YIG sample as it is rotated along the field axis.

3.2.2 Analysis

The important quantities in magnetic measurements are the magnetic field vector **H**, measured in Oersted and the magnetization intensity (or simply the magnetization) **M**, measured in emu/volume (electromagnetic unit = erg/Oersted). **M** is often reported in units of emu/g, emu/mole or Bohr magnetons (μ_B) per magnetic atom. The magnetic induction field **B** measured in gauss, defined by $\mathbf{B} = \mathbf{H} + 4\pi\ \mathbf{M}$, is often considered more fundamental in physics. The above units are CGS units which are more prevalent than MKS since the equations tend to be simpler. The MKS unit which is used commonly in the magnetic literature is the Tesla = 10000 gauss.

Most materials have a magnetization proportional to the applied field. The magnetic susceptibility χ, defined by $\mathbf{M} = \chi\mathbf{H}$, relates these two quantities. It is convenient to use $\chi = \mathbf{M}/\mathbf{H}$, for non-ferromagnetic and isotropic

substances. Otherwise, $\mathbf{M} = \mathbf{M}_0 + \chi\mathbf{H} + \chi_3\mathbf{H}^3 + \ldots$ can be used where χ is now a second rank tensor describing the linear response, $\mathbf{M}_0$ is the spontaneous magnetization, and χ_n describe the higher order nonlinear terms.

The magnetic field **H** can be produced either by electric currents or by the magnetization. If a sample is magnetized, an **H** field is produced in the sample to oppose the magnetization and therefore *demagnetize* the sample. This demagnetization field $\mathbf{H}_d$ is for an ellipsoidal sample directly proportional to the magnetization $\mathbf{H}_d = N_d\mathbf{M}$, where $0 \leq N_d \leq 4\pi$ is the demagnetization factor. Since the demagnetization field depends on the shape of the sample, it is the internal field $\mathbf{H}_i = \mathbf{H}_a - \mathbf{H}_d$ the applied field minus the demagnetization field which affects the magnetic response. Since the correction for the demagnetization fields is often ignored, one should be wary of the effects of demagnetization. Ferromagnets in small applied fields for example may have reduced bulk magnetization due to demagnetization.

3.2.2.1 Diamagnetism and Paramagnetism

Since atoms are made up of charged particles which undergo orbital motion and have magnetic moments, there are many ways a materials can have a magnetic response. A diamagnetic response is that for which the susceptibility is negative while a positive contribution to the susceptibility is paramagnetic.

3.2.2.1.1 Larmor diamagnetism

Since the electrons in an atom are essentially free charges orbiting a nucleus, the application of a magnetic field, by Lenz's law, induces an opposing magnetic moment. The resulting magnetic susceptibility is therefore negative and known as Larmor or core-electron diamagnetism. Both the classical and quantum mechanical analyses yield the same result, namely that the diamagnetic susceptibility of an atom or ion is proportional to the number of electrons it contains, Z and its cross sectional area

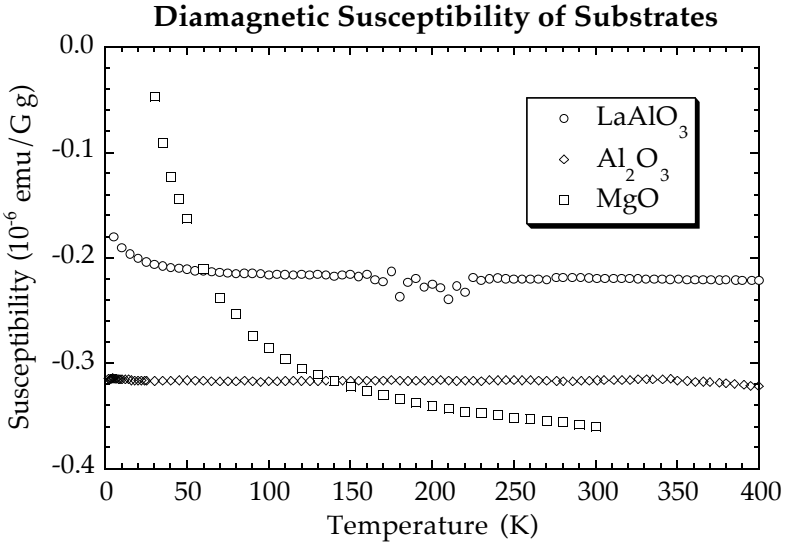

Figure 3-3 Diamagnetic magnetic susceptibility of typical substrates. The increase in the susceptibility at low temperatures is due to paramagnetic impurities.

$\chi_{mol} = -\langle r^2 \rangle ZN_A e^2/6mc^2$ where $\langle r^2 \rangle$ is the mean square electron radius. Since atomic sizes are roughly the same, and masses nearly proportional to Z, the diamagnetic susceptibility per gram for all substances are about the same $\chi_g \approx -0.5 \times 10^{-6}$ emu/g G. Since it is difficult to calculate $\langle r^2 \rangle$ accurately, it is best to use experimental values (tabulated in [76, 77]). In most measurements of paramagnetic and ferromagnetic substances, the diamagnetism is so small it is usually ignored.

An example of where core diamagnetism is important is shown in Figure 3-3. Oxide substrates are generally diamagnetic, but provide a significant susceptibility due to their large mass compared to the mass of a thin film. The diamagnetism is fairly temperature independent but substrates may contain paramagnetic impurities which alter the low temperature diamagnetism.

3.2.2.1.2 Conduction electron diamagnetism

The motion of conduction electrons in a metal or semiconductor will also provide a diamagnetic response (Landau diamagnetism) to a magnetic field. This is difficult to calculate but generally of the same order as the Pauli paramagnetism (section 3.2.2.1.3). A superconductor, however, expels a magnetic field completely (Meissner effect) by the motion of the superconducting electrons. The diamagnetism of a superconductor is, therefore, very large, $\chi_{vol} = -1/4\pi$ emu/cc G in the Meissner regime. Since superconductivity is affected by temperature and a magnetic field, the magnetic response of a superconductor is actually quite complicated.

3.2.2.1.3 Pauli paramagnetism

Electrons in a metal can be partitioned into spin-up and spin-down bands, parallel and antiparallel to an applied magnetic field H. The magnetic field will lower the energy of the spin-up band compared to the spin-down band (by $2\mu_B H$) and spin-down electrons will flip their spins and pour over into the spin-up band. The number of electrons (per volume) that need to flip their spins is approximately the density of electronic states, $n(E_F)$ times one half of the energy splitting. This produces a net magnetization proportional to the magnetic field and therefore a positive susceptibility, $\chi_{vol} = \mu_B^2 n(E_F)$. A more sophisticated statistical-mechanical derivation produces the same result with small correction proportional to T^2. The Pauli susceptibility of a metal should thus be nearly temperature independent and about the same magnitude as the Larmor diamagnetism. Since the contribution of the Landau diamagnetism is not known, it is usually not possible to get more than an order-of-magnitude estimate of the Pauli susceptibility from magnetization measurements. In principle, however, the Pauli susceptibility should be a measure of the bare density of electronic states at the Fermi level, $n(E_F)$, in the absence of many body effects. The linear electronic specific heat term

(γ, section 3.3.2.1) is also proportinal to $n(E_F)$, as well as the electronic effective mass. The ratio of these two experimental results is known as the Wilson ratio.

3.2.2.1.4 Curie paramagnetism

If a material has unpaired electrons, their magnetic spins will be highly susceptible to a magnetic field. The energy to orient the spins comes from the magnetic energy MH which for an atom with effective magnetic moment p, is $\mu_B pH$. The thermal energy $k_B T$, randomizes the spins to oppose the alignment, so the amount of alignment is roughly proportional to $\mu_B pH/k_B T$. The net magnetization is then $\mu_B p$ times the fraction of moments that are aligned. So, the magnetic susceptibility of free spins should behave like $\mu_B^2 p^2/k_B T$. This is several hundred times larger at room temperature than the core or Pauli diamagnetism/paramagnetism, and significantly temperature dependent.

The full statistical mechanical treatment for quantum mechanical moments with spin S, orbital angular momentum L, and total angular momentum J, gives a magnetization per atom $M = g\mu_B J B_J(g\mu_B JH/k_B T)$. g is the Landé g-factor, which for atoms where $J = S$ is the just the electron g-factor, $g = 2.00$, otherwise $g(J,L,S) = \frac{3}{2} + \frac{1}{2}\left[\frac{S(S+1) - L(L+1)}{J(J+1)}\right]$.

Transition metal ions generally have their orbital angular momentum quenched so $J \approx S$. The Brillouin function, $B_J(x)$, is defined by $B_J(x) = \frac{2J+1}{2J}\coth\frac{x(2J+1)}{2J} - \frac{1}{2J}\coth\frac{x}{2J}$. For small x, $B_J(x) \approx x\frac{J+1}{3J}$, while for very large x, $B_J(x) \approx 1$. The magnetization is then linear with respect to the magnetic field until it approaches its saturation value of $g\mu_B J$. In the linear region, $\mu_B H \ll k_B T$, the susceptibility has the Curie form $\chi_{mol} = \frac{N_A \mu_B^2}{3k_B}\frac{g^2 J(J+1)}{T}$

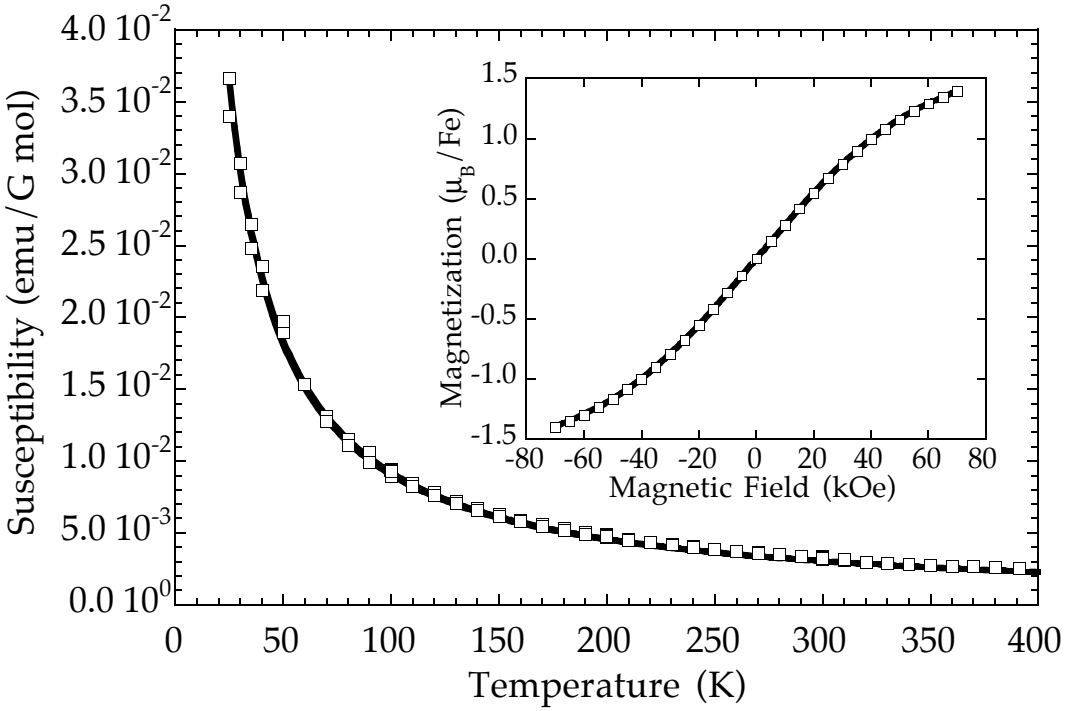

Figure 3-4 Paramagnetic susceptibility and hysteresis loop of a paramagnetic Fe containing organometallic compound [78].

where $\frac{N_A \mu_B^2}{3k_B} \approx \frac{1}{8} \frac{\text{emu K}}{\text{Gauss mol}}$. Since the spin state is not necessarily known, the effective moment p is often reported where $p^2 = g^2 J(J + 1)$. The Curie susceptibility diverges as the temperature approaches zero; however, in real systems the spins will "freeze-out" below some temperature making, for example, an antiferromagnet, ferromagnet, or spin glass.

Insulators with magnetic atoms far apart (do not interact) are good examples of Curie paramagnets. Figure 3-4 shows the magnetic properties of an organometallic compound $[SC(CH_3)_2C(CH_3)NCH_2CH_2NH_2]^-_2$ FeCl with well isolated Fe^{+3} ions [78]. The magnetization is slightly nonlinear at 5 K, as predicted by the Brillouin function. The linear susceptibility can be fit to $\chi = \chi_0 + C/T$ where χ_0 is the diamagnetic correction (section 3.2.2.1.1). If the

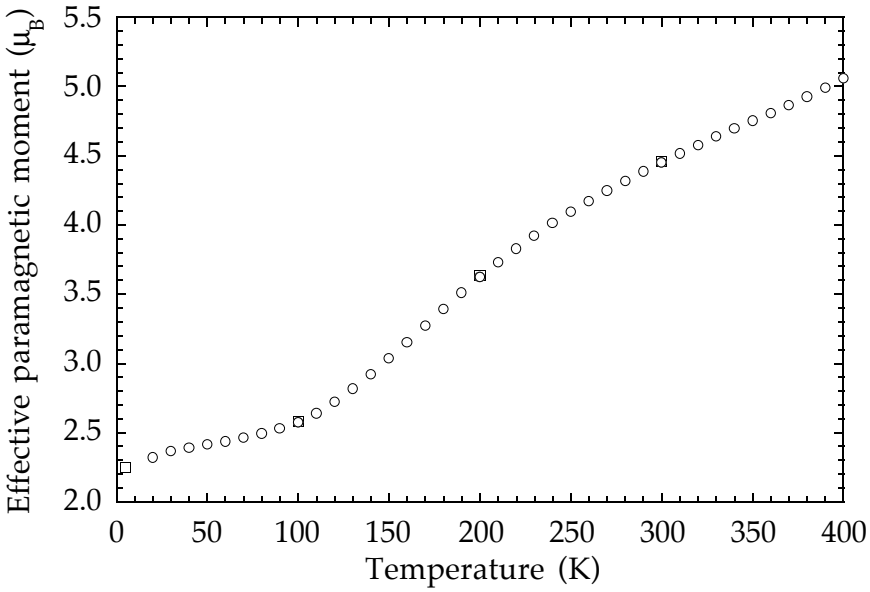

Figure 3-5 Effective paramagnetic moment of Fe in the organometallic compound $[SC(CH_3)_2C(CH_3)NCH_2CH_2CH_2]_2N^-$ $FePF^-_6$ showing a spin transition [78].

diamagnetic correction is assumed to be known, and the effective Curie moment as a function of temperature can be extracted. The compound $[SC(CH_3)_2C(CH_3)NCH_2CH_2CH_2]_2N^-$ Fe PF^-_6 in Figure 3-5 has a gradual spin-transition of the Fe^{+3} from $S = 1/2$ to $S = 5/2$ as the temperature is increased [78].

3.2.2.2 Ferromagnetism

If the magnetic species interact, then their magnetic properties can be profoundly altered. Neighboring moments which prefer to be aligned parallel lead to ferromagnetism while antiparallel alignment gives antiferromagnetism. More complex interactions lead to ferrimagnetism, canted ferromagnetism, and spin glass behavior.

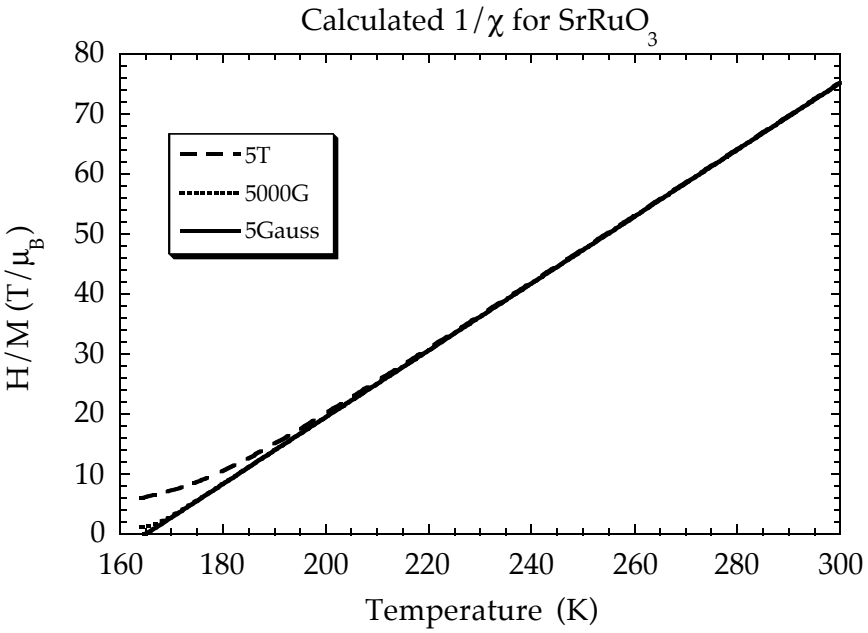

Figure 3-6 Calculated inverse magnetic susceptibility of $SrRuO_3$ using the molecular field model.

3.2.2.2.1 Weiss molecular field model

The phenomena of ferromagnetism, antiferromagnetism and ferrimagnetism can often be well described by a mean field or molecular field model. The molecular field model simply assumes that all the interactions from the neighboring magnetic species can be described in terms of an effective internal or molecular field H_m, which is proportional to the magnetic order $H_m = \lambda M$ (for convenience in this section, M will refer to the magnetization per molecule). For a ferromagnet $\lambda > 0$. The total magnetic field on an atom is then the sum of the applied field H_a and the molecular field. Substituting $H_a + H_m = H + \lambda M$ for H gives a transcendental function of M in terms of H and T which can be solved iteratively. For a simple ferromagnet the only parameter is the molecular field constant λ, which can be determined from the critical temperature T_C via $\lambda = 3k_B T_C / \mu_B^2 p^2$.

Above the Curie temperature the molecular field model gives the Curie-Weiss law for the zero-field susceptibility $\chi_{mol} = \frac{N_A \mu_B^2}{3k_B} \frac{g^2 J(J+1)}{T - \Theta_P}$, where Θ_P is the paramagnetic Curie temperature. In the Curie-Weiss molecular field model $\Theta_P = T_C$. Experimentally, for reasons discussed below, the experimental value of Θ_P is usually a slightly larger than the true critical temperature T_C.

In a field, this susceptibility is slightly less than linear ($\chi_3 < 0$), like it is for paramagnetic moments, due to saturation. The calculated inverse susceptibility, $1/\chi = H/M$, is shown in Figure 3-6 for $SrRuO_3$. The $1/\chi = 0$ intercept of the extrapolation of $1/\chi$ *vs.* T is the paramagnetic Curie temperature Θ_P.

Below T_C the mean field magnetization decreases exponentially slowly as the temperature is raised from $T = 0$ K, as shown in Figure 3-7. The zero field magnetization decreases to zero at the ferromagnetic Curie temperature T_C. Also at low temperatures, the mean field magnetic susceptibility is very small, *i.e.* the application of a magnetic field increases the calculated magnetization only slightly (Figure 3-7).

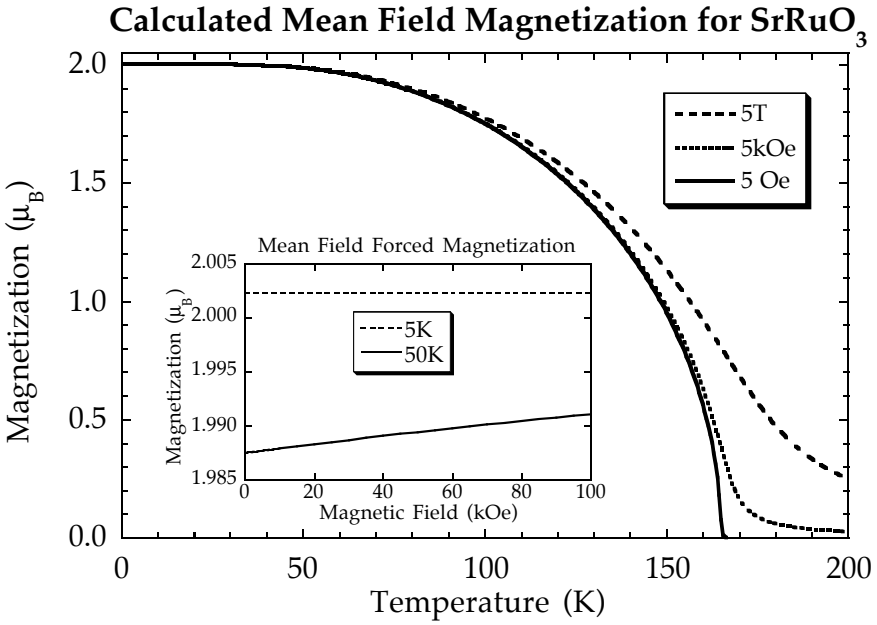

Figure 3-7 Mean field magnetization calculated in various fields for $SrRuO_3$ with T_C = 165K. Inset show the very small field dependence of the magnetization (forced magnetization) in this model.

The molecular field model assumes very little about the microscopic origin of ferromagnetism, only that it makes sense to define a local molecular field. Microscopic models for the interaction of atomic magnetic moments can be formulated into a similar mean field model. In this case, the interatomic exchange energy J can be related to the molecular field constant λ. A microscopic model also leads to a more accurate prediction of the magnetization. At low temperatures, the quantized moments can be collectively excited as discussed in section 3.2.2.2.8 to give the faster decrease in the magnetization than the molecular field model. The microscopic model also gives a more realistic description of the observed properties near the critical point (section 3.2.2.2.4).

3.2.2.2.2 Itinerant electron Model

The ground state properties of a metallic ferromagnet are believed to be fairly well described by the band theory which has advanced in the recent decades [79]. The thermal excitations and finite temperature properties, however, are more difficult because of the effects of strong electron-electron correlations in narrow energy bands. This limits the utility of traditional Hartree-Fock or mean field theory described briefly in this section and requires a treatment of generalized spin density fluctuations described in section 3.2.2.2.3 to describe fully the magnetic excitations in itinerant electron ferromagnets.

The quantum mechanical exchange interaction can lead to ferromagnetism in an electron gas within the band model, commonly known as Stoner ferromagnetism [80, 81] or itinerant electron ferromagnetism. Using the molecular field approximation, a ferromagnetic state is realized for $Jn(E_F) > 1$ where J is the average intra-atomic exchange energy per atom and $n(E_F)$ is the density of states at the Fermi level. This is also known as the Stoner condition for ferromagnetism. For $Jn(E_F) < 1$ the material is not ferromagnetic but has a Pauli susceptibility enhanced by $1/(1-Jn(E_F))$ [82]. This factor is called the Stoner enhancement factor.

The effect of the magnetization at finite temperatures can be calculated using the mean field approximation. Specifically, the energy of the up (down) spin band is uniformly lowered (raised) by an amount proportional to the magnetic polarization ζ and a molecular field constant. Since this model assumes electrons are either in up or down spin bands, the excitations are known as single particle, spin flip, or Stoner excitations. There is no energy gap required for Stoner excitations. However, zero or low energy excitations require a non-zero momentum transfer, while excitations with zero momentum transfer require an excitation energy equal to the exchange splitting as can be seen in Figure 3-8. The region of allowed Stoner excitations

is called the Stoner continuum. Collective, spin-wave excitations are not (yet) included. The mean field analysis [81] gives $(M/M(0,0))^2 = 1-(T/T_C)^2 + 2\chi(0,0)H/M$.

As expected from a Ginzberg-Landau/mean-field approximation section 3.2.2.2.5, this formula predicts mean field exponents of $\beta = 1/2$ and $\gamma = \gamma' = 1$ for T near T_C, and linear M^2 *vs*. H/M Arrott plots. Above T_C the inverse susceptibility is proportional to T^2-T_C^2 [81], which is in gross disagreement with the experimentally observed Curie-Weiss law ($1/\chi = T - T_C$). The finite zero field susceptibility at $T = 0$, $\chi(0,0)$, is essentially the enhanced Pauli-susceptibility [83].

Unlike the local moment model which requires the zero temperature saturation moment $M(0,0)$ to be equal to the sum of all the moments, the band model allows for opposing moments in the minority band at $T = 0$ ($\zeta<1$). This has been used to explain the low saturation moments in metallic ferromagnets, particularly when the saturation moment is lower than the effective Curie-Weiss moment. The Rhodes-Wohlfarth ratio $p_{\text{eff}}/p_{\text{sat}}$ is used to estimate the itinerant electron magnetism character of a material. A plot of $p_{\text{eff}}/p_{\text{sat}}$ *vs*. T_C, known as the Rhodes-Wohlfarth plot, shows that the likelihood of a large $p_{\text{eff}}/p_{\text{sat}}$ decreases as T_C increases [84].

The magnetization in zero field decreases as $M(0,0)\ \sqrt{(1-(T/T_C)^2)}$ which has a slightly stronger temperature dependence than the common approximation $M/M(0,0) = 1 - (T/T_C)^2/2$. This T^2 dependence on the magnetization is often attributed to Stoner, or single particle excitations.

The specific heat at low temperatures is dominated by a linear term, $C_v = \gamma T$. The predicted specific heat discontinuity at T_C is too small to be consistent with the observations [84].

Spin wave excitations can also be included within this simplified band model and predicts the $T^{3/2}$ temperature dependence described previously for

$T/T_C \ll \zeta^2$ (fractional polarization)[81]. A more complete improvement of the Stoner theory takes into account the effect of spin density fluctuations. Such improvements are discussed the following section.

3.2.2.2.3 Generalized Model

The self-consistent-renormalization (SCR) theory [79, 84, 85] combines both single particle and spin wave excitations into generalized interacting spin density fluctuations. It deals with the coupled modes of spatially extended spin density fluctuations in a self-consistent fashion. The theory gives a new mechanism for the Curie-Weiss magnetic susceptibility associated with the spatially extended modes of spin fluctuations instead of the local moments as spatially localized spin fluctuations. Furthermore, the theory is successful quantitatively in explaining various physical properties of weak itinerant ferro- and antiferromagnets: the theory contains a limited number of parameters which can be determined experimentally. Thus by the 1970's the theory of magnetism was advanced to the stage of having two established regimes in the opposite extremes, the local moment systems and weak itinerant ferro- and antiferromagnets. In the former regime the spin fluctuations are localized in real space while in the latter they are localized in *k*-space. In order to unify the two extremes into a single theory an interpolation theory for the intermediate regime was developed in the 1980's using the functional integral method within the static approximation.

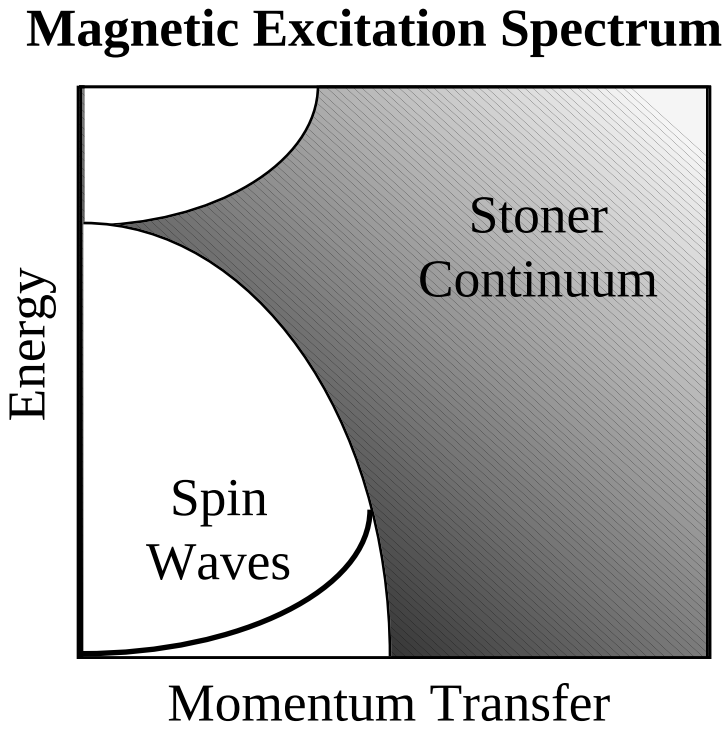

Figure 3-8 Energy spectrum of magnetic excitations. Spin wave excitations have a one-to-one dispersion relation while excitations in the Stoner continuum (shaded region) do not. The intensity of excitations in the Stoner continuum is strongest where the spin waves meet the continuum.

The theory predicts that spin waves exist only in a small region at the origin of (ω,k) space with dispersion relation $\omega = k^2D$, where D is the spin wave stiffness. The strongest intensity of the dynamical susceptibility is in the region where the spin wave excitations meet the Stoner continuum shown in Figure 3-8. In the low temperature limit a $T^{3/2}$ law is predicted in the magnetization. However, calculations for Ni_3Al [86] show that the magnetization is best approximated by a T^2 dependence over a broad temperature range below T_C. It has been assumed that in the highly correlated limit, *i.e.* metallic ferromagnets with a large saturation moment, the magnetization will obey the spin wave $T^{3/2}$ law [85], presumably because of strong evidence for the existence of spin waves in metallic ferromagnets.

The major advancement of the SCR theory is the development of a new mechanism for the Curie-Weiss magnetic susceptibility applicable to itinerant electron ferromagnets. The paramagnetic Curie-Weiss susceptibility arises essentially from the opposition of the magnetic energy to order the spins and the thermal energy to disorder them. The magnetization is then proportional to $\mu_B H/k_B T$, giving the inverse susceptibility H/M linear in T. In the case of the weak itinerant electron ferromagnets there are no localized spins above T_C so the susceptibility cannot arise from this mechanism. Instead, the changing mean-square local amplitude of the spin fluctuation provides the Curie-Weiss susceptibility.

The SCR expression for the inverse magnetic susceptibility contains a contribution from the mean-square local amplitude of the spin fluctuation S_L^2 [84] which can be derived from the fluctuation-dissipation theorem. Calculations have shown that S_L^2 increases almost linearly with temperature above T_C giving rise to the Curie-Weiss law. This is in contrast with the local moment mechanism where S_L^2 is a constant. The Curie constant of the new mechanism is related to the band structure around the Fermi surface and is independent of the saturation moment at $T = 0$. This Curie-Weiss law should hold even for paramagnetic metals when they are very close to the ferromagnetic instability, in contrast to that predicted by paramagnon theories [84].

The temperature variation of $S_L^2(T)$, which determines the new Curie-Weiss mechanism is strongest when the stiffness of the longitudinal spin fluctuations is small. When the longitudinal stiffness is small, a relatively rapid increase in $S_L^2(T)$ with inverse temperature is expected above T_C and it should saturate at a certain value determined by the band structure. After saturation the spin fluctuations behave like local moments with a certain degree of short range order, since the local amplitude of the spin density is almost fixed. This phenomenon is called temperature-induced local

moments [84]. Thus, a subtle change is expected in the Curie-Weiss mechanism at some temperature above T_C. This has been used to explain the change in the Curie constant at around $3T_C$ in $Co(S/Se)_2$ [87]. This phenomenon is also expected in some exchange-enhanced paramagnets.

In Heusler Alloys such as Pd_2MnSn, Ni_2MnSn, Cu_2MnAl, *etc*., manganese atoms are spatially well separated from each other (> 4Å), and are believed to carry well-defined local moments since the Rhodes-Wohlfarth ratio is close to one and neutron scattering experiments can be well analyzed with the Heisenberg model. The ferromagnetic $MnPt_3$, $FePd_3$ and antiferromagnetic $FePt_3$ are likely to have well-defined 3*d* local moments that couple with itinerant 4*d* or 5*d* electrons of Pd or Pt. CoS_2 and the metallic ferromagnets $AMnO_3$ described in chapter 4 fit perhaps best in this category.

In the intermediate regime between the local moment ferromagnets and the weak itinerant-electron ferromagnets are the Ferromagnetic transition metals (Fe, Co, and Ni) and compounds Fe_3Pt and $CeFe_2$. These materials have relatively high T_C's but have Rhodes-Wohlfarth ratios [84, 88] greater than one. The ferromagnetic oxide $SrRuO_3$ also fits in this category as described in detail in Appendix A.

MnSi is a good example of a weak-ferromagnetic helimagnet which is well described by the SCR theory. Other weak ferromagnets such as Ni_3Al, $ZrZn_2$ and Sc_3In can also be described in terms of the SCR theory [84].

Metallic Cr which orders antiferromagnetically below 312K with a long period spin density wave, is the most often used example of an itinerant electron antiferromagnet. However, the Curie-Weiss law is not obeyed above T_N. The magnetism of Cr is best described with an itinerant electron approach with the addition of a nesting Fermi surface model to describe the spin density waves [84]. The antiferromagnetic metals γ-Mn, γ-(FeMn) and γ-Fe have also been studied [84].

Examples of nearly ferro- or antiferromagnetic metals which show a large susceptibility are $CoSe_2$ (Curie Weiss) Pd or YCo_2 [84], and V_2O_3 [89]. The nearly ferro- or antiferromagnetic semiconductor FeSi (Curie Weiss) shows a Curie-Weiss susceptibility above 700K with a broad transition at 500K to a low susceptibility state [84].

3.2.2.2.4 Critical region

As the temperature approaches the critical temperature T_C, the spontaneous magnetization vanishes and the susceptibility diverges. This makes these properteis not analytic near T_C. The observed properties are well described by a power law $|T - T_C|^n$ where n is a scaling exponent. For example, the spontaneous magnetization varies as $(T_C - T)^\beta$ for $T < T_C$, while the susceptibility varies as $(T_C - T)^\gamma$ for $T > T_C$, and for $T = T_C$ (critical isotherm) $M^\delta = H$. The scaling exponents in the critical region are called critical exponents.

The critical exponents are very similar for a wide range of second order phase transitions. They tend to depend only on the general form of the interaction causing the phase transition, such as the dimensionality, and not on the particular material. Thus most ferromagnets fall into the universality class of 3-dimentional Heisenberg or Ising ferromagnets. The theoretical critical exponents calculated for these models is given in Table 3-1. There are only two unique critical exponents in each universality class. The others are related *via* the scaling relations such as $\gamma = \beta(\delta - 1)$.

According to the scaling hypothesis [90], the magnetic equation of state in the critical region depends only on the scaled variables $H/|T_C/T - 1|^{\beta+\gamma}$ and $M/|T_C/T - 1|^\beta$. For example, a plot of the scaled M^2 *vs.* the scaled H/M, (scaled

Arrott plot), will then have only two curves: one branch for the $T < T_C$ data and another for $T > T_C$.

The magnetization near T_C is predicted in the SCR theory, described in section 3.2.2.2.3, to behave as $M = (T_C^{4/3}-T^{4/3})^{1/2}$ [84, 91] which reducecs to $\beta = 1$ for T near T_C.

Table 3-1 Theoretical 3-dimentional critical exponents for different models and selected experimental values [92, 93].

	β	γ	δ
Ising	.33	1.24	4.8
Heisenberg	.36	1.39	4.8
Mean Field	.5	1	3
$ZrZn_2$	.50(3)	1.02(5)	3.1(3)
Fe, Ni, YIG	.37(2)	1.2(2)	4(1)

3.2.2.2.5 Landau mean field theory

Near the critical temperature T_C the molecular field, or mean field model (section 3.2.2.2.5) predicts mean field critical exponents (Table 3-1). The Landau theory of continuous, second order phase transitions (excluding fluctuations) arrives at the same mean field result. Here the free energy is expanded in a Taylor series of the order parameter (M in the case of ferromagnetism). Due to the symmetry of the order parameter, only even powers of M are nonzero. The first few terms are [94]: $G = G_0 + a(T - T_C)M^2 + bM^4 - HM$. At a given H and T, M can be found by minimizing the free energy G. The general solution is $H/M = 2a(T - T_C) + 4bM^2$. Below T_C the saturation magnetization ($H = 0$) is found to be $M^2 = (T_C - T)a/2b$, giving the critical exponent $\beta = 1/2$. Above T_C in a field, M is small so the bM^4 term can be ignored. This gives a susceptibility $\chi = M/H = (T - T_C)^{-1}/2a$, and a critical

exponent $\gamma = 1$. Along the critical isotherm $T = T_C$, $H = 4bM^3$ so the critical exponent $\delta = 3$.

3.2.2.2.6 Arrott Plot

According to the Landau equation of state $H/M = 2a(T - T_C) + 4bM^2$, a plot of M^2 *vs.* H/M at a constant temperature gives a straight line. At T_C, this line intersects the origin. The $M^2 = 0$ intercept gives the inverse susceptibility $1/\chi_0$ ($H = 0$) while the H/M intercept gives the spontaneous magnetization M_0^2 ($H = 0$).

In real systems near the critical point, non mean field critical exponents are observed. Thus the plot of M^2 *vs.* H/M (Arrott plot) will not necessarily be straight lines, but allows a visual analysis of the data [94]. The T_C determined from the Arrott plot is the isotherm that extrapolates to the origin. Likewise, the extrapolation to the axis intercepts give the $H = 0$ spontaneous magnetization M_0 ($T < T_C$) and inverse susceptibility $1/\chi_0$ ($T > T_C$) and allows a visual exstimation of the error. From these $M_0(T)$ and $\chi_0(T)$ the critical exponents β and γ can be estimated by fitting $M_0(T) \propto (1 - T/T_C)^{\beta}$ and $\chi_0(T) \propto (T/T_C - 1)^{-\gamma}$.

If the assumption of scaling is incorrect, such as a crossover from one scaling region to another as the temperature changes, then the entire data will not scale with the same exponents. In this case, the method described above is better for characterizing the separate regions. Such a crossover is observed in $SrRuO_3$ where β appears to change from 0.32 to 0.38 (Appendix A) so that the entire data does not scale very well with a single average value for β.

3.2.2.2.7 The Curie temperature

Because the Curie temperature affects many of the properties, there are several ways of measuring it. One of the simplest is finding the paramagnetic

Curie temperature, the temperature where the linear extrapolation of the $1/\chi$ curve crosses $1/\chi = 0$. Near the critical temperature however, $1/\chi$ is not necessarily linear in T since $1/\chi = (T - T_C)^{\gamma}$ where γ is usually large than 1. Thus the paramagnetic Curie temperature is usually slightly larger than the true critical temperature.

In principle the thermodynamic critical temperature can be found by fitting the divergence of all the measured quantities and using the scaling relations. This assumes a true critical region has been reached where the critical exponents do not change. The simpler method using the Arrot plots, described in the previous section (3.2.2.2.6) can give as accurate results. Thus, the Arrott T_C is probably the best simple way of finding the critical temperature.

The most basic definition of T_C for a ferromagnet is the temperature where the spontaneous magnetization drops to zero (as the temperature is raised). Unfortunately due to demagnetization effects, the zero applied field magnetization will drop to zero at T_C faster and less uniformly than expected. Nevertheless, the temperature where the magnetization, measured in zero or small applied field, is often used to measure the critical temperature and is called here the remnant T_C.

In an applied field, the magnetization does not drop to zero because of the large susceptibility near T_C. However, below T_C the magnetization has a negative curvature while above T_C it has a positive curvature. Thus the inflection point of the *M vs. T* curve (denoted here as the inflection T_C) is often used to measure the Curie temperature. In the mean field model, the inflection T_C is quite close to the real critical temperature. Figure 3-7 shows the calculated *M vs. T* of $SrRuO_3$ in various fields. In a 5 T applied field, the inflection point is 1.6 K higher than the true T_C used for the calculation. This agrees well with the experimental data shown in Figure 3-9, where the

derivatives are calculated numerically from the measured magnetization. In some systems, the inflection T_C can increase substantially as the applied field is increased, as seen for $Gd_{0.67}Ca_{0.33}MnO_3$ in section 5.1.4, making it a poor estimate of the Curie temperature.

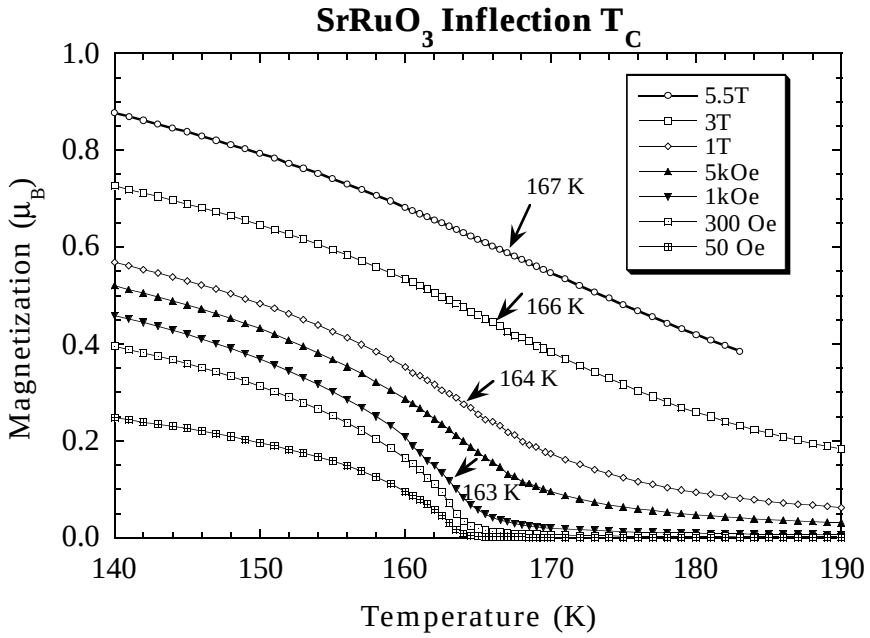

Figure 3-9 The inflection T_C measured for a $SrRuO_3$ pellet. For H < 1 Tesla the inflection T_C is within 1 K of the Arrott T_C = 163 K. At higher H the inflection T_C increases by only a few degrees.

3.2.2.2.8 Spin waves

Collective excitations (spin waves) are expected to be the dominant mode of excitations at the lowest temperatures. This is because it can be shown that collective excitations will always have lower energy than single spin excitations. The spin wave theory has been mostly developed for localized moments [95] but can also be generalized to include *k*-space electrons [81].

The energy ω of a spin wave is given by $\omega = Dk^2 + \Delta$ for low momentum k spin waves. D is the spin wave stiffness and Δ is a gap energy arising from anisotropy or applied magnetic fields. With no gap the spontaneous magnetization decreases as $T^{3/2}$ [95]: $M(T)/M_0 = 1 - (T/\Theta_{3/2})^{3/2}$. For a ferromagnet with spin S and spin density n, $\Theta_{3/2} = \left(\frac{nS}{2.612}\right)^{\frac{2}{3}} \frac{4\pi D}{k_B}$. The specific heat of these excitations [95] also follows a $T^{3/2}$ law: $c_V = 1.925\, k_B nS(T/\Theta_{3/2})^{3/2}$. The spin wave stiffness D may be estimated from the critical temperature T_C and number of near neighbors z, using $D = 2JS^{5/3}$ and $k_B T_C / J = 0.0521(z - 1)(11S(S + 1)-1)$ [96], where J is the exchange energy.

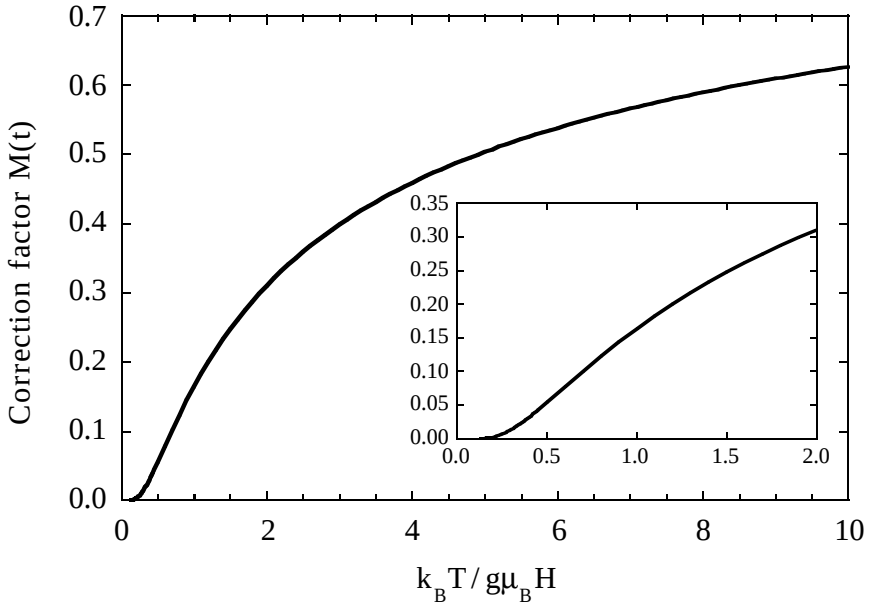

Figure 3-10 Correction factor to the $T^{3/2}$ contribution of the magnetization in the spin wave theory due to a magnetic field H.

The first order effect of a magnetic field providing a gap $\Delta = g\mu_B H / k_B T$, is to adjust the $T^{3/2}$ coefficient by a function of $k_B T / g\mu_B H$: $M(T)/M_0 = 1 - F_{3/2}(k_B T / g\mu_B H)/\zeta(3/2)\ (T/\Theta_{3/2})^{3/2}$. This correction factor $M(t)$, shown in

Figure 3-10, depends on the temperature T, thus altering the temperature dependence of the magnetization to have an effective power higher than 3/2 [97]. The Bose-Einstein integral function [95] $F_P(x)$ is given by $F_P(x) = \sum_{n=1}^{\infty} \frac{e^{-n/x}}{n^P}$ and $\zeta(P) = \sum_{n=1}^{\infty} \frac{1}{n^P}$ (*e.g.* $\zeta(3/2) = 2.612$ and $\zeta(1/2) = -1.460$). The correction $C(t)$ to the $T^{3/2}$ contribution to the heat capacity is similar: $C(t) = [F_{5/2}(t) + 4F_{3/2}(t)/5t + 4F_{1/2}(t)/15t^2)]/\zeta(5/2)$, where $t = k_B T/g\mu_B H$. The correction factor $C(t)$ is shown in Figure 3-11. Due to the Maxwell relation the increase in the effective power in $M(T)$ also increases the effective power of dc/dH (T).

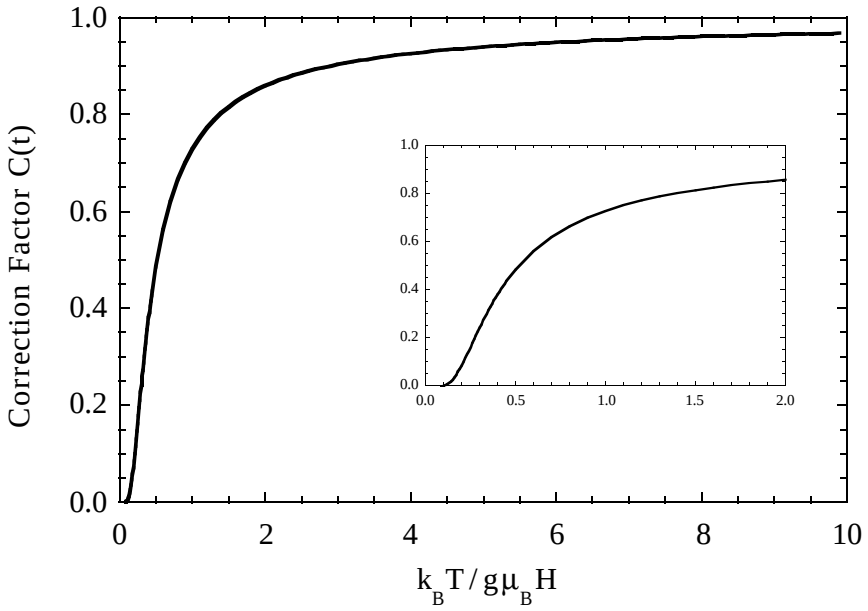

Figure 3-11 Correction factor to the $T^{3/2}$ contribution of the heat capacity in the spin wave theory due to a magnetic field H.

3.2.2.2.9 Irreversibility

Below T_C, a ferromagnet must undergo a first order phase transition when the field direction is changed. Like all first order processes, this involves nucleation and growth (of magnetic domains) and can be hysteretic. Technically there is only hysteresis when the internal field changes sign; if the field increases or decreases while retaining the same sign (direction), the change in the magnetization is continuous. However, in real systems, there exist internal anisotropy and demagnetization fields. So in low fields irreversible behavior can be found.

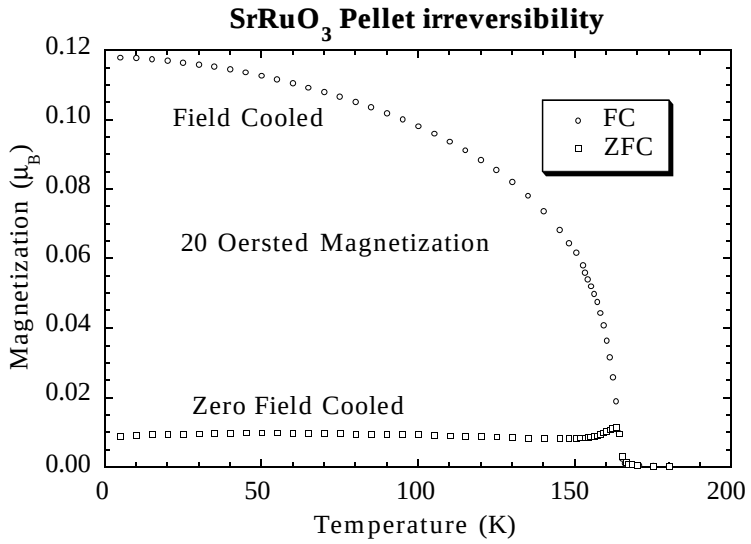

Figure 3-12 $SrRuO_3$ showing spin-glass like irreversibility of zero-field-cooled and field-cooled measurements in a small field. The field cooled curve may look saturated, but is actually less than 1/10 saturated at low temperatures. A small peak is observed in the zero-field-cooled measurement when the reversibility point is reached.

The field required to reduce to zero the magnetization of a saturated sample, is called the coercive field. When the coercive field is large, such as

in polycrystalline $SrRuO_3$, the irreversibility will be evident in many measurements. The coercivity depends on the microstructure of the sample, and therefore depends on the processing. $SrRuO_3$ single crystal for instance (Appendix A) has a coercive field 100 times smaller than polycrystalline $SrRuO_3$.

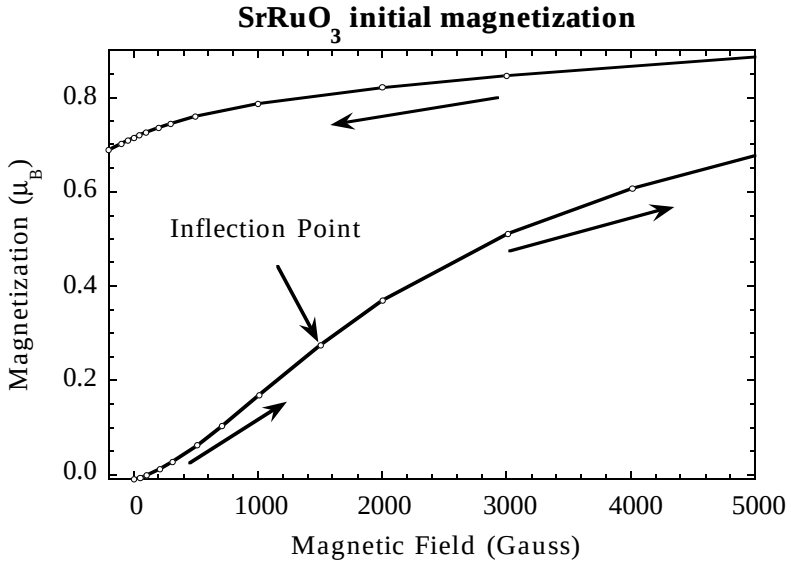

Figure 3-13 Initial magnetization of $SrRuO_3$ pellet at 5 K, after cooling in zero field. The magnetization follows a "S" shaped curve providing an inflection point.

In the irreversible regime, a ferromagnet will have magnetic properties similar to that of a spin glass [98]. For example, it is common to characterize spin glasses [99] (or disordered superconductors) by comparing the field-cooled (sample cooled below T_C in the measuring field) and zero-field-cooled (sample cooled in zero field and then the field applied before measuring upon warming) magnetization in a small field. For a spin-glass or disordered superconductor, these two curves are different. In such small fields, a

ferromagnet will also show such hysteresis, as demonstrated in Figure 3-12 for $SrRuO_3$. The field cooled curve may look like a ferromagnetic *M vs. T* curve, however it is influenced greatly by the demagnetization field and coercivity. For example in applied fields lower than the maximum demagnetization field ($4\pi N M_S$) the net magnetization can only increase until the demagnetization field cancels the applied field ($M = H/4\pi N$). The a plot of *M vs. T* in this case will show a constant, low value for *M*, until the true magnetization decreases near T_C (see for example the low field data in [29]).

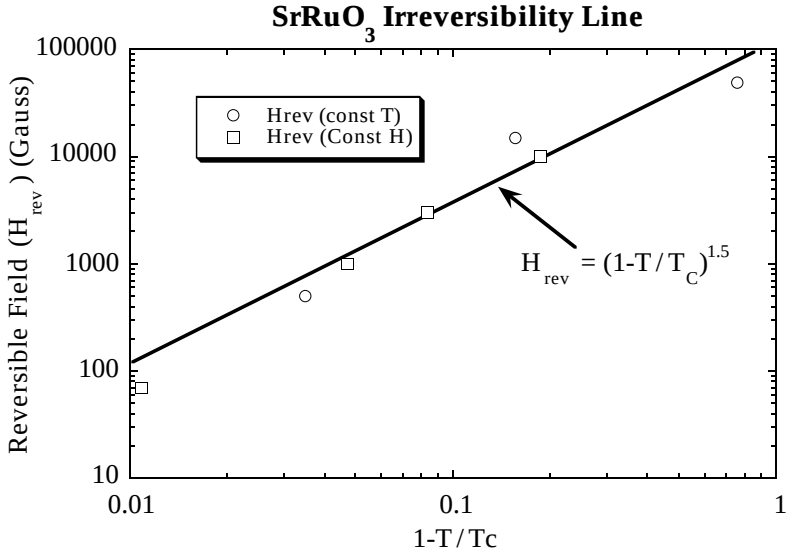

Figure 3-14 Magnetic irreversibility line for polycrystalline $SrRuO_3$. Above the line the magnetization is reversible, below it is irreversible. The irreversibility exponent is about 1.5.

Another characteristic of a spin glass is an "S" shaped magnetization curve, which gives an inflection point in *M vs. H*. Such a curve is also observed for a ferromagnet, such as that seen for $SrRuO_3$ in Figure 3-13. The curves for increasing and decreasing fields will meet at the irreversibility point. The irreversibility points measured by the two methods (constant *T*,

Figure 3-13; and constant *H*, Figure 3-12) give an irreversibility line, much like that in superconductors. For polycrystalline $SrRuO_3$ the reversible field is approximately proportional to $(1 - T/T_C)^{1.5}$.

Like many glassy systems, the magnetic properties in the irreversible region are time dependent. In a ferromagnet the domain walls are pinned and so must overcome some barrier energy to move. Thus the magnetization increases in a time dependent manner. Figure 3-15 shows the magnetization of a $SrRuO_3$ pellet at 5 K after increasing the magnetic field from 0 Gauss (where the magnetization was 0.0076 μ_B) to 100 Gauss. The magnetization increases with a Log(time) dependence, with 98% of the increase happening before the first data point (about 1 minute). Such a logarithmic time dependence is also characteristic of a spin glass [99].

$SrRuO_3$ has all the properties of a ferromagnet, and because of this long range order can not be a spin glass. The domain structure of a ferromagnet provides magnetic disorder on a larger length scale than a spin glass, but to be a spin glass, the disorder must be on the atomic scale.

3.2.2.3 Antiferromagnetism

In an antiferromagnetic substance, the neighboring magnetic moments align antiparallel. Such a material is called an antiferromagnet. In the ordered state, there is often no net moment in zero field. Thus magnetization measurements cannot easily measure the magnetic order. In neutron diffraction, the magnetic unit cell multiplies giving extra diffraction peaks. The intensity of these peaks is a direct measure of the ordering.

In a magnetic field, an antiferromagnet has a small positive susceptibility. Above the ordering temperature, or Néel temperature T_N, the susceptibility can be well described by the Curie-Weiss law used for ferromagnets. Since the interactions are antiparallel, the coupling is of the opposite sign as that for a

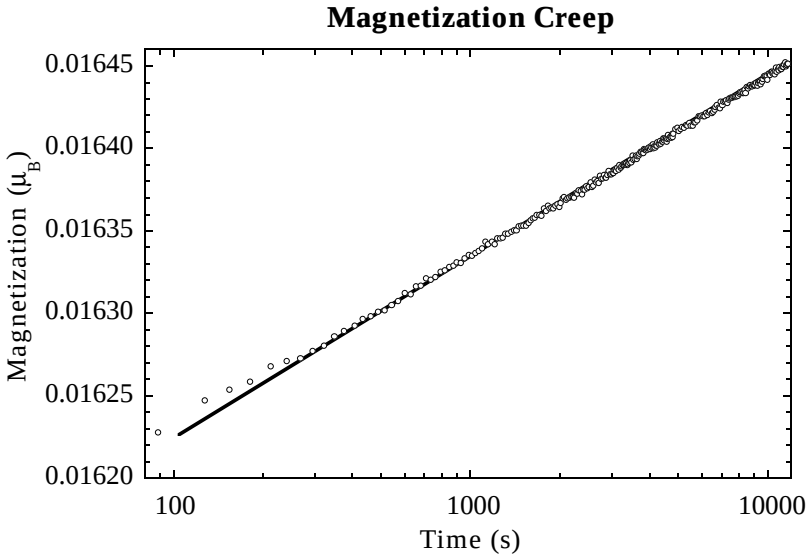

Figure 3-15 Time dependent magnetization of $SrRuO_3$ pellet at 5 K. The field was increased from 0 to 100 Gauss. The magnetization follows a Log(time) dependence.

ferromagnet. This leads to a negative paramagnetic Curie temperature $\Theta_P \approx -T_N$, where the susceptibility above T_N is given by $\chi_{mol} = \frac{N_A \mu_B^2}{3k_B} \frac{g^2 J(J+1)}{T - \Theta_P}$.

Below the ordering temperature T_N, *M vs. H* is still linear with no $H = 0$ magnetization, but the susceptibility depends on the orientation of the magnetic field with respect to that of the magnetic moments [56]. For example, Figure 3-16 shows the susceptibility of platinum containing "$CaRuO_3$" crystals, or $CaRu/PtO_3$ described in section 2.1.2.1. If the magnetic field is applied parallel to the ordered moments, the applied torque ($\mu \times H$) is small so the susceptibility decreases to zero. The $CaRu/PtO_3$ crystal when oriented with the 2-fold symmetric axis parallel to *H* shows such a susceptibility. When the field is perpendicular to the ordered moments, the torque is maximized providing a large, constant susceptibility in the ordered

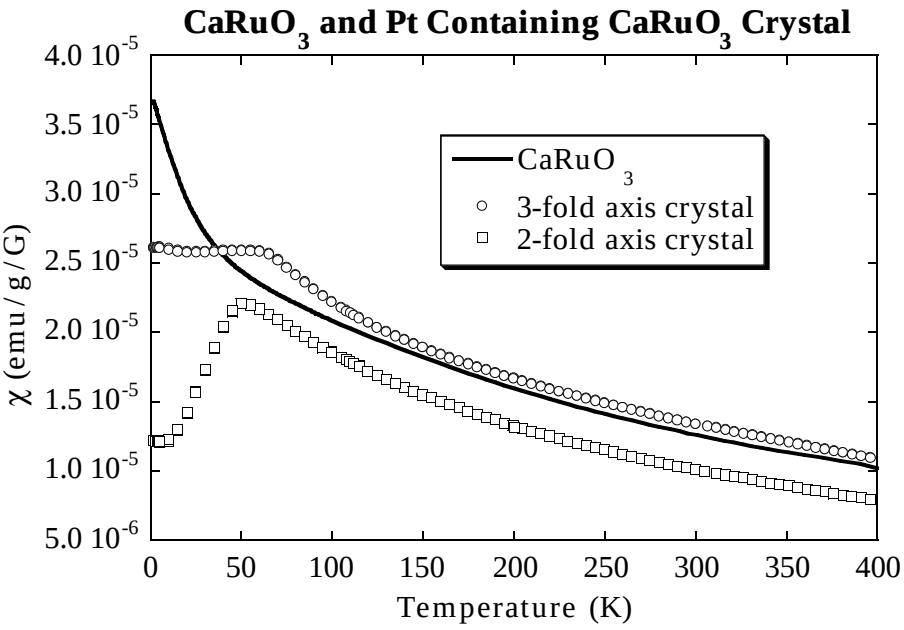

Figure 3-16 Magnetic susceptibility of a Pt containing "$CaRuO_3$" crystal. The crystal was aligned with its 2-fold symmetric axis parallel to the applied field has a susceptibility characteristic of antiferromagnetic moments aligning parallel to the field, while the 3-fold axis appears to have moments perpendicular to the field.

state. This is seen in the crystals oriented with a 3-fold symmetric axis parallel to H. Without Pt, $CaRuO_3$ has an antiferromagnetic like susceptibility ($1/(T + \Theta_P)$) above 50K ($\Theta_P \approx$ -210K $p_{\text{eff}} \approx 9.75$ or $S \approx 1.14$) but does not become antiferromagnetic. Instead, it remains paramagnetic but with a stronger temperature dependence $\approx 1/T$ (Figure 3-16). From 2 K to 20 K the susceptibility fits well to ($1/(T + \Theta_P)$) with an antiferromagnetic slope (Θ_P = -73K $p_{\text{eff}} = 4.17$ or $S = 0.64$).

3.2.2.4 Ferrimagnetism

If the sublattices of different moment orientation do not exactly cancel, there is then a small ferromagnetic moment in the ordered state, that behaves

with temperature and field much like a ferromagnet. When this is due to a canting of neighboring moments from truly parallel or antiparallel, this is called a canted antiferromagnet. If the ferromagnetic moment is not due entirely to canting but arises from the different strengths of the sublattice magnetizations, the material is called a ferrimagnet.

Most commercial insulating "ferromagnets" are actually ferrimagnets. Common examples are ferrites and garnets such as YIG. The multiple magnetic interactions inherent to a ferrimagnet provide a variety a magnetic behavior. For example, when the magnetizations of the opposing sublattices exactly cancel, the net moment is zero like it is in an antiferromagnet. The temperature where this occurs is called the compensation temperature T_{Comp}.

3.2.2.4.1 Mean field model for $Gd_{0.67}Ca_{0.33}MnO_3$

The gross features of a ferrimagnet can be explained using the molecular field model of section 3.2.2.2.5. For a ferrimagnet with two sublattices, the total magnetization M is the sum of the two sublattice magnetizations M_A and M_B. The molecular field acting on each sublattice can then arise from interactions with atoms in the other sublattice as well as atoms in the same sublattice. For example on the A sublattice $H_{mA} = \lambda_{AA}M_A + \lambda_{AB}M_B$. The molecular field constants λ_{ij} can be either positive for ferromagnetic coupling between sublattices or negative for antiferromagnetic coupling. For a ferrimagnet or antiferromagnet, there must be strong antiferromagnetic coupling. Similarly, on the B sublattice $H_{mB} = \lambda_{BB}M_B + \lambda_{AB}M_A$. Once the molecular field constants are known, the magnetization of each sublattice can be calculated iteratively as described in section 3.2.2.2.5 until self consistency is reached.

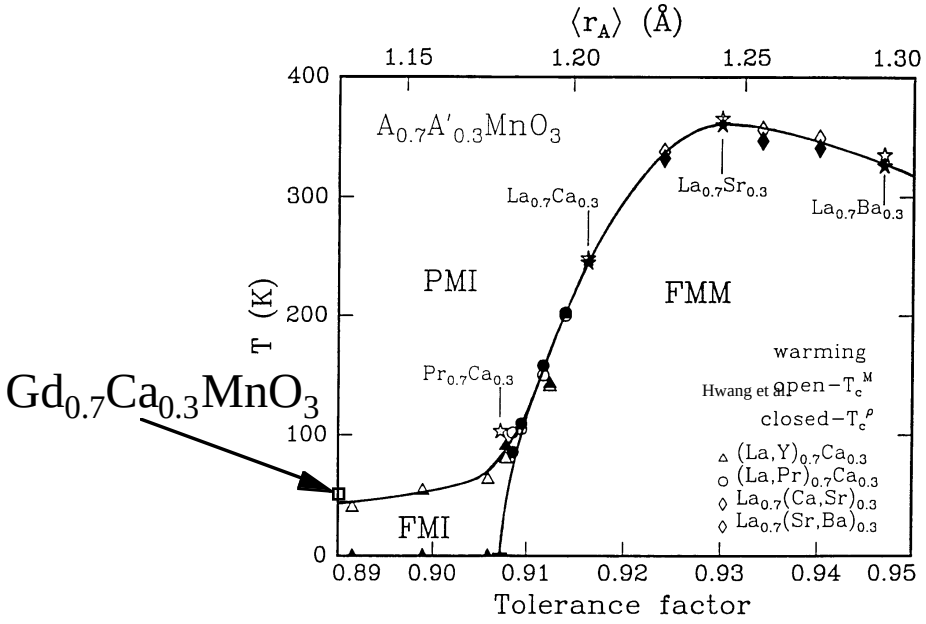

Figure 3-17 Temperature - tolerance factor phase diagram from reference [100], with the position of $Gd_{0.67}Ca_{0.33}MnO_3$ indicated.

This has been done for $Gd_{0.67}Ca_{0.33}MnO_3$ where the experimental results are given in chapter 5. In $Gd_{0.67}Ca_{0.33}MnO_3$ the Mn atoms are on one sublattice (B) and Gd atoms on the other (A). The dominant molecular field constant is expected to be the ferromagnetic Mn-Mn coupling due to the stronger 3*d* exchange interaction. From the trend found in the manganese ferromagnetic ordering temperature as a function of the average of the R and A atom size [100] in $R_{1-x}A_xMnO_3$, shown in Figure 3-17, the T_C is expected to be around 60K. The molecular field constant can then be approximated using the relationship found for a ferromagnet in section 3.2.2.2.5, namely $\lambda_{BB} = 3k_BT_C / \mu_B^2 p_B^2$.

Here p_i^2 also includes the site occupancy for each type of atom on the *i* sublattice. For $Gd_{0.67}Ca_{0.33}MnO_3$, the Mn (B) sublattice has two magnetic contributions since the site is 67% occupied by Mn^{+3} (S = 2) and 33% occupied

by Mn^{+4} ($S = 3/2$). This gives $p_B^2 = \Sigma\, n_i g^2 s_i(s_i + 1) = 21$. On the Gd/Ca (A) sublattice, only Gd^{+3} (67% occupied, $S = 7/2$) has a moment giving $p_A^2 = 42$.

The Gd-Gd interaction is expected to be negligible, and therefore $\lambda_{AA} \approx 0$, since the Gd 4*f* electrons are well localized. The Gd atoms are expected to order due to the significant Gd-Mn interaction which is antiferromagnetic, so $\lambda_{BA} < 0$. In the case of $Gd_{0.67}Ca_{0.33}MnO_3$, there exists a temperature where the magnetization of the larger, but poorly ordered, Gd moments exactly cancels that of the Mn sublattice. This temperature is called the compensation temperature T_{Comp}.

The compensation temperature T_{Comp} can be used to estimate the molecular field constant λ_{BA}. The weakly coupled Gd approximately act like free paramagnetic spins reacting to the internal (molecular) field caused by the ordered Mn moments. In zero applied field this gives $M_A = H_{mA}\, \mu_B^2 p_A^2 / 3k_B T$. The internal field on the A sublattice is related to λ_{BA} from $H_{mA} = \lambda_{BA} M_B$. At $T = T_{Comp}$, there is no net magnetization so $M_B + M_A = 0$. Combining these relations gives $\lambda_{BA} = -3k_B T_{Comp} / \mu_B^2 p_A^2$.

Above T_N, the susceptibility can be calculated analytically [101] giving a hyperbola for $1/\chi$ *vs.* T shown in Figure 5-5. The high temperature asymptote is a straight, Curie-Weiss like, line which intersects the T axis at $\Theta_P = (\mu_B^2 / 3k_B)\,(p_B^4 \lambda_{BB} + 2p_B^2 p_A^2 \lambda_{BA}) / (p_B^2 + p_A^2)$. For $Gd_{0.67}Ca_{0.33}MnO_3$, $\lambda_{BA} < 0$ and $\lambda_{BB} > |\lambda_{BA}|$ so Θ_P should be less than but close to $7\lambda_{BB}\,(\mu_B^2 / 3k_B)$ which is 1/3 of the value that would be expected (T_C of Mn) if no Gd moments were present.

In this model, the ferrimagnetic Néel temperature is given by $T_N = p_B^2 \lambda_{BB}\,(\mu_B^2 / 3k_B)[1/2 + \sqrt{(1/4 + (p_A \lambda_{BA} / p_B \lambda_{BB})^2)}]$ [101]. For $\lambda_{BB} > |\lambda_{BA}|$ this is only slightly greater than the $T_C = p_B^2 \lambda_{BB}\,(\mu_B^2 / 3k_B)$ expected if the Gd moments were absent. Combining this result with that of the last paragraph gives a

general requirement of this model $T_N / \Theta_P > (p_B^2 + p_A^2) / p_B^2 = 3$, which should be easily verified from experiments (section 5.1.5.1).

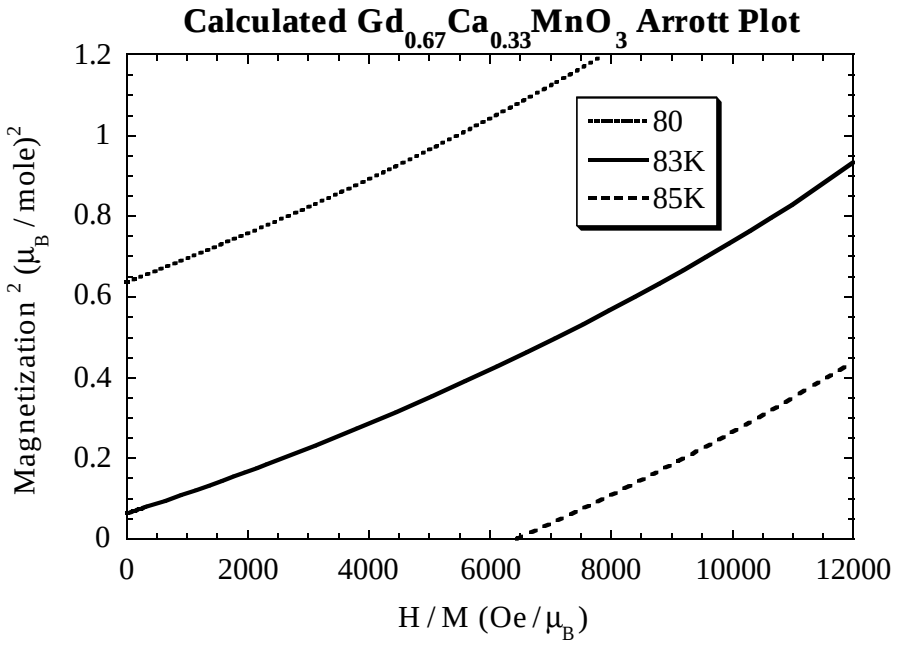

Figure 3-18 Calculated Arrott Plot for $Gd_{0.67}Ca_{0.33}MnO_3$ using the mean field model with T_C = 83.3 K.

The critical temperature T_C, of a ferrimagnet is the Néel temperature T_N. As T approaches T_N from below, the zero field magnetization vanishes much like that of a ferromagnet. The theoretical Arrott plot T_C (shown in Figure 3-18) is equivalent to the remnant $T_C = T_N$. The mean field calculation gives a nearly linear critical isotherm on the Arrott plot, shown in Figure 3-18, since $M^\delta = H$ and $\delta = 3$ is the mean field critical exponent. The inflection point in the *M vs.. T* curve is also a good estimate of T_C. In this model, the inflection T_C increases by only 0.55 K / Tesla as H is increased.

Below T_C the calculated magnetic susceptibility is small since the internal molecular field is quite large. The ferrimagnet susceptibility calculated here, however, is not uniformly decreasing as T decreases like it does for a

ferromagnet. Instead, it peaks as shown in Figure 3-19 near the compensation temperature T_{Comp}.

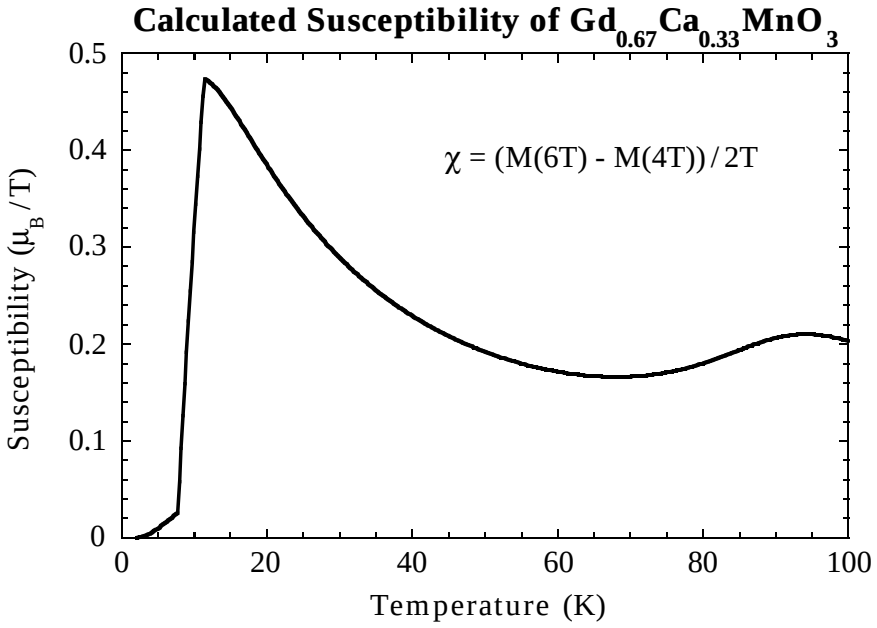

Figure 3-19 High field differential susceptibility for $Gd_{0.67}Ca_{0.33}MnO_3$ calculated using the mean field model. The maximum is at 11.5 K which is near T_{Comp} = 14.2 K in this model.

3.3 Heat Capacity

The heat capacity of a sample, particularly at low temperatures, is a powerful experimental technique which gives fundamental information about low-lying excitations of many kinds (phonons, electrons, magnons, etc.). Microscopic models which describe these excitations typically give quantitative predictions of the specific heat which can then be used to check the theory. The has been quite successful at low temperatures where the excitations are simple. At higher temperatures, the dispersion relation of the excitation spectrum can become less simple and therefore complicate the heat

capacity. Thermal measurements at higher temperatures T>100K are typically only used to study phase transitions.

3.3.1 Measurement

The most straightforward method of measuring heat capacity is adiabatic calorimetry. Here, the heat capacity $C=\Delta Q/\Delta T$ is measured directly by applying a known ΔQ and measuring ΔT. This technique requires that the thermal relaxation time constant between the sample and its surroundings be large compared to the measurement time. In a common Differential Scanning Calorimeter (DSC) or Differential Thermal Analyzer (DTA) the loss of heat due to thermal relaxation is accounted for by subtracting the signal of an empty sample holder measured at the same rate. A DSC actually operates by recording the heat input required $\Delta Q / dt$ to keep the temperature changing at a constant rate $\Delta T/dt$ = constant. The DTA supplies a constant ΔQ and measures ΔT between the sample and a reference. These commercial instruments are used mostly to detect and estimate the entropy associated with a phase transition. Very accurate measurements require a more complicated apparatus with better thermal isolation.

The relaxation technique and ac methods for measuring heat capacity are preferred when measuring a small ΔQ or ΔT. The heat ΔQ is actually calculated in the relaxation technique by measuring the thermal time constant of the system. The sample is attached to an object with high thermal mass and known temperature (the surroundings) by means of a weak thermal link. After heating the sample, the temperature of the sample exponentially decays to that of the surroundings. The heat capacity is then the product of the time constant of this decay and the thermal conductance of the weak link. This thermal conductivity can be measured in the steady state by applying a fixed power and measuring the resulting temperature of the sample.

3.3.1.1 Apparatus

The apparatus, method of operation, data reduction and analysis used at Stanford is described in detail in [102] and references therein. The sample is attached to a bolometer by means of Wakefield thermal compound. The bolometer is a patterned sapphire substrate containing two phosphorus doped silicon thermometers (used for different temperature ranges) and a heater with aluminum contact pads (6). Gold-7%Cu wire of 0.001" diameter is spotwelded to these contacts to mechanically, electrically, and thermally connect the sample containing bolometer to the surrounding sample holder. The gold wire provides the weak thermal link to the surroundings and has a thermal conductivity approximately linear in temperature. The sample chamber is evacuated before the measurement and care must be taken to keep out He since it adds to the thermal conductivity and even the heat capacity if it condenses on the bolometer. The heat capacity due to the sapphire bolometer, thermal compound, gold wire and aluminum contacts (in order of decreasing importance) must be subtracted from the raw heat capacity data. The precision of the measurement is typically 0.5% with or without an applied magnetic field.

3.3.2 Analysis

The specific heat at low temperatures is usually of the form $c = \gamma T + \beta T^3$. Because of this, the data are usually plotted as c/T *vs.* T^2 giving a straight line with slope β and intercept γ.

The specific heat of spin waves are discussed in section 3.2.2.2.8.

3.3.2.1 Electronic specific heat

The linear term comes from the specific heat of itinerant electrons and is proportional to the density of electronic states at the Fermi level, $n(E_F)$. $\gamma = n(E_F)k_B{}^2\pi^2/3$. Insulators and semiconductors have no free electrons and therefore no linear term. Good metals tend to have broad bands with low

density of states, giving a γ of the order 1 $mJ/mol/K^2$. Bad metals tend to have narrow bands and high density of states providing the region of large γ between semiconductors and metals.

3.3.2.2 Phonon specific heat

The cubic term in the specific heat arises from the excitation of phonons in the crystal lattice, and can be related to the Debye temperature Θ_D: $\beta = \Theta_D^{-3} n k_B \, 12\pi^4/5$. The Debye temperature varies like the spring constant between neighboring atoms in the crystal: with Θ_D being very large for light, strongly bonded atoms such as diamond, and small for heavy, weakly bonded atoms such as lead metal. Graphite, which has strong bonding in only two dimensions, has a specific heat over a significant temperature range which is proportional to T^2 instead of T^3.

The Debye model does not account for the specific heat of optical phonons. At higher temperatures this may become important. Using the Einstein model the additional specific heat is proportional to $nk_B \dfrac{(\Theta_E/T)^2 e^{\Theta_E/T}}{(e^{\Theta_E/T}-1)^2}$ where Θ_E is the Einstein temperature.

4. Intrinsic Electrical Transport and Magnetic Properties of $La_{0.67}Ca_{0.33}MnO_3$ and $La_{0.67}Sr_{0.33}MnO_3$ MOCVD Thin Films and Bulk Material

In this study, measurements among polycrystalline pellets, single crystals and thin films, supplemented with literature data when available, are compared to establish the properties inherent to $La_{0.67}AE_{0.33}MnO_3$ where AE = Ca, Sr, Ba or Pb. Whereas most reported $La_{0.67}AE_{0.33}MnO_3$ films have been grown by laser ablation, it is shown here that organometallic chemical vapor deposition (MOCVD) can produce high quality films. It will be demonstrated that singular behavior can be obtained in bulk and thin films. Most of the work described in this section has been previously published [103].

To form the thermodynamically stable phase, the material is annealed at high temperatures for long times and cooled slowly. This produces films, polycrystalline pellets and single crystals with very similar properties. Properties which are common to all these samples are called “intrinsic” to the thermodynamically stable phase. The remaining differences can then be attributed to inhomogeneities, noncrystallinity, microstructure, strain or growth induced effects. Major changes in the magnetization and electrical transport have been observed in $RE_{0.67}AE_{0.33}MnO_{3+\delta}$ compounds (where RE is a rare earth element) when the oxygen stoichiometry was varied; these have been discussed mainly in terms of non-stoichiometry doping and carrier localization [14-17, 104, 105].

In order to compare experimental properties certain terms need to be defined. For simplicity, T_C the used in this chapter is the temperature where the bulk of the zero field magnetization disappears. T_{MI} (metal to insulator temperature) is defined here as the temperature where the resistivity is a maximum. T_{MR} is the temperature where the magnetoresistance (R(0)-R(H))

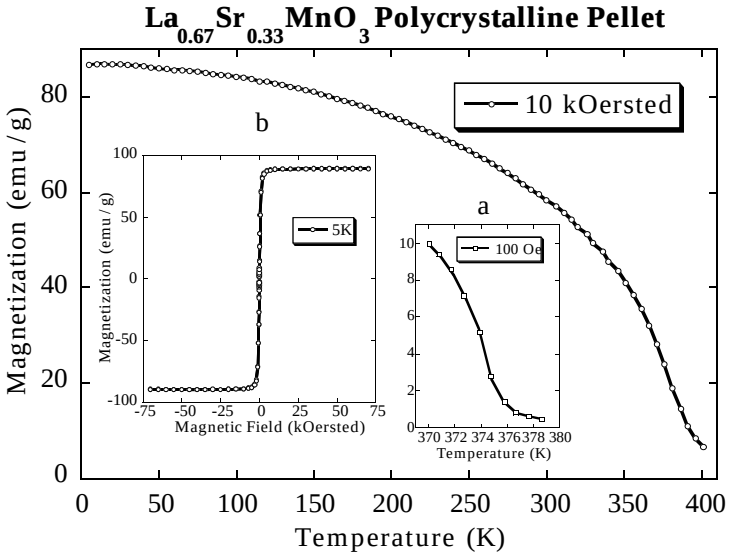

Figure 4-1 Magnetization of $La_{0.67}Sr_{0.33}MnO_3$ polycrystalline pellet at 10kOe. Inset a, magnetization at 100Oe used to determine T_C = 375K. Inset b, full hysteresis loop at 5 K.

is the largest. The term "CMR" is used here when the magnetoresistance ratio $\Delta R/R(H)$ is greater than 10 (or 1000%).

4.1 Magnetism

The polycrystalline samples have relatively square hysteresis loops (Figure 4-1), with forced magnetization at 70kOe of only a few percent. The saturation magnetizations are close to that expected for high spin manganese in octahedral coordination: for spin only (orbital contribution quenched) moment $\mu = gs\mu_b$, g=2 and then $\mu = 2\mu_b[0.67 \times 2$ (from Mn^{3+}) + $0.33 \times 3/2$ (from Mn^{4+})] = $3.67\mu_b$. The measured ferromagnetic and Curie temperatures are the same within experimental error of a few degrees. The physical properties of the polycrystalline materials summarized in Table 4-1 Physical Properties of Polycrystalline Pellets are consistent with previous results [1-4, 29, 106, 107].

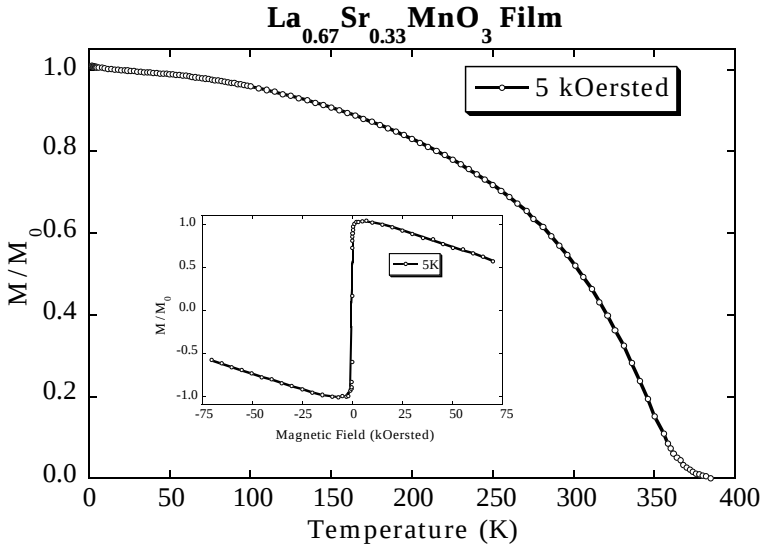

Figure 4-2 Magnetization of $La_{0.67}Sr_{0.33}MnO_3$ film (LSM1) on $LaAlO_3$ at 5kOe. Inset, full hysteresis loop at 5 K of film and (diamagnetic) substrate.

Since the precise oxygen concentration has a noticeable effect on T_C and M_S [104], slight differences are expected. Float zone grown crystals have similar magnetic properties.

Table 4-1 Physical Properties of Polycrystalline Pellets

	$La_{0.67}Sr_{0.33}MnO_3$	$La_{0.67}Ca_{0.33}MnO_3$
T_C	376K	270K
M_S	$3.59\mu_b$ / Mn	$3.39\mu_b$ / Mn
a	3.88Å	3.86Å
H_C	20Oersted	10Oersted
Curie Weiss μ_{eff}	$5.61\mu_b$	$5.96\mu_b$
Hall carrier density (of films)	2.1holes / Mn	0.9holes / Mn

The transition temperatures of the annealed films are close to those of the polycrystalline material, and are summarized in Table 4-2. The saturation magnetization, measured at 5kOe, also decreases as T^2 for both samples. The annealed films exhibit a (5 K) coercivity of about 100 Oe and a sheared hysteresis loop expected from demagnetization or uniaxial anisotropy effects (Figure 4-2 and Figure 4-3).

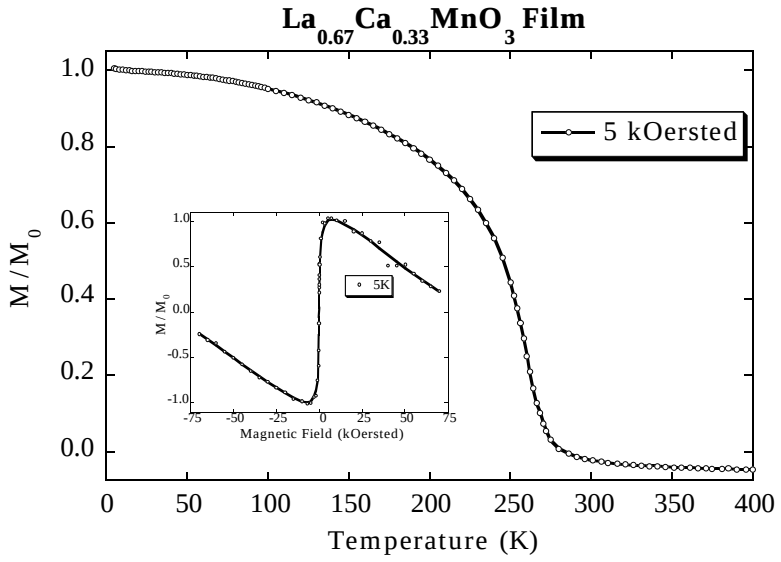

Figure 4-3 Magnetization of $La_{0.67}Ca_{0.33}MnO_3$ film (LCM15) on $LaAlO_3$ at 5kOe. Inset, full hysteresis loop at 5 K of film and (diamagnetic) substrate.

4.1.1 Low Temperature Excitations

The saturation magnetization decreases approximately proportional to T^2 at low temperatures (Figure 4-4). This temperature dependence of M can be expected for metallic ferromagnets as discussed in section 3.2.2.2.2.

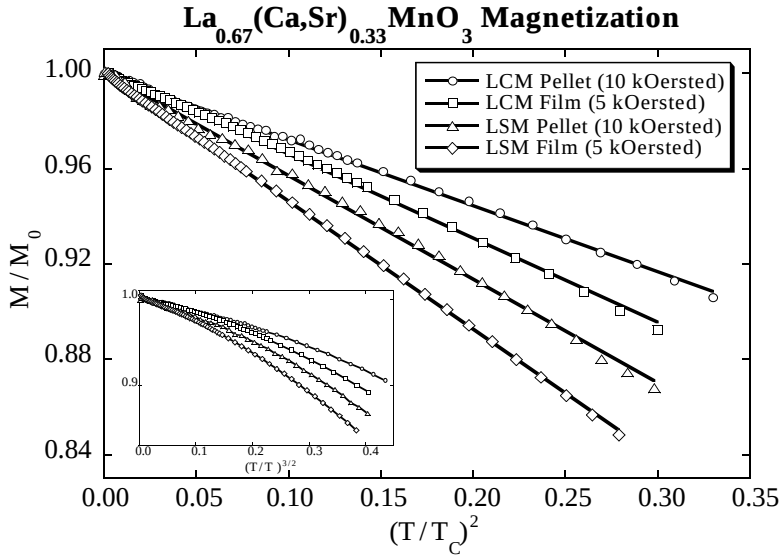

Figure 4-4 Magnetization of $La_{0.67}(Ca/Sr)_{0.33}MnO_3$ films and polycrystalline samples showing the T^2 dependence of the magnetization. Inset, same data as a function of $T^{3/2}$ for comparison.

A T^2 dependence of the magnetization is predicted by the Moriya theory of spin fluctuation in itinerant electron ferromagnets, as shown by a calculation for the weak metallic ferromagnet Ni_3Al [86]. A T^2 dependence has been observed in bulk $SrRuO_3$ (Appendices A and B) which is a metallic ferromagnet with a substantial saturation moment (*i.e.* $p_{sat}/p_{cw} > 0.5$) like the manganites. In the simplest model, a T^2 dependence is due to single (*k*-space) particle spin-flip excitations, while a $T^{3/2}$ law is expected for collective excitations (spin waves). At low temperatures, the $T^{3/2}$ law may be seen in $La_{0.67}Sr_{0.33}MnO_3$ [97] with a stiffness (D = 154 meV or $\Theta_{3/2}$ = 2224 K) also observed in neutron work. This low temperature form is compared in Figure 4-5 with the corresponding data of Figure 4-4 to demonstrate the limitations of this form at higher tem-peratures. The next order term in the spin wave

theory predicts a $T^{5/2}$ con-tribution. Fitting the $T^{5/2}$ parameter $\Theta_{5/2}$, along with the $T^{3/2}$ term fits the data for $La_{0.67}Sr_{0.33}MnO_3$ better up to 300K than a simple T^2 fit. Some samples, such as that shown in Figure 4-5, show an increase in the magnetization at 50 K.

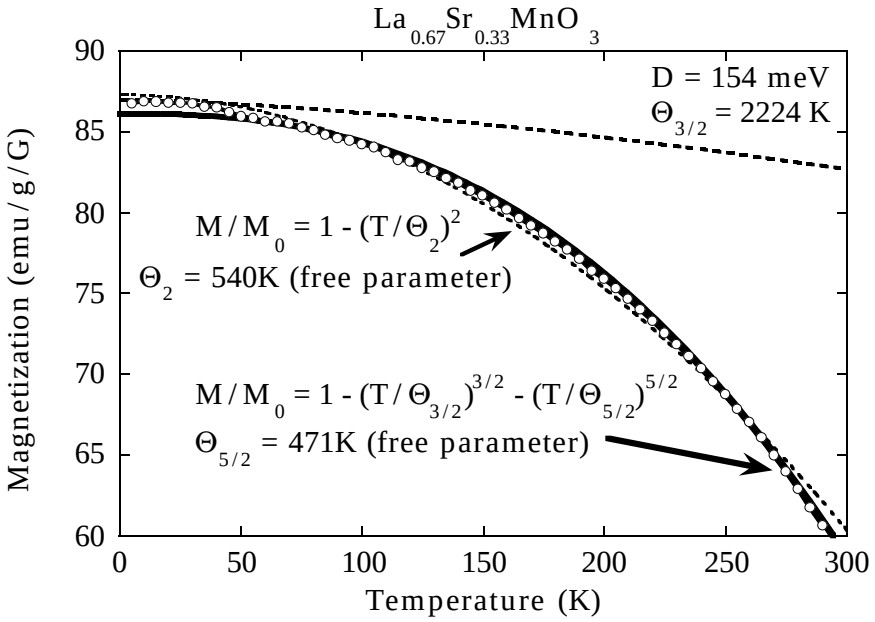

Figure 4-5 Comparison of the magnetization of $La_{0.67}Sr_{0.33}MnO_3$ with the $T^{3/2}$ term found at low temperatures, and various fits to the magnetization.

4.2 Electronic Transport

Both $La_{0.67}Sr_{0.33}MnO_3$ and $La_{0.67}Ca_{0.33}MnO_3$ have an abrupt drop in resistivity below the magnetic Curie temperature in both films and bulk samples (Figure 4-6 and Figure 4-7). The magnetoresistance (Defined as R(0)-R(H)) peaks near the Curie temperature as shown in Figure 4-6 and Figure 4-7 and previous experiments ([29, 104]).

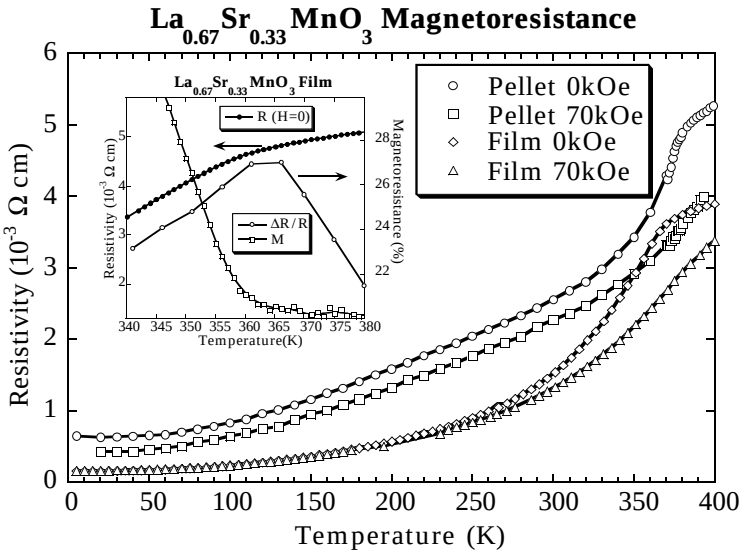

Figure 4-6 Magnetoresistance of $La_{0.67}Sr_{0.33}MnO_3$ polycrystalline pellet and Film (LSM1). Inset, simultaneous magnetization and resistivity of the film at 20Oersted, along with the magnetoresistance [R(*H* = 0 kOe)-R(*H* = 70 kOe)].

4.2.1 Low Temperature Resistivity

Low temperature resistivity data were analyzed using a polynomial expansion in temperature *T*. Since the resistivity is essentially constant for temperatures less than 10K for all samples, it is clear that the resistivity data both with and without an applied field require a temperature independent (R_0) term. As shown previously for related compounds [29, 104, 108], R_0 is a function of magnetization in polycrystalline $La_{0.67}AE_{0.33}MnO_3$ (Figure 4-8) as discussed in section 4.2.8. In contrast, the magnetoresistance of films and crystals at 5 K is over 100 times less: it is not even measurable in the $La_{0.67}Ca_{0.33}MnO_3$ crystal where the precision is 0.5%. Due to the higher resistance of the films, the magnetoresistance at 5 K is measurable and is

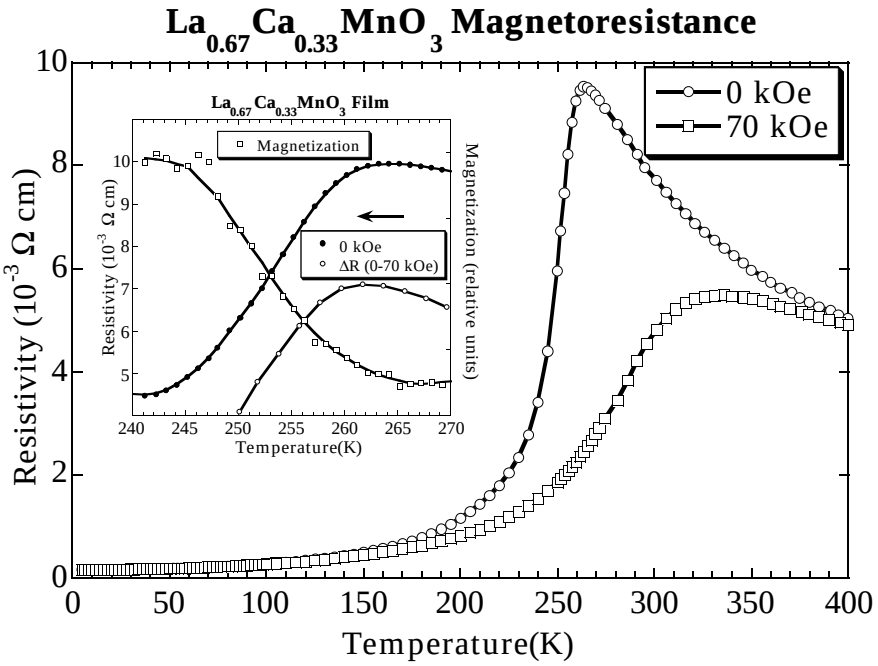

Figure 4-7 Magnetoresistance of $La_{0.67}Ca_{0.33}MnO_3$ film (LCM17). Inset, simultaneous magnetization and resistivity at 20Oersted, along with the magnetoresistance [R(*H* = 0kOe) - R(*H* = 70kOe)].

approximately linear with field (Figure 4-8). This effect is small enough for the analysis to be carried out with R_0 independent of magnetic field.

Since polycrystalline material contains a significant contribution to the resistivity from grain or domain boundaries, as shown by microwave measurements [109-111] and higher R_0 values, analysis of the resistivity data is made only for the well annealed films and crystals. Data up to 70K and 100K for $La_{0.67}Ca_{0.33}MnO_3$ and $La_{0.67}Sr_{0.33}MnO_3$, respectively, are well described with an additional (R_2) term proportional to T^2 (Figure 4-8). A linear term in T did not significantly improve the fit and was not used in later calculations in order to keep the number of free parameters to a minimum. The field

dependence of R_2 is so small (less than 10% variation) it has not been measured.

The range of validity can be extended to about 200K for $La_{0.67}Ca_{0.33}MnO_3$ and 350K for $La_{0.67}Sr_{0.33}MnO_3$ with the addition of a T^n term where $4 < n < 5$. The data was analyzed with a fit to $R_0 + R_2 T^2 + R_{4.5}(H)T^{4.5}$ since a $T^{4.5}$ temperature dependence has been predicted for electron-magnon scattering in the double exchange theory [112]. Evidence for a $T^{4.5}$ term (as opposed to T^4 or T^5) cannot be claimed from this data, only that it allows the determination of the R_0 and R_2 terms to higher accuracy in a much larger temperature range. The maximum temperature for which the data were analyzed was determined by finding the maximum temperature where the free parameters remained stable and the fit was visibly accurate.

The results of this analysis are given in Table 2. As expected, $R_{4.5}(H)$ decreases as the magnetic field increases. In a field of 70 kOe, $R_{4.5}(H)$ decreases by 25-50% (Table 2).

Recently other authors have analyzed the resistivity data for $RE_{0.67}AE_{0.33}MnO_3$ compounds using models different than the one presented above. The resistivity of polycrystalline $La_{0.67}Ca_{0.33}MnO_3$ has been fit to $R_0 + R_c T^c$ [29] while a polynomial fit such as the one used in this work will also fit their data. The $R_0 + R_2 T^2 + R_{4.5} T^{4.5}$ fit, which has the same number of free parameters, is preferable since there seems to be some universality in R_2. The low temperature zero field resistivity of $La_{0.67}Ba_{0.33}MnO_3$ films [109] has been fit to $R_0 + R_1 T + R_2 T^2$, where $R_1 < 0$. R_1 may not have physical meaning even though a small correction is necessary to explain the almost constant resistivity at the lowest temperatures. A dominant T^2 term has been also recently found in the resistivity of single crystals [113].

4.2.1.1 Temperature independent term

The temperature independent term in the resistivity can be ascribed to scattering processes such as impurity, defect, grain boundary and domain wall scattering. From this value, one can make a rough estimate of the (0 K) mean free path of 26Å [56]. The temperature independent term in the polycrystalline samples is somewhat larger than that observed in films or crystals (Figure 4-6, [29]). This indicates a significant grain boundary resistance and/or a significantly restricted conduction path in the polycrystalline samples. The temperature independent terms for the various $La_{0.67}Ca_{0.33}MnO_3$, $La_{0.67}Sr_{0.33}MnO_3$ films and crystals (Table 4-2) concur with recent measurements on other well annealed $La_{0.67}AE_{0.33}MnO_3$ [109, 114, 115] films and single crystals [116]. This limiting resistivity which is largely independent of A-site atoms may be due to the inherent disorder on the A-site.

Table 4-2 Magnetoresistance of Annealed Films.

Sample	T_C (K)	T_{MR} (K)	T_{MI} (K)	R_0 ($10^{-3}\Omega$cm)	R_2/R_0 ($10^{-6}K^{-2}$)	$R_{4.5}(0T)/R_0$ ($10^{-12}K^{-4.5}$)	$R_{4.5}(7T)/R_0$ ($10^{-12}K^{-4.5}$)	E_a/k_B (K)
LSM1[a]	360	365	455	0.15	55	28	15	
LCM X	267	272	275	0.10	102	67	54	849
LCM13	240	250	250	0.10	61	122	87	967
LCM10	260	275	280	0.12	66	85	72	740
LCM15	260	265	265	0.15	73	87	73	725
LCM17	260	262	264	0.16	60	133	82	865
LCM21	240	245	245	0.28	61	114	60	1116
LBM[109]	310	310	330	0.34	52			

4.2.1.2 T^2 dependent term

The T^2 term in the resistivity is also universal with respect to different samples and type of alkaline earth element (Table 2). Furthermore, this term is independent (within 5%) of magnetic field. The significant

[a] LSM = $La_{.67}Sr_{.33}MnO_3$; LCM and LBM are the Ca and Ba analogues. X refers to float zone grown crystals.

magnetoresistance observed in the temperature range used to fit the conductivity data is absorbed primarily in the $T^{4.5}$ term. This universality with respect to growth, composition, and magnetic field leads us to conclude that the T^2 term in the resistivity represents intrinsic behavior of $La_{0.67}AE_{0.33}MnO_3$ compounds.

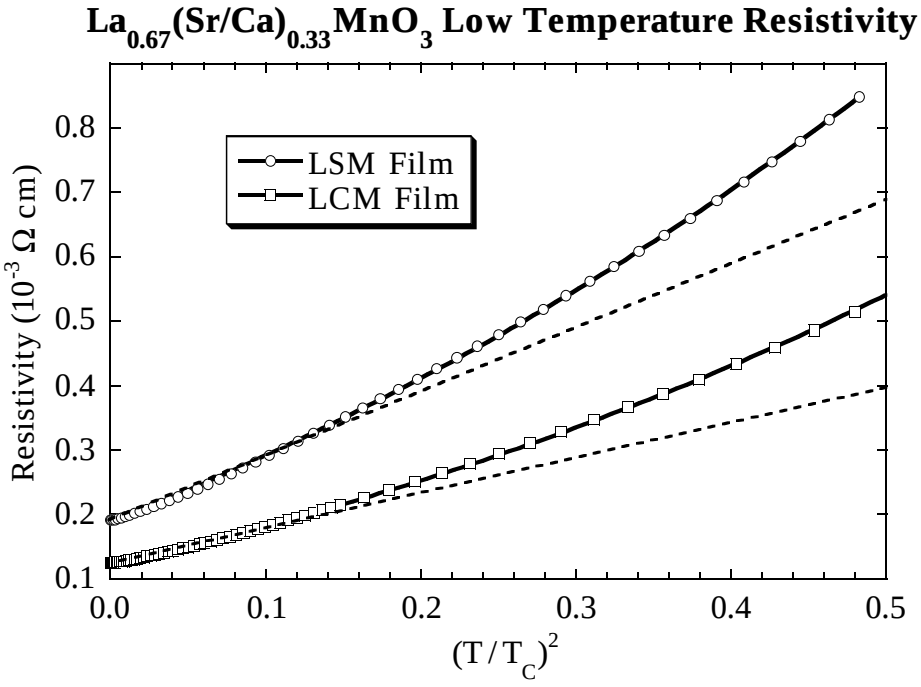

Figure 4-8 Low temperature resistivity (in zero field) of $La_{0.67}(Sr/Ca)_{0.33}MnO_3$ films (LSM1 and LCM10). Solid lines are the fit to $R_0 + R_2T^2 + R_{4.5}T^{4.5}$ up to 250K and 200K for LSM and LCM respectively. The dashed lines show the constant and T^2 terms of the best fit.

Significant T^2 dependencies in resistivity [117] are often observed in metallic ferromagnets such as Fe, Co, and Ni where the coefficient [118] is 10^{-11} $\Omega cm/K^2$. The magnitude of R_2 is expected [84, 119] to scale with $1/M_0$, which explains the larger 5×10^{-8} $\Omega cm/K^2$ value for R_2 found in the weak itinerant

electron ferromagnets Sc_3In and $ZrZn_2$. The term in $La_{0.67}AE_{0.33}MnO_3$ (Table 4-2) is about 1000 times larger than that in Fe, Co and Ni, which have comparable M_0's. Furthermore, the value of R_2 is expected to decrease in a magnetic field (proportional to $H^{-1/3}$) due to the suppression of spin fluctuations; however, the field dependence of R_2 in the manganites is too small for us to detect. Thus the theory of spin fluctuations does not completely explain the observed T^2 dependence of the resistivity.

General electron-electron scattering mechanisms within the Fermi liquid model give a T^2 dependence of the resistivity which is not necessarily field dependent. A value of R_2 as large as that seen in this work has been found in the nonmagnetic semimetal TiS_2 [120].

4.2.1.3 Relationship to magnetism

A quite interesting correlation [114, 115, 121, 122] has been found between the magnetization and the resistivity, namely $\rho = R_e \exp(-M(T, H)/M_r)$ where R_e and M_r are fitting parameters. This is clearly preferable to a polynomial fit in the critical region near T_C. If, at low temperatures, $M = M_0 (1-M_2T^2)$ where M_2 is largely independent of field, then this expression predicts the resistivity will vary as $R_2T^2 + R_4T^4$. Thus a three parameter fit to $\rho = R_e \exp(-M(T, H)/M_r)$ is essentially equivalent to $R_0 + R_2T^2 + R_4T^4$ and therefore fits our data very well. However, this equivalency breaks down when one considers the field dependence: Since both R_e and M_r are independent of field, the field dependence of ρ comes from the field dependence of M_2 which would affect R_2 and R_4 equally. In summary, the exponential fit combined with a T^2 dependence of the magnetization uses four free parameters: R_0, R_e, M_r and $M_2(7T)$ which does not fit the low temperature data as well as the four free parameters R_0, R_2, $R_{4.5}(0T)$, $R_{4.5}(7T)$ used in this work. This is discussed further in chapter 7.

4.2.2 High Temperature resistivity

Above T_C, The zero field resistivity (Figure 4-9) of $La_{0.67}Ca_{0.33}MnO_3$ fit best to $R_h T \exp(E_a / k_b T)$ predicted by small polaron hopping conductivity [123], as opposed to that often used for a semiconductor, $\ln(\rho) \propto 1/T$ (Figure 9). Other (low temperature) forms predicted by variable range hopping [124] or band semiconductor type conductivity were also fit with two parameters to the data with less accurate and less consistent results. In contrast to the Ca and Ba analogs [29, 104] the $La_{0.67}Sr_{0.33}MnO_3$ resistivity (Figure 4-10) does not reach a maximum until about 100K above T_C [16].

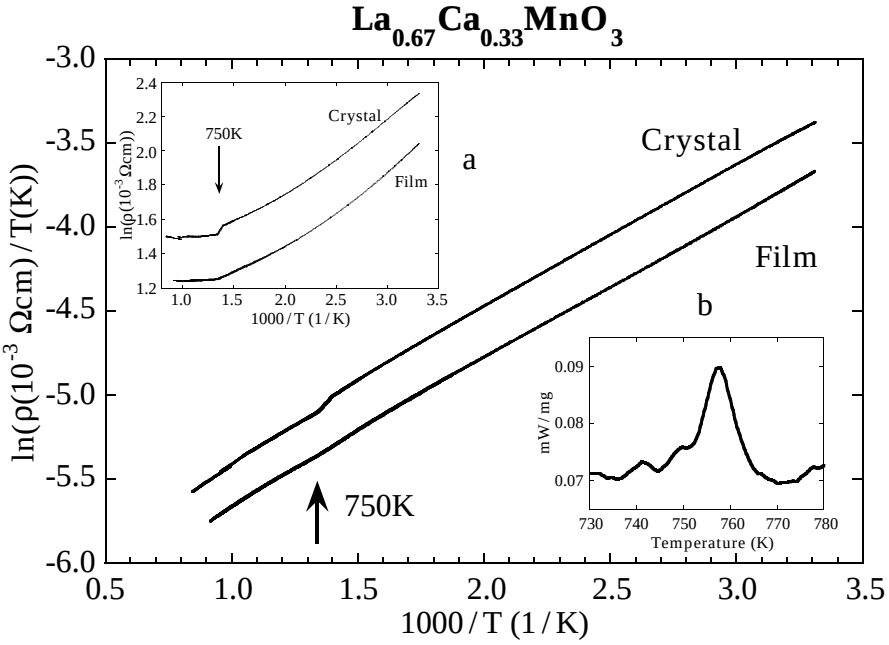

Figure 4-9 High temperature resistivity (warming and cooling) of $La_{0.67}Ca_{0.33}MnO_3$ film (LCM17) and crystal in zero field. Inset a, same data with different abscissa to compare small polaron and semiconductor models. Inset b, DSC trace of polycrystalline $La_{0.67}Ca_{0.33}MnO_3$ showing the heat of the high temperature structural transition.

In the theory of small polaron conductivity, E_a is the hopping energy. The prefactor $R_h \approx k_b / (e^2 a^2 p(1-x)\nu)$ where k_b is Boltzmann's constant, e is the charge of the hole, a is the distance between hopping sites, p is the carrier density, x is the doping fraction (1/3 in this case) and ν is the optical phonon or attempt frequency. A least squares fit of the high temperature data gives a hopping activation energy of 865K and attempt frequency $\nu = 6 \cdot 10^{13}$ / s.

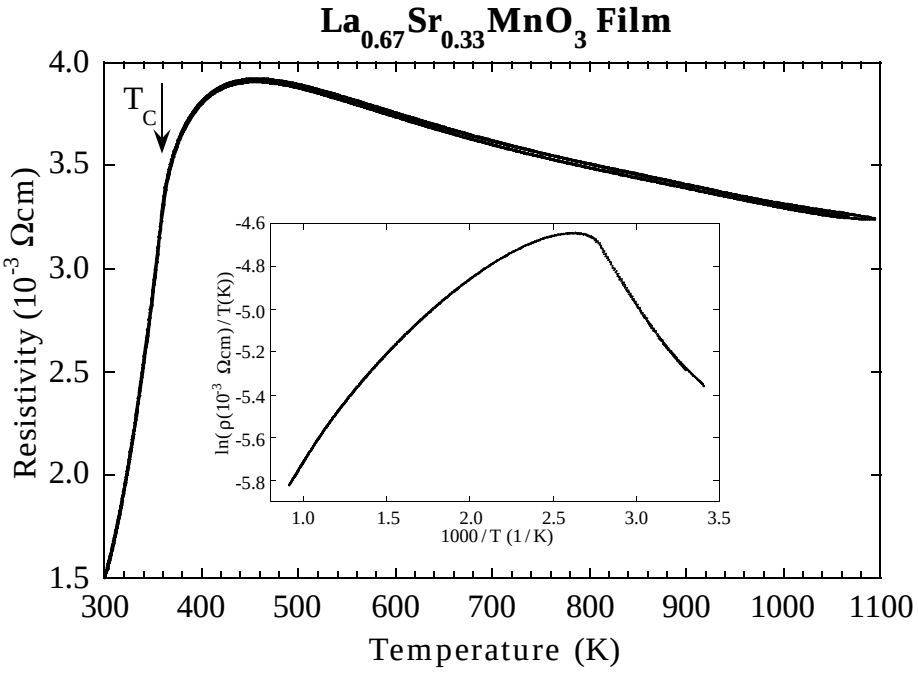

Figure 4-10 High temperature resistivity (warming and cooling) of $La_{0.67}Sr_{0.33}MnO_3$ film (LSM1) in zero field. Inset, same data displayed as in Figure 4-9.

4.2.3 Transport Near T_C

The resistance of $La_{0.67}Ca_{0.33}MnO_3$ reaches a maximum near the Curie temperature whereas that of $La_{0.67}Sr_{0.33}MnO_3$ maximizes about 100K above T_C. This is best seen from simultaneous magnetization and resistance

measurements (Figure 4-6 and Figure 4-7), where there is no error in relative temperature. Both $La_{0.67}Ca_{0.33}MnO_3$ and $La_{0.67}Sr_{0.33}MnO_3$ have $T_{MR} \approx T_C$ within a few Kelvin. For $La_{0.67}Ca_{0.33}MnO_3$ T_{MI} is approximately equal to $T_C \approx T_{MR}$. $La_{0.67}Sr_{0.33}MnO_3$ however shows a much more gradual transition to a hopping conductivity-like transport with T_{MI} (approximately 455K) well above T_C = 360K.

At T_C a maximum in $d\rho(H=0)/dT$ is expected for a metallic ferromagnet [125]. This is observed for both compounds studied within experimental uncertainty. The added resistance at a ferromagnetic Curie temperature is due to electron scattering off thermally disordered spins and, particularly in the case of the manganites, polaron formation. Since a magnetic field can easily suppress spin fluctuations in the critical region, the resistance associated with magnetic disorder will be reduced in a magnetic field. In a good metal such as Fe or $SrRuO_3$ [126] this normally is a small effect of about a few percent. It has been shown theoretically that this effect is much larger for a semimetal (or semiconductor) at T_C, particularly within the double exchange model [8, 125, 127, 128]; however, it has been recently been pointed out that double exchange alone can not account for the large magnetoresistance [10, 11]. Nevertheless, such an explanation has been used to explain the magneto-transport properties of semiconducting magnetic chalcogenides [129] such as EuO [130], Gd_2S_3 [131], and various spinels [129, 132-135] where the resistance may drop by several orders of magnitude at T_C.

4.2.4 Hall effect

The Hall effect data at 5 K (Figure 4-11) were analyzed according to the equation $R = R_0 + H \cdot R_H + |H| \cdot R_{MR}$, where R_H is the Hall resistance and R_{MR} is the magnetoresistance. The contribution due to the anomalous Hall effect was not detected at this temperature. From the simple single band interpreta-

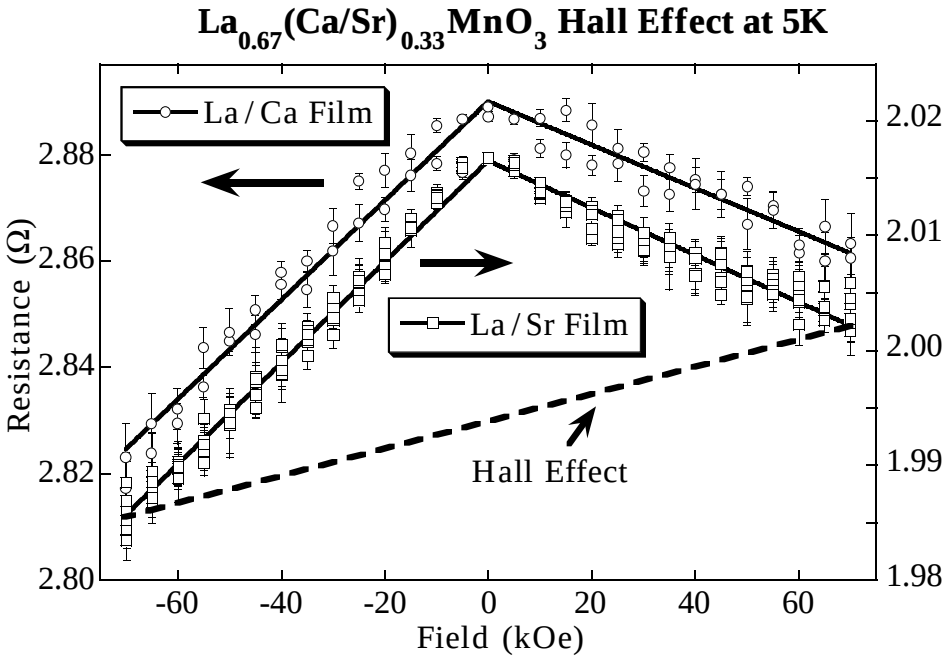

Figure 4-11 Resistance as a function of field $La_{0.67}(Ca/Sr)_{0.33}MnO_3$ films (LSM1 and LCM19) in the Hall effect configuration at 5 K. The Hall effect is calculated from the slope of the line indicated (see text).

tion of the Hall effect [56], our measurements at 5 K show hole conductivity with concentrations of the expected order of magnitude (Table 1).

Because the Hall effect is so small and conduction appears to proceed via small polaron hopping, it is concluded that the temperature dependence of the resistivity is due to the temperature dependence of the mobility while the carrier concentration remains relatively constant.

Since $LaMnO_3$ is a high spin d^4 insulator, the e_g orbitals must be split, possibly by the Jahn-Teller effect. Thus doping with an alkaline earth element on the La site, should put mobile holes in the lower e_g state. The magnitude of the carrier concentration calculated from the Hall effect is

somewhat too large compared with the above model and therefore such a simple interpretation is clearly inadequate.

4.2.5 Crystallographic Phase change

At 750K, a nearly discontinuous jump as well as a significant change in slope is observed in the resistivity. The jump is much more noticeable in the crystals indicating a structural transition which is suppressed to some extent by the epitaxy in the thin films. This transition has been confirmed by differential scanning calorimetry (Figure 4-9). An orthorhombic to rhombohedral transition is seen in at low temperatures in $La_{0.83}Sr_{0.17}MnO_3$ [126].

A change in slope is only noticeable in the $\ln(\rho)$ vs. $1/T$ plot but not in the $\ln(\rho/T)$ vs. $1/T$ plot. This indicates that the change in $d\rho/dT$ can be interpreted within the small polaron hopping conductivity model [62]. Below 750K thermally activated hopping of the charge carriers dominates the conductivity, while above 750K scattering of these carriers begins to dominate.

4.2.6 Small Polarons

The presence of small polarons implies the existence of local lattice distortions which localize the charge carriers. A Jahn-Teller distortion about the Mn^{3+} ion is expected from its d^4 configuration in an octahedral environment. It has been postulated that such a distortion is necessary to explain the magnetoresistivity of these compounds [10, 11].

Above T_C the resistivity of $La_{0.67}Sr_{0.33}MnO_3$ may be explained by a crossover between two types of polaron conduction [116]. Just above T_C the polarons are heavy free carriers scattered by phonons, which gives a positive $d\rho/dT$. Quantitatively, this is expected to add a term to the conductivity proportional to $\exp(-T/\Theta_D)/T$ [62]. At T_{MI}, which should be about half the Debye temperature (Θ_D), the phonon scattering becomes so strong that the mean free path is about one lattice spacing, and therefore localizes the

carriers. Above T_{MI} the polarons conduct via thermally activated hopping, which has a negative $d\rho/dT$. Although this qualitatively explains the data, the quantitative predication of the temperature dependence does not fit the data very well.

4.2.7 Colossal Magnetoresistance

In general, manganite films reported in the literature which exhibit CMR as shown in Figure 4-12 [21, 23, 26, 127, 128]: 1) do not have square hysteresis loops at low temperatures, leading some to believe superparamagnetic behavior exists in those materials; 2) have ill-defined T_C's which are much less than those reported for the bulk materials with the same nominal composition; 3) have T_{MI} well below T_C, with T_{MR} slightly less than T_{MI}; and 4) have high resistivities in the metallic state, at low temperatures.

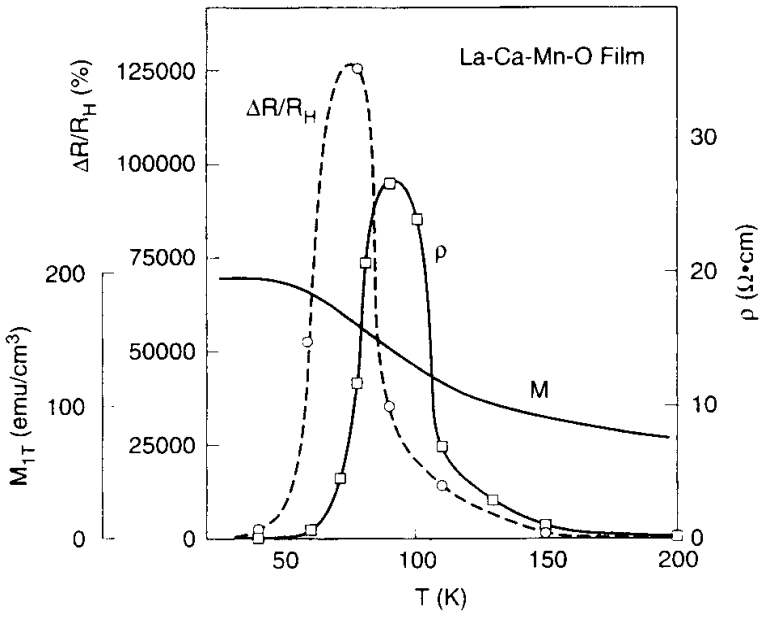

Figure 4-12 Colossal magnetoresistive $La_{0.67}Ca_{0.33}MnO_3$ film from [21, 127].

The annealed films in this study (which do not exhibit CMR) are much like bulk polycrystalline or single crystal material: They are clearly itinerant

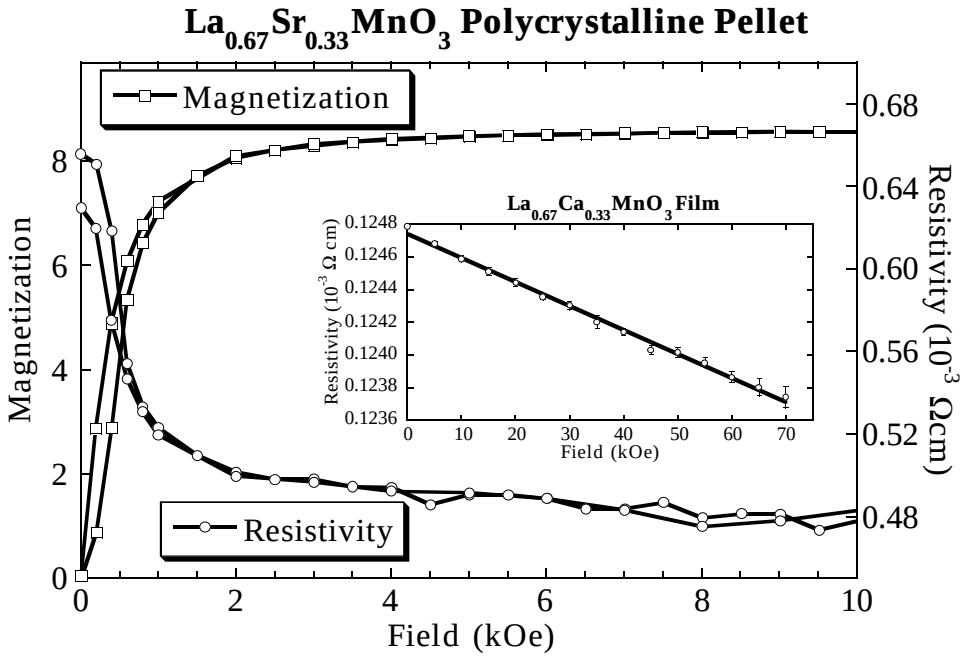

Figure 4-13 Simultaneous magnetization and resistivity in a magnetic field of $La_{0.67}Sr_{0.33}MnO_3$ polycrystalline pellet at 5 K. Data for both increasing and decreasing field are shown. Inset, Magnetoresistance of $La_{0.67}Ca_{0.33}MnO_3$ film (LCM10) at 5 K.

electron ferromagnets with reasonably square hysteresis loops, T^2 dependence of the saturation magnetization and sharp T_C's. They have T_C and T_{MR} all approximately equal and along with T_{MI} are comparable to those of the bulk polycrystalline material. Finally, the films have low resistivities like those observed in single crystals [104, 109, 114, 129-131]. It is therefore concluded that these films are displaying properties inherent to $La_{0.67}(Sr/Ca)_{0.33}MnO_3$ and less influenced by microstructure, strain, and/or compositional variations than films with suppressed T_C and CMR.

If one assumes that the resistivity behaves as $T\exp(E_a/k_BT)$ above T_{MI} and at least R_2T^2 in an infinite field below T_C, then the maximum magnetoresistance

($\Delta R/R(H)$ at $T = T_{MR} = T_{MI}$) follows $\exp(E_a/k_B T_{MI})/(T_{MI})$. This predicts "colossal" magneto resistance only at low temperatures, as a consequence of the depressed T_{MI}. Such a strong dependence of the magnetoresistance on a film's particular T_{MI} has been documented (Appendices A and B) from the various values reported in the literature.

4.2.8 Domain Boundary Magnetoresistance

The negative magnetoresistance associated with the domain orientation is only observed in polycrystalline samples [28, 96]. If this is due to domain wall scattering, then films and crystals with fewer domain boundaries would be expected to show a much smaller effect. It has been concluded that spin-polarized inter-grain tunneling is responsible for this effect [132].

4.2.9 Low temperature magnetoresistance

The low temperature negative magnetoresistance linear in H is very small in the films but somewhat larger in the polycrystalline samples (Figure 4-13, and [28, 96]). This negative magnetoresistance may be due to the M^2 dependence of the resistivity described in section 7.2.4 [129, 130] combined with a small forced magnetization. Classic magnetoresistance of metals is generally positive but is often negative in ferromagnets.

4.3 Conclusion

Well annealed MOCVD thin films show properties of bulk $La_{0.67}Ca_{0.33}MnO_3$ and $La_{0.67}Sr_{0.33}MnO_3$. The limiting low temperature resistivity of 0.2 mΩcm, which gives a mean free path of roughly 20Å, is independent of alkaline earth element and only slightly dependent on field for single crystal material (bulk or film). The manganites show a significant T^2 dependence of the resistivity which is also independent of alkaline earth element and magnetic field. The maximum in the magnetoresistance occurs at the Curie temperature, which is not necessarily where $d\rho/dT$ changes sign, but where $d\rho/dT$ is a maximum. A large magnetoresistance can occur well

above room temperature, but the effect decreases significantly with temperature.

Three regions of magnetoresistance are identified in these materials. The largest effect is likely due to the suppression of magnetic critical scattering near the Curie temperature. There is also a negative magnetoresistance associated with the net magnetization of polycrystalline samples but not seen in single crystal materials. Finally there is a small negative magnetoresistance linear in field even at low temperatures.

The compounds $La_{0.67}Ca_{0.33}MnO_3$ and $La_{0.67}Sr_{0.33}MnO_3$ are metallic ferromagnets with large saturation moments. The saturation magnetization is found to decrease proportional to T^2.

The high temperature resistivity of $La_{0.67}Ca_{0.33}MnO_3$ clearly follows the law predicted by small polaron hopping conductivity both in the thermally activated regime and at higher temperatures where scattering becomes important. There appears to be a structural transition at about 750K.

The resistivity of $La_{0.67}Sr_{0.33}MnO_3$ above the Curie temperature shows a crossover from a metallic to a hopping regime at higher temperatures.

In conclusion, the CMR effects in materials of the same compositions as those studied here but with much lower transition temperatures, are not intrinsic to the thermodynamically stable phase. Local inhomogeneities or noncrystallinity in not fully annealed films may suppress the magnetic and metal-insulator transitions. This presumably causes the observed superparamagnetic type magnetism and conduction via percolation.

5. Local Structure, Transport and Rare Earth Magnetism in the Ferrimagnetic Perovskite $Gd_{0.67}Ca_{0.33}MnO_3$

In order to examine the nature of the metal-insulator transition in the CMR manganites, the distorted perovskite $Gd_{0.67}Ca_{0.33}MnO_3$ related to $La_{0.67}Ca_{0.33}MnO_3$ was studied. The composition $x = 1/3$ was chosen because this doping concentration should maximize the double exchange effect as seen in the lanthanum compounds [29]. Due to the small size of the Gd^{3+} ion, $Gd_{0.67}Ca_{0.33}MnO_3$ should be in the region of the $x = 1/3$ phase diagram where there is no transition to a metallic state, but to a ferromagnetic insulating state around 50K [100]. The ferromagnetic nature of this low temperature state has recently been questioned due to evidence of a spin glass behavior with no long range ferromagnetic order in $(Tb_xLa_{1-x})_{0.67}Ca_{0.33}MnO_3$ [136]. The x-ray-absorption fine-structure (XAFS) technique can detect small variations of the average local environment about a particular atomic species, making it ideal for studying subtle structural phase transitions associated with any metal-insulator or ferromagnetic transitions. The Mn *K*-edge (6.54 keV) and Gd L_{III}-edge (7.25 keV) are well enough separated that there is little interference of the Mn and Gd XAFS.

In this study, it is found that the rare earth moments in $Gd_{0.67}Ca_{0.33}MnO_3$ order antiparallel to the manganese giving rise to ferrimagnetism. Furthermore, not only does this material remain insulating when it becomes magnetically ordered, but no structural difference exists between the ferrimagnetic and paramagnetic state. This is consistent with models that require a structural change, as well as the ferromagnetic ordering of the manganese atoms, to explain the metal-insulator transition and the large magnetoresistance that accompanies it. Most of the work presented in this chapter has been previously published [137].

5.1 Ferrimagnetism

The polycrystalline pellets, crystals and thin films all display a ferromagnetic transition and a compensation temperature (Figure 5-1), which is characteristic of ferrimagnets. Both bulk materials, polycrystalline pellet and float zone crystal, have very similar magnetic properties while the film is slightly different.

$Gd_{0.67}Ca_{0.33}MnO_3$ displays the properties of a ferrimagnet, much like the garnet ferrite $Gd_3Fe_5O_3$ [138]. At about 60K, the transition metal spins order, dominating the magnetization. As the temperature is lowered, the opposing magnetization of the weaker coupled rare earth ions increases, since they behave almost as though they were free paramagnetic spins reacting to an internal field (section 5.1.3, Figure 3-19).

At the compensation temperature, T_{Comp}, the rare earth and transition metal sublattice magnetizations exactly cancel (in zero field). Below T_{Comp}, the magnetization of the rare earth ions, which have larger spins, dominates. This is best seen in zero field remnant data which shows the magnetization changing sign at T_{Comp}.

In the presence of magnetic fields greater than the coercive field, the stronger sublattice flips to align parallel with the field, giving the minimum in M at T_{Comp} as seen the 5 kOe data.

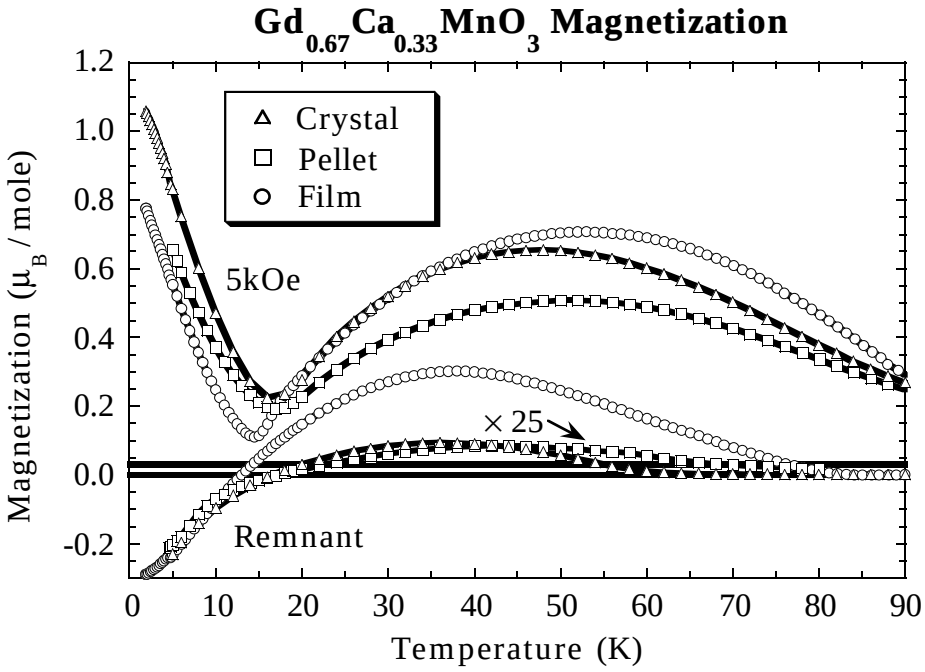

Figure 5-1 Low temperature magnetization of $Gd_{0.67}Ca_{0.33}MnO_3$ measured in a 5 kOe field and zero field after cooling in a large field (remnant).

5.1.1 Low temperature moment

The saturation magnetization per mole of $Gd_{0.67}Ca_{0.33}MnO_3$ expected from the Gd^{3+} $S = 7/2$, $l = 0$ is $\mu=(0.67 \times 2 \times 7/2)\ \mu_B = 4.67\mu_B$, while high spin manganese gives spin only (orbital contribution quenched) $\mu = gS\mu_B$, $g = 2$ so $\mu = 2\mu_B[0.67 \times 2$ (from Mn^{3+}) $+ 0.33 \times 3/2$ (from Mn^{4+})$] = 3.67\mu_B$. The simple two sublattice (Gd and Mn) ferrimagnetism described above predicts a zero temperature saturation magnetization of 4.67 μ_B - 3.67 μ_B = 1.00 μ_B (if there is any canting of the sublattices such as that in $Pr_{0.67}Ca_{0.33}MnO_3$ [139], a smaller moment is predicted). This is roughly what is observed. The mean field

calculation predicts a constant moment for $T < 5$ K, while the data show an almost linear change in M for 2 K < T < 5 K. Also, the peak in the magnetization, observed at about 50 K in the 5 kOe data is less than the $1.9\mu_B$ predicted in the mean field calculation.

5.1.2 High temperature susceptibility

Susceptibility data (Figure 5-2) above 200 K fit to the Curie-Weiss law: $\chi = \mu_{eff}^2/(8(T-\Theta))$ with $\Theta = 34$ K and $\mu_{eff}^2 = 71\ \mu_B^2$. The difference in the susceptibility of the crystal compared to that of the pellet at high temperatures may not be significant. For quantum mechanical spins μ_{eff}^2 per mole is expected to be $63\ \mu_B^2$: $2^2\mu_B^2(0.67 \times 4/2 \times 6/2) = 16\ \mu_B^2$ from Mn^{3+}; $2^2\mu_B^2(0.33 \times 3/2 \times 5/2) = 5\ \mu_B^2$ from Mn^{4+}; $2^2\mu_B^2\ (0.67 \times 7/2 \times 9/2) = 42\ \mu_B^2$ from Gd^{3+}. This extra moment, which is also observed in $La_{0.67}Ca_{0.33}MnO_3$ [103] section 4.1, may be due to the orbital contribution in the manganese ions. Since the two sublattices have different coupling energies, the susceptibility above T_C will not obey a simple Curie-Weiss law even in the mean field approximation (Figure 5-5). The simple mean field model of the above ferrimagnetism requires $T_C/\Theta > 3$, as described in section 3.2.2.4.1. This is clearly not the case for the measured parameters. Alternatively, the addition of a Pauli-like susceptibility χ_0 to the fit, $\chi = \chi_0 + \mu_{eff}^2/(8(T-\Theta))$, will reduce the contribution from μ_{eff}. For example, an equally good fit to the data can be found with $\mu_{eff}^2 = 63\ \mu_B^2$, $\chi_0 = 7.7 \times 10^{-6}$ emu G^{-1} g^{-1}, and $\Theta = 50$ K.

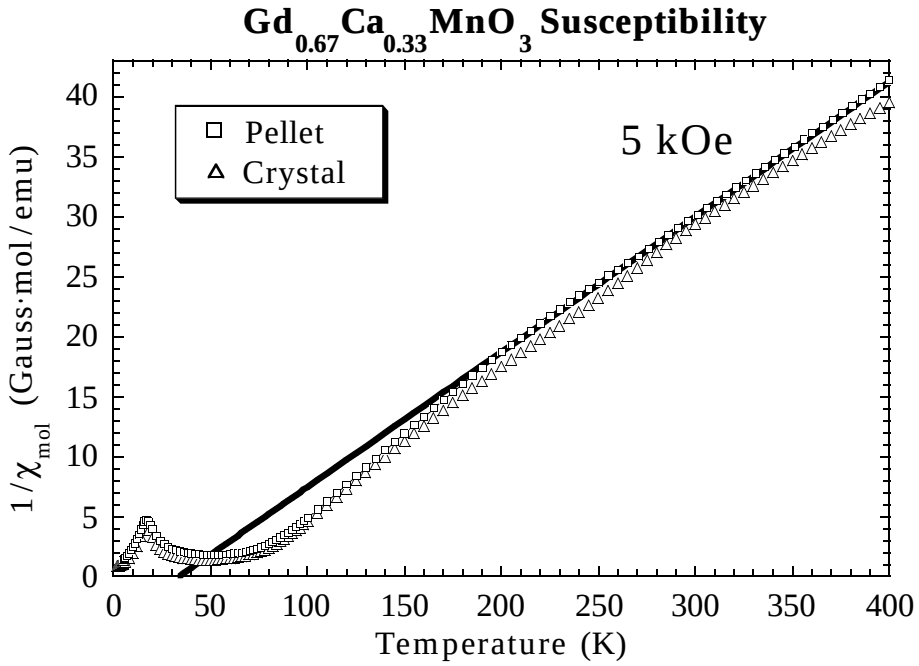

Figure 5-2 Inverse magnetic susceptibility of bulk $Gd_{0.67}Ca_{0.33}MnO_3$. Solid line is the high temperature fit to $\chi = \mu_{eff}^2/(8(T-\Theta))$ described in the text.

5.1.3 Low temperature susceptibility

Between T_{Comp} and T_C, the magnetic susceptibility essentially that of the paramagnetic-like rare earth moments, showing an approximate $\chi \propto 1/(T + T_{Comp})$. Below T_{Comp} the Gd^{3+} moments effectively order antiferromagnetically with respect to the manganese moments, and so the susceptibility decreases below T_{Comp}.

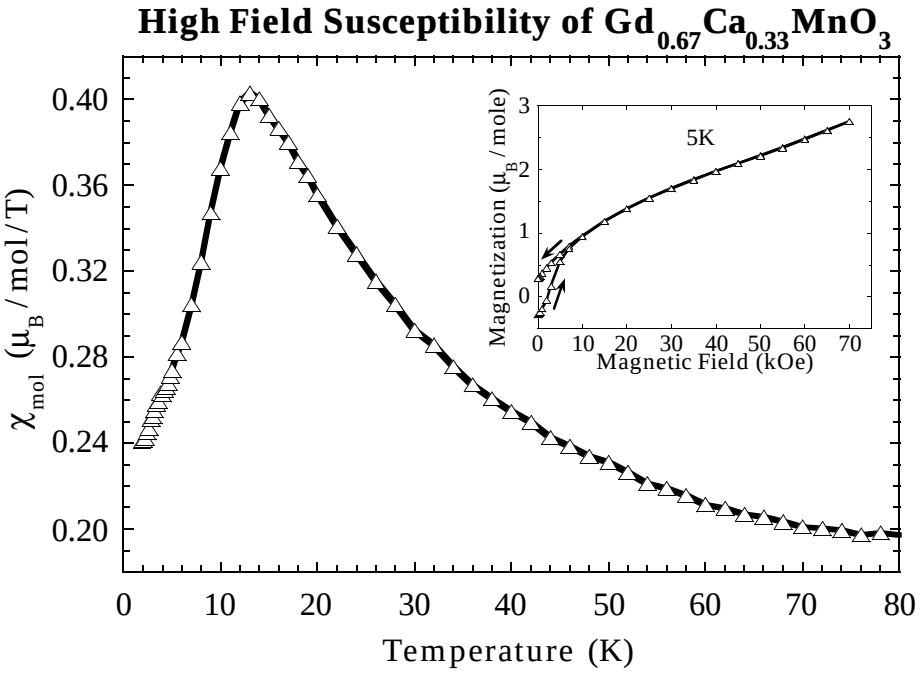

Figure 5-3 Low temperature and high-field magnetic susceptibility, χ = (*M*(60 kOe)-*M*(40 kOe))/20kOe, of $Gd_{0.67}Ca_{0.33}MnO_3$ crystal. Inset, hysteresis loop at 5 K.

The hysteresis loop at 5 K (Figure 5-3) shows an additional high field paramagnetic response not expected for a mean field ferrimagnet. It is not uncommon, however, to observe such a field-induced increase of the magnetization in canted ferromagnetic or ferrimagnetic systems [140, 141], and is used as evidence of the ferrimagnetic sublattices canting away from antiparallel [101]. The magnetic field affects the canting angle, which results in the magnetization increasing nearly linearly with field even at T = 0 K [140]. If this large susceptibility were due to a second phase with free paramagnetic spins, then this phase would have to contain at least half of the available spins and have a $1/T$ temperature dependence for all T. This is not

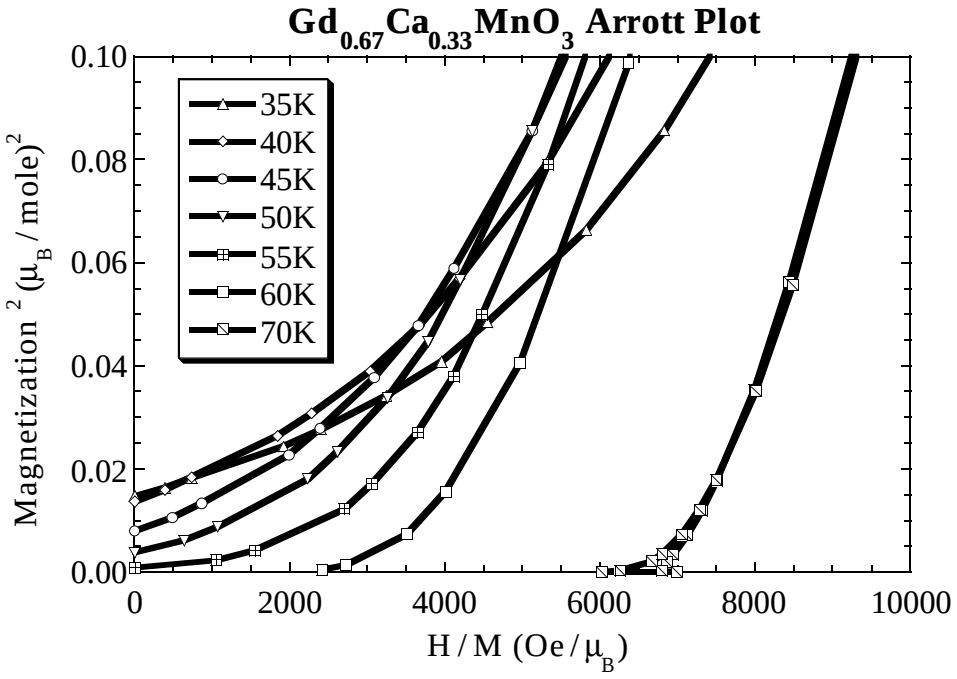

Figure 5-4 Arrott plot of polycrystalline $Gd_{0.67}Ca_{0.33}MnO_3$ pellet.

seen in Figure 5-3. Instead, the high field susceptibility maximizes near T_{Comp} which is typical of an antiferromagnet with $T_N \approx T_{Comp}$. This is predicted in the mean field calculation for a ferrimagnet described in section 3.2.2.4.1.

5.1.4 Near T_C magnetism

The experimental values of T_C are summarized in Table 5-1. An example

Table 5-1 Transition Temperatures for $Gd_{0.67}Ca_{0.33}MnO_3$.

	T_{Comp}	Arrott T_C	Remnant T_C	Inflection T_C
Polycrystalline Pellet	17K	52K	60K	80K
Single Crystal	17K	56K	62K	78K
Thin Film	13K	70K	81K	88K

of the nonlinear M^2 *vs.* H/M Arrott plot is given in Figure 5-4.

5.1.5 Magnetism model

To explain the magnetism, a mean field model was used assuming a ferrimagnetic ground state. Other possible explanations for the magnetism in $Gd_{0.67}Ca_{0.33}MnO_3$ are briefly discussed

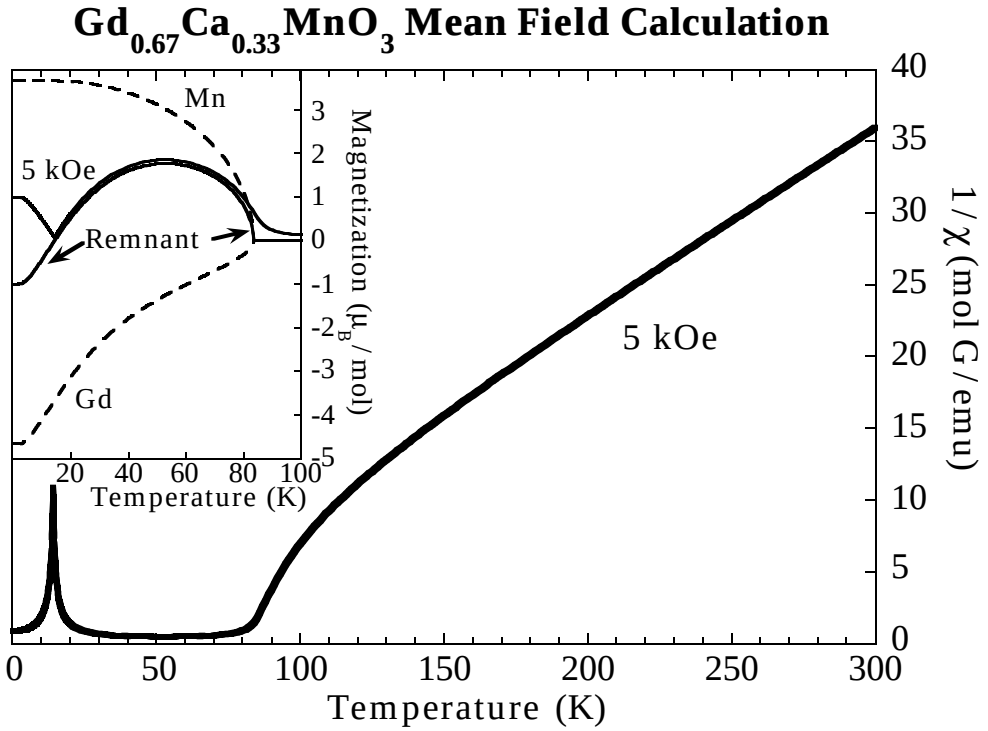

Figure 5-5 Magnetization and inverse magnetic susceptibility calculated for $Gd_{0.67}Ca_{0.33}MnO_3$ using the simplified mean field theory described in the text and T_C = 83 K, T_{Comp} = 17 K. The contribution to the magnetization of each sublattice is shown in dashed lines.

5.1.5.1 Mean Field Model

Due to the stronger 3*d* exchange interaction compared to that of the 4*f*, the Mn-Mn coupling is expected to be stronger than the Mn-Gd, and the Gd-Gd interaction to be negligible. Since the observed Curie temperature is about

that expected from the trend found in the manganese ferromagnetic ordering temperature as a function of the average of the R and A atom sizes in $R_{1-x}A_xMnO_3$ [100], it is assumed for now that the Mn-Mn interaction in $Gd_{0.67}Ca_{0.33}MnO_3$ is ferromagnetic. The ferrimagnetism must then arise from a weaker, antiferromagnetic Mn-Gd interaction. Thus, unlike the ferrites, where the dominant interaction is antiferromagnetic between the two transition metal sublattices, the strongest magnetic coupling in $Gd_{0.67}Ca_{0.33}MnO_3$ is ferromagnetic, much like that found in the rare earth cobaltites, *e. g.* $GdCo_5$ [142].

The above description of the magnetization can be bolstered using a simple molecular or mean field model described in section 3.2.2.4. Assuming that all atoms on each sublattice (Mn or Gd) feel the same mean field, there are only two unknown mean field coefficients due to the Mn-Mn and Mn-Gd interactions. These two coefficients are easily determined since they are nearly proportional to T_C and T_{Comp}, respectively. This molecular field model (Figure 5-5) reproduces the qualitative features described above.

The calculated magnetization and inverse susceptibility for the molecular field model described below is shown in Figure 5-5.

This model is limited by the obvious simplifications: not only are there two distinct types of Mn atoms (Mn^{3+} and Mn^{4+}), but there are numerous possible configurations for the number and type of near neighbors due to the randomness on the Mn and Gd/Ca sites. The discrepancy among the various values of T_C determined by the three methods mentioned is an example of non-mean-field ferromagnetic behavior. The discrepancies in the salient features discussed above may result from the simplifications of the model, and the assumptions behind it.

5.1.5.2 Canted antiferromagnetism

The evidence concerning the magnetic structure of the manganese in the ferromagnetic insulator phase points to a canted antiferromagnetic structure

rather than a simple ferromagnet. The magnetic structure of $Pr_{0.67}Ca_{0.33}MnO_3$ which is on the boundary between ferromagnetic-insulator and ferromagnetic-metal low temperature phases [100], has been extensively studied. Neutron diffraction shows $Pr_{0.67}Ca_{0.33}MnO_3$ to have a charge-ordered, canted-antiferromagnetic structure in the low temperature phase with ferromagnetic moment about half of the total expected moment [139, 143]. A compound clearly in the ferromagnetic-insulator part of the tolerance-factor phase-diagram (Figure 3-17), much closer to $Gd_{0.67}Ca_{0.33}MnO_3$ than $Pr_{0.67}Ca_{0.33}MnO_3$ is $La_{0.2}Y_{0.5}Ca_{0.3}MnO_3$. This compound appears to be ferromagnetic with about half the expected ferromagnetic moment [100], which could be explained by a canted antiferromagnetic state similar to that found in $Pr_{0.67}Ca_{0.33}MnO_3$. Thus, one should expect the ferromagnetic moment of the Mn ions in $Gd_{0.67}Ca_{0.33}MnO_3$ to be half that predicted in the above molecular field model. If the Gd moments are also canted to the same degree, then the predicted magnetization will be qualitatively the same for the uncanted case (Figure 5-5), only half the magnitude; namely, there will still be a compensation temperature.

5.1.5.3 Spin glass magnetism

Atomic disorder such as that found on both the Gd and Mn site in $Gd_{0.67}Ca_{0.33}MnO_3$ can result in a spin-glass, and indeed a spin-glass insulating low-temperature phase was found in $(Tb_xLa_{1-x})_{0.67}Ca_{0.33}MnO_3$ in place of the ferromagnetic insulator state. The compound $Tb_{0.67}Ca_{0.33}MnO_3$ should be in the same region of the tolerance-factor phase-diagram as $Gd_{0.67}Ca_{0.33}MnO_3$ and $La_{0.2}Y_{0.5}Ca_{0.3}MnO_3$. The Tb compound is apparently a pure spin-glass with no long-range magnetic order [136]. A full investigation of the existence or non-existence of spin-glass behavior in $Gd_{0.67}Ca_{0.33}MnO_3$ is beyond the scope of this work. However, it is clear that $Gd_{0.67}Ca_{0.33}MnO_3$ has long range magnetic order, which eliminates the possibility of a spin glass. The distinction is most obvious in the Arrott plot (Figure 4), which shows that $Gd_{0.67}Ca_{0.33}MnO_3$ has a

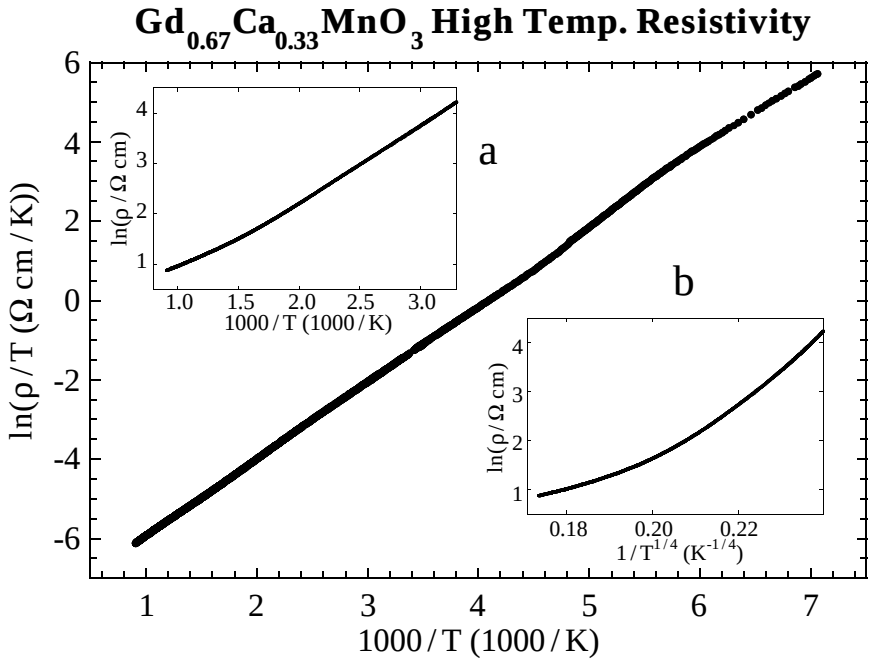

Figure 5-6 High temperature resistivity during heating and cooling a $Gd_{0.67}Ca_{0.33}MnO_3$ film, *ln*(ρ/*T*) vs. 1/*T*. Inset a, comparison with *ln*(ρ) vs. 1/*T*. Inset *b*, comparison with *ln*(ρ) vs. $1/T^{1/4}$.

non-zero magnetization when $H = 0$ below T_C, while $(Tb_{0.33}La_{0.67})_{0.67}Ca_{0.33}MnO_3$ does not [136]. The other striking feature of $Gd_{0.67}Ca_{0.33}MnO_3$ is the existence of a compensation point, which to our knowledge cannot be explained by a spin-glass magnetic system.

5.1.5.4 Related Compounds

Since Gd^{3+} has the largest spin of the rare earth elements, it should have the highest ordering temperature. If the relevant exchange interaction is due to spin-spin coupling of the rare earth and manganese atoms, then the strength of this interaction will be proportional to the spin *S* of the rare earth

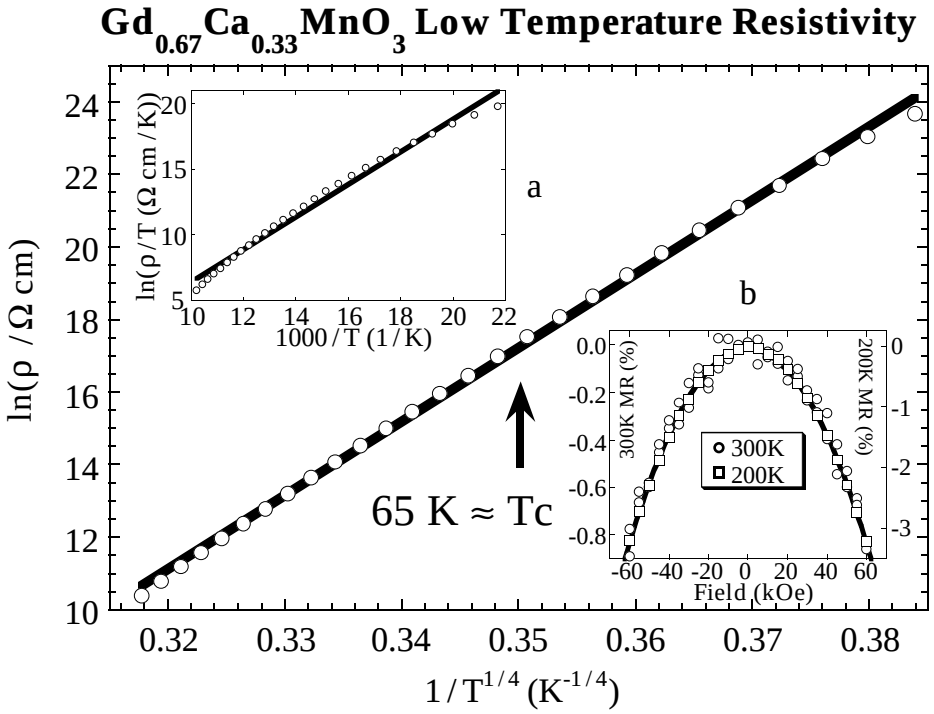

Figure 5-7 Low temperature resistivity of $Gd_{0.67}Ca_{0.33}MnO_3$ crystal, *ln(*ρ) vs. $1/T^{1/4}$. Inset *a*, comparison with *ln*(ρ/*T*) vs. 1/*T*. Solid lines show linear best fit to the data shown. Inset *b*, magnetoresistance of a film at 200 K and 300 K; solid line is the quadratic fit.**

ion. From this relation the ordering temperature of the rare earth moments in related compounds is estimated to be about 7 K for $Nd_{0.67}Ca_{0.33}MnO_3$ and 5 K for $Pr_{0.67}Ca_{0.33}MnO_3$. This should result in a decrease in M at low T. This appears at temperatures lower than these estimates, if at all [23, 144]; perhaps indicating an interaction strength proportional to S^2, the square of the rare earth spin, or simply that these moments do not order antiparallel to the manganese moments [145].

5.2 Electronic Transport

The resistivity can be well approximated by $R_h T\exp(E_a/k_B T)$ (Figure 5-6), predicted by small polaron hopping conductivity [68, 146]. Below about 150 K (Figure 5-7), the resistivity is somewhat better described by $R_0\exp(T_0/T)^{1/4}$, which is commonly attributed to variable range hopping [123]. The quantitative aspects of the fits is discussed below. The thin film and crystal samples show no transition to a metallic state down to 5 K.

5.2.1 Magnetoresistance

No extraordinary magnetoresistance was observed in the entire temperature range. The magnetoresistance at 200 K and 300 K is a few percent in a 70 kOe field and approximately proportional to H^2 (Figure 5-7). Reliable resistivity data could be measured on the crystal sample down to 40 K. No discontinuity in the resistivity was found near T_C.

5.2.2 Small Polaron Hopping

The electrical resistivity of $Gd_{0.67}Ca_{0.33}MnO_3$ is consistent with adiabatic small polaron hopping conductivity (section 4.2.6)$R_h T\exp(E_a/k_B T)$ [58, 68] $R_h = 2k_B/3ne^2a^2\nu$ particularly at high temperatures. Here, k_B is Boltzmann's constant, e is the electronic charge, n is the number density of charge carriers — about 0.7 carrier per Mn, a is the site-to-site hopping distance, and ν is the longitudinal optical phonon frequency. This behavior has also been observed in the La containing compound described in section 4.2.2 [103, 146]. Resistivity data are often displayed on an Arrhenius plot ($ln(\rho)$ *vs.* $1/T$) which will give a straight line for a band gap semiconductor [15, 147]. The slightly different temperature dependence of the data provides the significant nonlinearity in such a fit (Figure 5-6). A polaron hopping activation energy, E_a, of 1940K, and an attempt frequency of 8×10^{13} s^{-1} is inferred. The small polaron mechanism implies that unlike a bandgap semiconductor, the highly temperature dependent quantity is the mobility, not the carrier concentration.

A high, temperature independent carrier concentration is consistent with Hall effect measurements (sect 4.2.4) on $La_{0.67}Ca_{0.33}MnO_3$.

5.2.3 Variable Range Hopping

The resistivity of the manganites has also been attributed to variable range hopping due to Anderson localization [148]. At temperatures less than 150K, this picture produces a somewhat better fit to our data (Figure 5-7), but is clearly inferior to the polaron model at high temperatures (Figure 5-6). The fit to $R_0\exp(T_0/T)^{1/4}$ gives $T_0 = 1.7 \times 10^9$ K. In the theory of variable range hopping [71, 149], $k_B\ T_0 \approx 21/(\zeta^3 N(E_F))$ where ζ is the decay length of the localized wave function, and $N(E_F)$ is the density of localized states at the Fermi level. For $\zeta \approx a = 3.9$Å, the distance between neighboring Mn atoms, this implies $N(E_F) \approx 2.4 \times 10^{18}$ eV^{-1} cm^{-3} which is typical for disorder semiconductors but about 1500 times less than the density of states found in the specific heat of manganites which become metallic at low temperatures (≈ 5 mJ mol^{-1} K^{-2})[124].

5.3 X-ray Absorption Fine Structure

The primary quantity in XAFS data analyses is $\chi(k)=(\mu(k)-\mu_0(k))/\mu_0(k))$, where k is the ejected photoelectron wave vector, $\mu(k)$ is the total absorption due to the absorbing atomic species, and $\mu_0(k))$ is the portion of $\mu(k)$ that does not include the photoelectron backscattering off neighboring atoms. This backscattering causes an interference at the absorbing atom which is manifest as oscillations in $\chi(k)$. A Fourier transform of $k\chi(k)$ thus produces peaks that correspond to the distribution of atoms around the absorbing atom. Figure 5-8 shows these Fourier transforms.

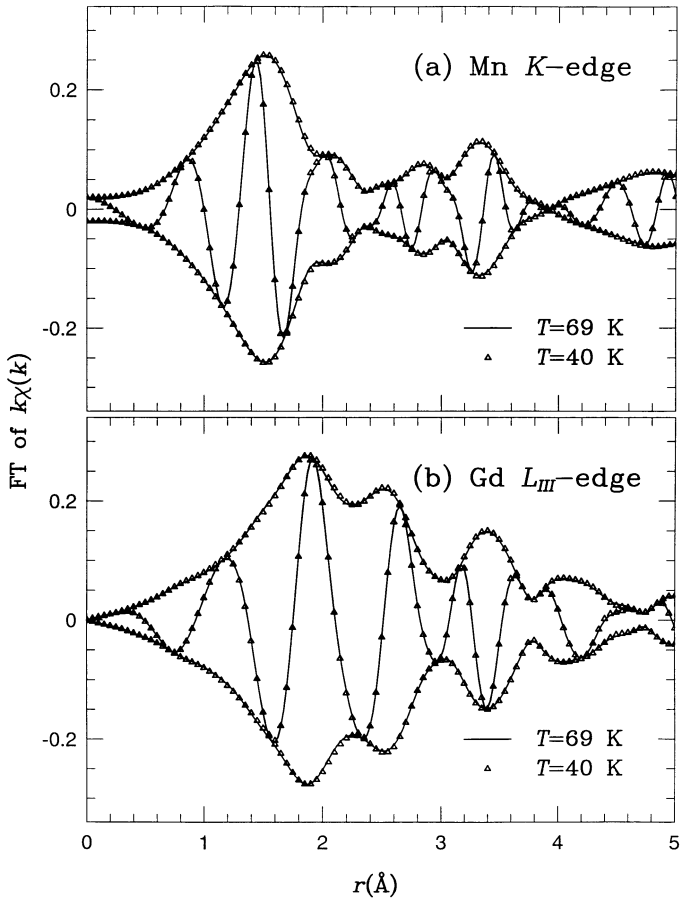

Figure 5-8 Fourier transform of $k\chi(k)$ from (a) Mn *K*-edge and (b) Gd L_{III}-edge data on $Gd_{0.67}Ca_{0.33}MnO_3$. The solid lines are data collected at T = 69 K, while the triangles (△) are data collected at T = 40 K. Agreement between data above and below T_C is well within the errors of the experiment. Transform ranges for the Gd edge data are from 3.5-12.5 $Å^{-1}$ and Gaussian broadened by 0.3 $Å^{-1}$. Transform ranges for the Mn edge data are from 3.2-12.5 $Å^{-1}$ and Gaussian broadened by 0.3 $Å^{-1}$.

The agreement between the data above and below T_C is very good and places limits on any atom-position changes around either the Gd or Mn atoms within ±0.005 Å, and changes in the Debye-Waller broadening factor to ±0.002 Å (P*nma*; a = 5.52Å, b = 7.50Å, c = 5.34Å).

5.3.1 Relationship of structure to CMR

Unlike the colossal magnetoresistance manganites, $Gd_{0.67}Ca_{0.33}MnO_3$ does not have a metal-insulator transition or a large magnetoresistance near the Curie temperature. The negative magnetoresistance is only of order 1% in large fields and is proportional to H^2 (or M^2 since it scales with χ^2) like that observed in $La_{0.67}Ca_{0.33}MnO_3$ in the paramagnetic state (section 7.2.1) [150]. Thus, $Gd_{0.67}Ca_{0.33}MnO_3$ is clearly in the class of 1/3 doped manganites which, due to the small size of Gd^{3+} [100], change from paramagnetic insulators to ferromagnetic insulators at T_C. There is much interest in finding a structural change at T_C in the giant magnetoresistive manganites, since it is predicted to have a large effect on the resistive transition [11]. There is now evidence [151-154] for a decrease in structural disorder as the GMR manganites become ferromagnetic metals. $Gd_{0.67}Ca_{0.33}MnO_3$ shows the contrapositive: there is no discontinuity in the atomic disorder for a material which does not become metallic at T_C. This has also been noted in manganites with different dopant concentrations: $La_{0.88}Ca_{0.12}MnO_3$ [151] and $La_{0.5}Ca_{0.5}MnO_3$ [154].

5.4 Conclusion

$Gd_{0.67}Ca_{0.33}MnO_3$ is ferrimagnetic with a compensation temperature of about 15K due to the interaction and ordering of the Gd^{3+} ions. The qualitative features of the magnetic properties can be accounted for with a simple two sublattice (Gd and Mn) molecular field model. The large high field susceptibility at low temperatures may indicate a canting of the magnetic sublattices. Contrary to the conclusion in [136] that there does not exist long-range magnetic order (only spin-glass magnetism) in the ferromagnetic-insulator region of the tolerance-factor phase-diagram, $Gd_{0.67}Ca_{0.33}MnO_3$ shows definite long-range order and a compensation point which can not be explained by spin-glass phenomena alone. The resistivity is consistent with small polaron conductivity over a broad temperature range, with a possible crossover to a different mechanism such as variable-range hopping at low

temperatures. There is no noticeable change in the structure, as determined by XAFS, or conductivity at the ferrimagnetic transition. Recent theoretical and experimental work conclude that structural effects at T_C are associated with the metal-insulator transition and large magnetoresistance. Since $Gd_{0.67}Ca_{0.33}MnO_3$ is in the doping regime where a metal-insulator transition and large magnetoresistance are *not* observed at T_C, this work supports that conclusion, *i. e.* that a significant structural change is associated not with the ferromagnetic transition, but the metal-insulator transition.

6. Magnetoconductivity in $La_{0.67}Ca_{0.33}MnO_3$

In this chapter, the nature of the field dependence of the resistivity in $La_{0.67}Ca_{0.33}MnO_3$ - or magnetoresistance above and below T_C is studied in more detail. For this study, sample LCM 17 (Chapter 4, Table 4-2) was used since it shows magnetic and transport properties consistent with bulk samples. Measurements at $0.9T_C$ = 237 K and $1.1T_C$ = 289 K will have considerable magnetoresistance while being clearly either in the ferromagnetic or paramagnetic state. In order to achieve maximum temperature stability, data were collected only after there was no appreciable drift in the resistivity. The major conclusions have been reproduced with other samples which like this one have high T_C's and no domain boundary magnetoresistance (section 4.2.8). The work presented in this chapter has been published in [150].

Two configurations were used: 1) magnetic field parallel to the film, which was used for longitudinal and transverse magnetoresistance analysis since there is almost no demagnetization field. Since the van der Pauw configuration is used, the longitudinal magnetoresistance has a small component due to transverse magnetoresistance and *vice versa*. 2) magnetic field perpendicular to the film, used primarily for Hall effect measurements.

6.1 Anisotropic magnetoresistance

The magnetoresistance at 289 K ($1.1T_C$) on increasing and decreasing magnetic field is displayed in Figure 6-1 for longitudinal and transverse directions. The two configurations give identical magnetoresistance.

The high field ($|H|$ > 1 kOe) magnetoresistance at $0.9T_C$ is also shown in Figure 6-1 for both increasing and decreasing fields. There is no appreciable hysteresis for $|H|$ > 200 Oe. The transverse and longitudinal magnetoresistance in high fields are nearly identical when the same current path is used. Different current paths however, give a slightly different

magnetoresistance at $0.9T_C$ indicating some magnetic/electronic inhomogeneity below T_C. All current paths have the functional form of the magnetoresistance described below, and therefore the apparent inhomogeneity does not affect the conclusions of this paper. The transverse magnetoresistance with the field perpendicular to the film is identical to the transverse magnetoresistance with the field parallel to the film with an additional demagnetization field of (1750+/-100 Oe); this was used to estimate M at 0.9 T_C.

6.2 Magnetoresistance models

In order to assess the potential of the colossal magnetoresistance in a magnetic field sensor, (such as the read head in a magnetic recording device) knowledge of the magnitude and exact field dependence of the magnetoresistance is critical, primarily in low magnetic fields, H. Experimental data generally show that for low fields the magnetoresistance is approximately quadratic in H above the Curie temperature, T_C and is more cusp like or linear below T_C [116]. There exists, however, many counter examples to this generalization [22, 25, 114] presumably due to inhomogenous samples where T_C is not so well defined [116]. The best empirical model of the resistivity ($\rho = \rho_0 e^{M/M_0}$) around T_C [114] gives a linear field dependence. Since the earliest reports [4], the magnetoresistance has been claimed or assumed to be independent of the angle between the magnetic field and the current [113].

The microscopic mechanism of the magnetoresistance can be quite complicated and still not accurately predict much of the observed magnetoresistance phenomena. Much of the theory assumes an electron band transport mechanism [55], which may not be appropriate in the case of the manganites because they are not metallic above T_C. Some microscopic models of transport in the manganites have predicted the conductivity σ or

resistivity $\rho \propto M^2$ [113, 155, 156] (which is isotropic) with limited experimental verification.

6.2.1 General Model

The difference above and below T_C as well as the relationship to the magnetization M can be shown more generally by only considering the symmetry of the resistivity tensor - with no assumptions about or even a reference to microscopic transport mechanisms. Following Landau and Lifshitz [157], the relation between the electric field **E** and the current density **J** is given by the resistivity tensor ρ: $E_i = \rho_{ik} J_k$ where the components of ρ are functions of **H** and **M**. Since **H** and **M** are vectors which are antisymmetric under time reversal, ρ must have the following symmetry: $\rho_{ik}(\mathbf{H},\mathbf{M}) = \rho_{ki}(-\mathbf{H},\mathbf{M}) = \rho_{ki}(\mathbf{H},-\mathbf{M}) = \rho_{ik}(-\mathbf{H},-\mathbf{M})$. The symmetric, s_{ik}, and antisymmetric, a_{ik}, parts of $\rho_{ik} = s_{ik} + a_{ik}$ then have the following properties: $s_{ik}(\mathbf{H},\mathbf{M}) = s_{ik}(-\mathbf{H},\mathbf{M}) = s_{ik}(\mathbf{H},-\mathbf{M})$ and $a_{ik}(\mathbf{H},\mathbf{M}) = -a_{ik}(-\mathbf{H},\mathbf{M}) = -a_{ik}(\mathbf{H},-\mathbf{M})$. Thus the components of s_{ik} are even functions of **H** and **M** while those of a_{ik} are odd functions.

The measured resistivity ρ, the diagonal component of the resistivity tensor, contains no contribution from a_{ik} and therefore must be even in **H** and **M**. Assuming the resistivity is an analytic function with respect to **H** and **M** (which themselves may not be analytic in T), the first terms in the expansion of ρ in powers of **H** and **M** is then $\rho = \rho_0 + \alpha M^2 + \beta H^2 + \gamma \mathbf{H} \cdot \mathbf{M}$. At this point, one can already expect that for $T > T_C$ (M=0) the low field magnetoresistance should be proportional to H^2 while for $T < T_C$ ($M \neq 0$) the term linear in H may be expected to dominate. Clearly a negative magnetoresistance can not obey this relation for arbitrarily large H, for the resistivity would eventually become negative; higher order terms or inverse powers of H are then required. The above argument is as valid for the conductivity tensor σ, where $J_i = \sigma_{ik} E_k$, as it is for ρ. In the case of the manganites, the magnetoconductivity

is positive and unlike the magnetoresistance may not require further expansion in H.

6.2.1.1 Magnetoconductivity model

For an isotropic conductor the longitudinal and transverse magnetoconductances (and magnetoresistances) are, in general, not equal. The general form of the relation between **J** and **E** in an isotropic conductor [157] up to terms quadratic in **H** and **M** is:

$$\begin{aligned}\mathbf{J} = {} & \sigma_0\mathbf{E} + \alpha_1 M^2\mathbf{E} + \alpha_2(\mathbf{E}\cdot\mathbf{M})\mathbf{M} + \\ & \beta_1 H^2\mathbf{E} + \beta_2(\mathbf{E}\cdot\mathbf{H})\mathbf{H} + \\ & \gamma_1(\mathbf{H}\cdot\mathbf{M})\mathbf{E} + \gamma_2(\mathbf{M}\cdot\mathbf{E})\mathbf{H} + \gamma_3(\mathbf{E}\cdot\mathbf{H})\mathbf{M} + \\ & \sigma_H\mathbf{H}\times\mathbf{E} + \sigma_A\mathbf{M}\times\mathbf{E}\end{aligned} \qquad (1)$$

If all the coefficients (except α_1) are allowed to be functions of M^2, (e.g. $\sigma_0 \rightarrow \sigma_0 + \alpha_1 M^2 + \ldots$) then (1) is a complete expansion in H up to H^2 and all powers of M.

The β_i terms provide the $M = 0$ magnetoconductance quadratic in H. When $\beta_2 = 0$, the longitudinal and transverse magnetoconductances are equal. Similarly, the α_2 term leads to magnetoconductance depending on the angle between **E** and **M** - known as anisotropic magnetoresistance 6.1. The γ_i provide magnetoconductance linear in H only when $M \neq 0$. The equation used to fit the data is formally equivalent to a circuit containing a resistor (ρ_∞) in series with the magnetoconductor (*e.g.* $\sigma(H) = \sigma_0 + \sigma_{H^2}H^2$), although the physical significance of such an equivalent circuit is not entirely clear. In any event, ρ_∞ is presumably the intrinsic spin independent resistivity found to be proportional to a constant plus a T^2 term, described in sections 4.2.1 and 7.2.2 [103].

The Hall effects are contained in the antisymmetric part of σ and ρ and therefore can be expanded in odd powers of **H** and **M**. The first two terms in the Hall resistivity is $R_H\mathbf{H}\times\mathbf{J} + R_A\mathbf{M}\times\mathbf{J}$, where R_H is the normal Hall coefficient and R_A is the anomalous Hall coefficient. Since there is no evidence to prefer the Hall conductivity of equation 1 ($\approx -R_H/H^2$) to the Hall resistivity, the Hall effect is analyzed using R_H and R_A.

It is possible that the observed magnetoconductivity could be reduced to terms involving only M^2 and $(\mathbf{E}\cdot\mathbf{M})\mathbf{M}$ since $M \approx M_0 + \chi H$ gives the same field dependence described above. This would imply a strict relationship among the various $\beta_i(T)$ and $\gamma_i(T)$ which could be determined by simultaneous measurements of M and the magnetoconductivity. The resistivity saturates in a magnetic field [113, 158] more rapidly than does the magnetization (giving M^2 behavior only at small M), indicating again that it is probably the conductivity not the resistivity which is proportional to M^2. This is discussed in more detail in chapter 7.

The reciprocal nature of the conductivity and resistivity leads to only an abstract distinction between them. Thus, the simpler, empirical description of the resistivity in terms of a magnetoconductivity may be accidental. Nevertheless, it warrants further consideration. The standard additive scattering time interpretation of the magnetoresistivity requires a more complex H dependence to describe the suppression of magnetic scattering by a magnetic field. The simplicity of the magnetoconductivity expression may signify the basis of an alternative transport interpretation. Taken literally, the magnetic field appears to open parallel channels of conduction with a simple, physical functional dependence.

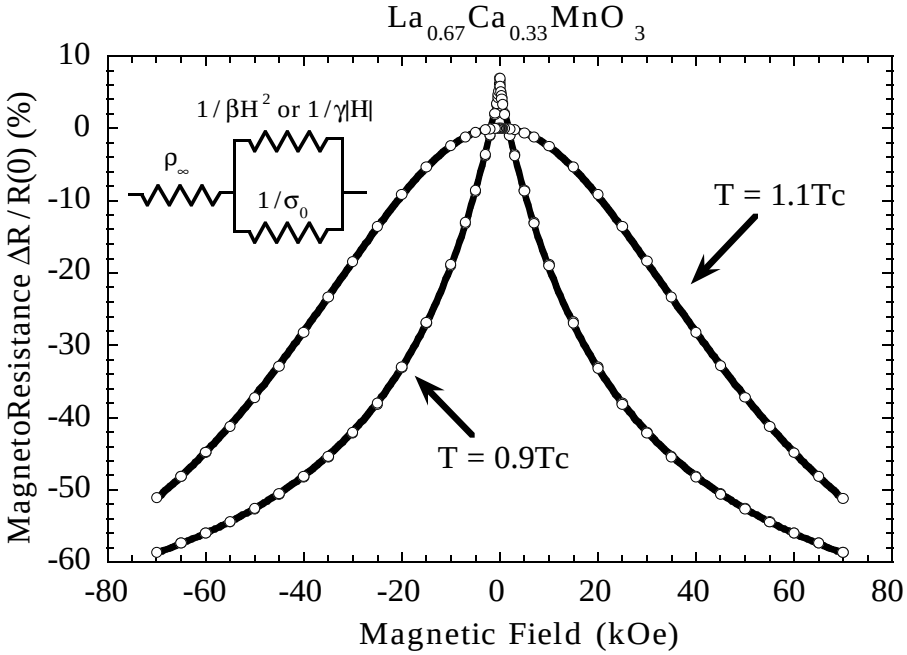

Figure 6-1 High field (longitudinal) magnetoresistance above and below T_C for $La_{0.67}Ca_{0.33}MnO_3$ film. The solid lines show the fit using the indicated equivalent circuit

6.2.1.1.1 T > T_C regime

The $1.1T_C$ data fit very well with three parameters (ρ_∞ = 1.3 mΩcm, σ_o = 0.14 $(m\Omega cm)^{-1}$ and $\sigma_{H^2} = 43 \times 10^{-6}$ $(m\Omega cm)^{-1}$ $(kOe)^{-2}$) to $\rho(H) = \rho_\infty + 1/(\sigma_0 + \beta H^2)$. A much less satisfactory fit is obtained with $\rho(H) = \rho(0) + aH^2 + bH^4$.

Above T_C, M = 0 (or at least $M = \chi H$ which gives the same field dependence of σ) so the diagonal element of the isotropic magneto-conductance tensor $\sigma(H) = \sigma_0 + \beta_1 H^2 + \beta_2(\mathbf{E}\cdot\mathbf{H})^2/E^2$. From the fit described above at 1.1 T_C, $\beta_1 = 43 \times 10^{-6}$ $(m\Omega cm)^{-1}$ $(kOe)^{-2}$ and $\beta_2 \approx 0$ is estimated.

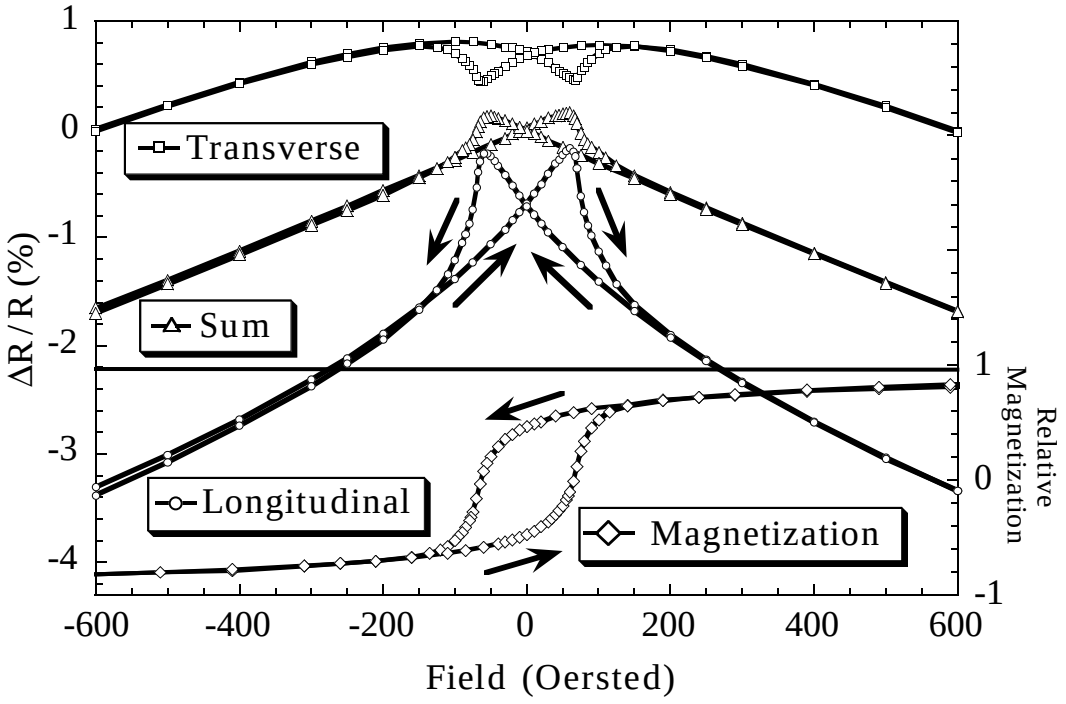

Figure 6-2 Low field magnetoresistance and magnetization (relative units) of $La_{0.67}Ca_{0.33}MnO_3$ at 0.9 T_C. The sum of the longitudinal and transverse resistances minimizes the effect of the anisotropic magnetoresistance.

6.2.1.1.2 T < T_C regime

The longitudinal data fit well with three parameters (ρ_∞ = 0.58 mΩcm, σ_o = 0.35 $(m\Omega cm)^{-1}$ and σ_H = 0.013 $(m\Omega cm\ kOe)^{-1}$) to $\rho(H) = \rho_\infty + 1/(\sigma_o + \sigma_H|H|)$. A significantly less satisfactory fit is obtained with an exponential form [114, 156]: $\rho(H) = \rho_\infty + ae^{-|H|/b}$.

Below T_C and for $\mathbf{M} \neq 0$ parallel to $\mathbf{H}$, i. e. $\mathbf{M} = M\mathbf{H}/|\mathbf{H}|$, then up to terms linear in H, $\sigma(H)$ reduces to $(\sigma_0 + \alpha_1 M^2) + \alpha_2 M^2(\mathbf{E}\cdot\mathbf{H})^2/E^2H^2 + \gamma_1 M|\mathbf{H}| + (\gamma_2 + \gamma_3)M|\mathbf{H}|(\mathbf{E}\cdot\mathbf{H})^2/E^2H^2$. By fitting the $0.9T_C$ data, $\gamma_1 = \sigma_H/M = 73 \times 10^{-6}$ (mΩcm

kOe emu)$^{-1}$ is estimated. For equal longitudinal and transverse magnetoresistance, $\gamma_2 + \gamma_3 \approx 0$.

The |**H**| form of the magnetoresistance below T_C provides a cusp in the magnetoresistance near $H = 0$. This is in contrast to the rounded curve observed above T_C.

6.2.1.1.3 Anisotropic magnetoresistance

The low field data are shown in Figure 6-2 with the average of the transverse and longitudinal magnetoresistances. The vertical offset of these data is approximate, *i.e.* it is calculated from measurements of a different, patterned sample. The switching of the resistivity at +/-65 Oe is due to the switching of the magnetization (coercivity). This can be seen in Figure 6-2 where the magnetization, relative to the saturated 0.9 T_C value of about $1\mu_B$/Mn, is shown for comparison.

The anisotropic magnetoresistance (AMR) at $0.9T_C$ appears to provide the nonlinear magnetoresistance in low fields, (Figure 6-2) aside from the magnetization switching at 65 Oe. Since $1/(\rho_{trans} + \rho_{long}) \approx \alpha_2(\mathbf{E}_{trans} \bullet \mathbf{M})^2 + \alpha_2(\mathbf{E}_{long} \bullet \mathbf{M})^2 \approx \alpha_2 M^2(\mathrm{Cos}^2(\theta) + \mathrm{Cos}^2(\theta + 90°)) = \alpha_2 M^2$, the sum of the transverse and longitudinal resistances should be independent of the direction of M, leaving only the magnetoresistance linear in H (Figure 6-2). This is approximately what happens. The larger (smaller) than linear peak (depression) in the longitudinal (transverse) magnetoresistance for $H < 100$ Oe is apparently due to AMR since the sum produces a curve which looks like |H| that switches at the coercive field. Similar AMR has been independently verified elsewhere [159].

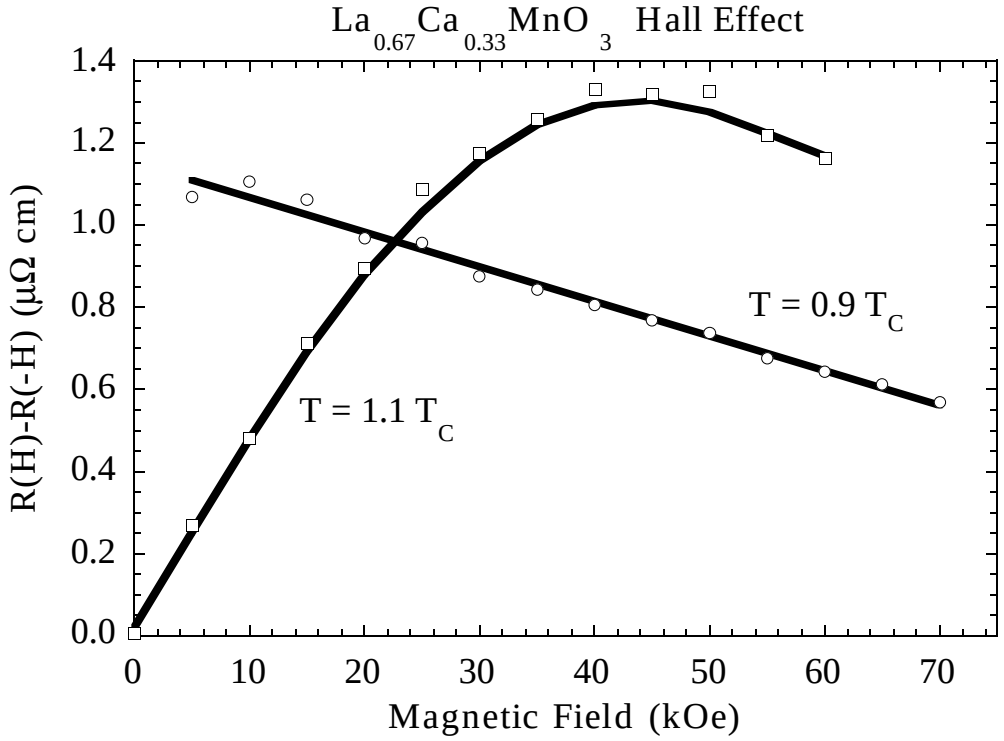

Figure 6-3 Hall effect of $La_{0.67}Ca_{0.33}MnO_3$ below (fully magnetized data only) and above T_C.

6.2.1.1.4 Hall Effect

The Hall effect (Figure 6-3) is calculated from R(H) - R(-H), which should remove all contributions to the transverse voltage due to magnetoresistance and changes in magnetic homogeneity. The Hall effect at $0.9T_C$ shows a clear contribution at H=0 due to the anomalous Hall effect [160] as well as a term linear in H. From this linear term, a carrier density of n = 0.85 holes/cell is calculated which is the same as that observed at 5 K (section 4.2.4), where no anomalous Hall effect was detected. The anomalous Hall effect apparently increases with temperature, which is quite unexpected since it is usually proportional to M [160]. Nevertheless, this has also been observed in the magnetic spinels such as $CuCr_2Se_4$ [132-134]. At 1.1 T_C the Hall effect has an

electron-like slope at low fields that slowly reverses to hole-like in high fields. The low field slope can be attributed to the anomalous Hall effect resulting from the magnetization due to the Curie-Weiss susceptibility, χ: $R_{hall} = R_A M + R_H H = (\chi R_A + R_H)H$. Thus while the sample magnetizes the Hall effect looks electron-like, but once the magnetization saturates, the Hall effect returns to hole-like.

6.3 Conclusion

In summary, an accurate and simple model, based solely on symmetry without reference to any mechanism, is proposed for the magnetoresistance in $La_{0.67}Ca_{0.33}MnO_3$. One can also conclude from this model that the mechanism of the magnetotransport is best described by a magnetoconductance, and therefore mechanistic theories should predict at least a M^2 dependence of the conductivity. The functional form and estimate of parameters presented above should not only help guide the development of a mechanistic theory, but also provide a basis for predicting the magnetotransport properties when designing a device.

In homogeneous materials, it is clear that the magnetoresistance maximizes near the ferromagnetic Curie temperature T_C and rapidly decreases at lower or higher temperatures. The magnetoresistance also slowly saturates as the magnetic field is increased past several Tesla. Thus, the conductivity behaves much like the magnetization: above T_C the conductivity and magnetization are low, while below T_C the conductivity and magnetization rapidly increase. Furthermore, near T_C both the conductivity and resistivity can be increased by an applied magnetic field. The theory of double exchange, which has been developed to explain these properties of the manganites [7, 112, 155], predicts this correlation between the conductivity and the magnetization.

7. Critical Transport and Magnetization of $La_{0.67}Ca_{0.33}MnO_3$

In homogeneous $La_{0.67}Ca_{0.33}MnO_3$, it is clear that the magnetoresistance maximizes near the ferromagnetic Curie temperature T_C and rapidly decreases at lower or higher temperatures. The magnetoresistance also slowly saturates as the magnetic field is increased past several Tesla. Thus, the conductivity behaves much like the magnetization: above T_C the conductivity and magnetization are low, while below T_C the conductivity and magnetization rapidly increase. Furthermore, near T_C both the conductivity and magnetic moment can be increased by an applied magnetic field. The theory of double exchange, which has been developed to explain these properties of the manganites [7, 112, 155], predicts this correlation between the conductivity and the magnetization.

The relationship between the conductivity (or resistivity) and the magnetization has been examined both experimentally and theoretically. Several theoretical models [31, 112, 121, 155, 156, 161-164] predict an M^2 dependence of the resistivity (or conductivity). The first term of the Taylor series expansion of the resistivity (or conductivity) in terms of M should be M^2 for all models due to symmetry considerations [150].

Experimentally, a correlation between the resistivity and magnetization can be found by plotting one as a function of the other [24, 114, 115, 121, 158, 165]. These plots show that the resistivity is roughly proportional to the square of the magnetization M^2 for small M. For larger M however, the resistance decreases more slowly in relationship to M^2 as if it were saturating before the magnetization does. Thus the relationship between the resistivity and the magnetization is more complicated than $\rho \propto M^2$. This relationship may instead be well described by an M^2 dependence of the conductivity in a slightly more complicated circuit [150]. In the previous chapter, only the

magnetic field H dependence of the resistivity is shown to be more fully described in terms of a magnetoconductive circuit, $\rho = \rho_\infty + 1/(\sigma_0 + \sigma_{H^2}H^2)$ for $T > T_C$ and $\rho = \rho_\infty + 1/(\sigma_0 + \sigma_H|H|)$ for $T < T_C$, where ρ_∞, σ_0, σ_{H^2} and σ_H are parameters. In order to determine if the magnetoconductivity, $\sigma_{H^2}H^2$ and $\sigma_H|H|$ can replaced by a common term proportional to M^2 as suggested above, the temperature dependencies and magnitudes of σ_{H^2}, σ_H and M need to be examined.

Alternatively, it has been found in several cases that the correlation $\rho \propto \exp[-M(H,T)/M_E]$ is a good fit to the data [24, 114, 115]. This formulation does not yet have a good theoretical understanding.

In this chapter, which will be published separately, the temperature and field dependence of the magnetization and magnetoresistance, above and below T_C are reported. A well annealed $La_{0.67}Ca_{0.33}MnO_3$ thin film on a $LaAlO_3$ substrate grown by MOCVD was used for transport measurements as described in chapter 4. DC conductivity measurements were performed using the method of Van der Pauw [52, 53]. Only the longitudinal magnetoresistance data are shown. The transverse magnetoresistance is nearly identical to the longitudinal as was discussed in chapter 6. After stabilizing the temperature, repeated resistance *R vs. H* curves were measured and fit with three parameters (ρ_∞, σ_0, and σ_{H^2} or σ_H) to $\rho = \rho_\infty + 1/(\sigma_0 + \sigma_{H^2}H^2)$ for $T > T_C$ and $\rho = \rho_\infty + 1/(\sigma_0 + \sigma_H|H|)$ for $T < T_C$. The data fit well to these forms except the few degrees near T_C (where a combination of the two forms is better) and at low temperatures. For $T < 50$ K the magnetoresistance shows no sign of saturating ($\rho = [\rho_\infty + 1/\sigma_0] - \sigma_H|H|/\sigma_0^2$), so only two parameters ($[\rho_\infty + 1/\sigma_0]$ and σ_H/σ_0^2) can be extracted.

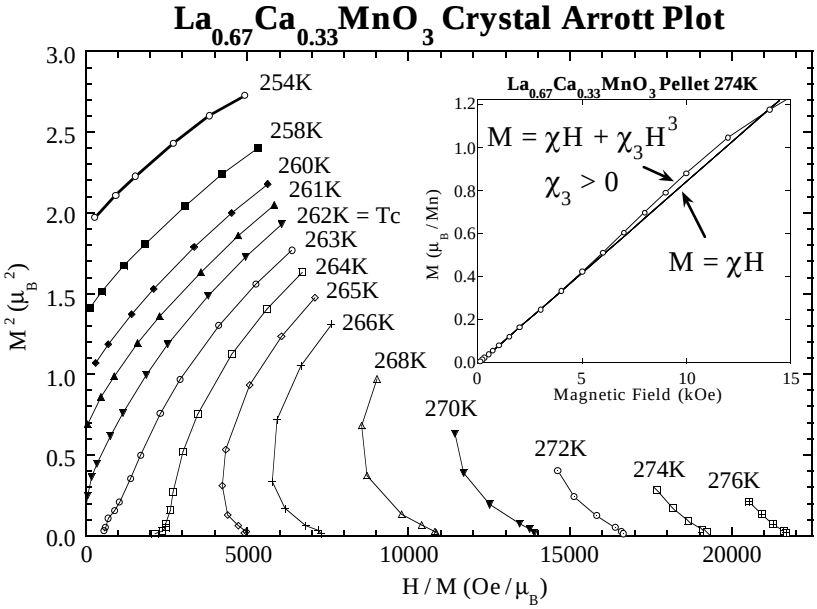

Figure 7-1. M^2 vs. H/M plot for $La_{0.67}Ca_{0.33}MnO_3$ float zone crystal. A mean field ferromagnet has linear isotherms with a positive slope. The negative slope for $T > T_C$ indicates a faster than linear increase in M (inset) due to a highly unusual positive non-linear susceptibility χ_3.

The focus of this study is on the isotropic properties. The effects due to the anisotropic magnetoresistance (section 6.1) and magnetocrystalline anisotropy are minimized by concentrating on the $H > 1000$ Oe data for $T < T_C$. Even in this preliminary investigation, peculiar magnetic properties are found that require a more complex physical model than that used for a typical ferromagnet.

7.1 Magnetism near T_C

Magnetization measurements were performed while the magnetic field H was decreasing. Data for increasing H field are identical to the H decreasing data for $T > T_C$. Polycrystalline pellets were prepared (section 2.1.1) and this material was used to for floating-zone laser-heated crystal growth described in

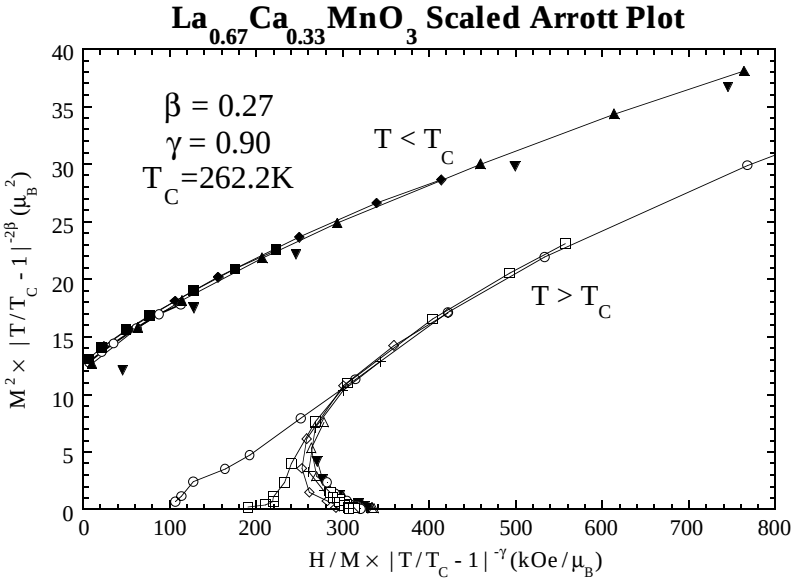

Figure 7-2. Data from Figure 7-1 (using the same symbols) scaled with β = 0.27 and γ = 0.90. According to the scaling hypothesis, all the $T < T_C$ data should lie on a single curve while the $T > T_C$ data should lie on a separate, single curve.

section 2.1.2. The float zone product (referred to below as "crystal") is dense and crystallographically highly-oriented. The polycrystalline pellets and a float zone crystal used for magnetization measurements have very similar magnetic properties. A demagnetization factor N ($H_d = 4\pi NM$) of about 0.5 was estimated and used to correct the data. The demagnetization correction is large only for H small. The conclusions of this work are unaffected by variations in N.

Most of the $M(H, T)$ data can be scaled [90] with β = 0.27 and γ = 0.90. According to the scaling hypothesis, the magnetic equation of state in the critical region depends only on the scaled variables $H/|T_C/T - 1|^{\beta+\gamma}$ and $M/|T_C/T - 1|^{\beta}$. A plot of the scaled M^2 and scaled H/M, shown in Figure 7-2, will then have only two curves: one branch for the $T < T_C$ data and another

for $T > T_C$. The regions of negative slope on the M^2 vs. H/M plot ($\chi_3 > 0$) make the scaled $T > T_C$ curve also approach $M^2 = 0$ with a negative slope. For $T - T_C < 0.01\ T_C$, the scaled data break away from this region of negative slope to giving a nearly straight curve typical of a ferromagnet. This crossover in scaling suggests that the true critical regime only begins with $|T - T_C| < 0.01\ T_C$, and that the exponents reported here, which will be quite useful in modeling the magnetization, are effective rather than true critical exponents. The true critical regime is reached when the magnetic critical fluctuations become as large as the net magnetization itself.

The experimental value of the critical exponent δ, $H = M^\delta$ when $T = T_C$, depends strongly on the demagnetization correction, and therefore not analyzed here. The scaling relation $\delta = 1 + \gamma/\beta$ can be used to estimate δ. The other critical exponents γ and β do not vary significantly when a different demagnetization correction is used.

7.1.1 Spontaneous magnetization exponent

The square of the magnetization M^2, plotted *vs.* H/M (Figure 7-1) facilitates understanding the critical behavior of $La_{0.67}Ca_{0.33}MnO_3$. The isotherm which extrapolates to $M^2 = 0$, $H/M = 0$ is the critical isotherm $T = T_C$. In this way $T_C = 262.2$ K ± 0.5 K is estimated. The uncertainty in T_C is due to the uncertainty of the demagnetization correction. The isotherms below T_C should be approximately linear and intersect $H/M = 0$ at M_0. From these $M_0(T)$ the (magnetic order parameter) critical exponent $\beta \approx 0.30$ and $T_C = 262.2$ K can be estimated by fitting $M_0(T) \propto (1 - T/T_C)^\beta$ (Figure 7-3).

The fit is not as good as this method, in the same apparatus, allows (Appendix A), perhaps due to the contributions in low fields from the magnetocrystalline anisotropy, which have been ignored. Therefore, the

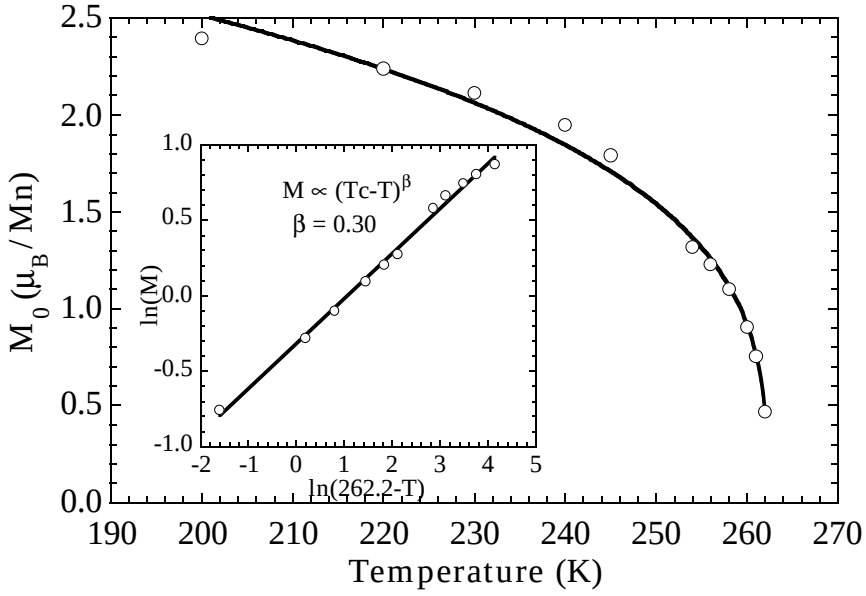

Figure 7-3. Saturation Magnetization, M_0 as a function of temperature for $La_{0.67}Ca_{0.33}MnO_3$ crystal. At each temperature, the value shown is M extrapolated to H = 0 as given by the intercept in Figure 7-1.Solid line is fit to $M_0(T) \propto (1 - T/T_C)^\beta$ with β = 0.30.

values for β reported here are more uncertain than those reported for other materials.

Typical experimental values for the critical exponent β in Fe, Ni and YIG [92] are 0.37 ± 0.02, which are near the theoretical values (Ising β = 0.33, Heisenberg β = 0.36). The related metallic ferromagnets $SrRuO_3$ (Appendix A) and $La_{0.5}Sr_{0.5}CoO_3$ [92] have β ≈ 0.36 and β = 0.361 respectively. Previous magnetic data [166, 167] on $La_{0.67}Ca_{0.33}MnO_3$ have been fit with such values of β, suggesting that the critical region has been reached. For example, muon-

spin-relaxation measurements [167] give $\beta = 0.345 \pm 0.015$ with $T_C = 274$ K. The double layer perovskite $La_{1.4}Sr_{1.6}Mn_2O_7$ has a small [168] $\beta = 0.25$ possibly due to 2-D ferromagnetism. The significance of the low values for β given here for $La_{0.67}Ca_{0.33}MnO_3$ is unknown due to the uncertainty of the measurement.

7.1.2 Susceptibility exponent

The $T > T_C$ isotherms should intersect $M^2 = 0$ at $1/\chi(T, H = 0) = 1/\chi_0 \propto (T/T_C - 1)^{\gamma}$ and can be used to give an effective $\gamma \approx 0.7$ and $T_C = 263$ K $\pm$ 1 K. This value of γ is unexpected particularly since it is less than one (Figure 7-4). For a typical ferromagnet, the plot of $1/\chi$ vs. T is close to linear at high temperatures and then become slightly concave up as T approaches T_C. In this way, the high temperature, linear extrapolation of $1/\chi$ to $1/\chi = 0$ gives the paramagnetic Curie temperature, $\Theta_P \approx 257$ K. The ferromagnetic Curie temperature, T_C is the temperature where $1/\chi$ and M_0 vanish, and normally $T_C < \Theta_P$. However, for $\gamma < 1$, the plot of $1/\chi$ *vs.* T is concave down and $\Theta_P < T_C$.

When critical fluctuations are included in the theory, γ increases due to the suppression of the transition (Ising $\gamma = 1.24$, Heisenberg $\gamma = 1.39$). Typical experimental values for γ (Fe, Ni and YIG [92] $\gamma = 1.2 \pm 0.2$; $SrRuO_3$ (Appendix A) $\gamma = 1.17$) are greater than one.

An inhomogeneous ferromagnet, with a range of T_C's, can provide such a negative curvature resulting in an apparent $\gamma < 1$; however, this will also make M_0 decrease more linearly ($\beta \approx 1$) as T approaches T_C from below. Since the observed β is not larger but smaller than expected, a range of T_C's is unlikely. In ferrimagnets such a negative curvature is expected due to the

competition between ferromagnetic and antiferromagnetic interactions. As pointed out by DeGennes, there is competition between double exchange (ferromagnetic) and superexchange (antiferromagnetic) as will be discussed further in section 7.1.4. One of the early theories of double exchange presented by Anderson and Hasagawa [7] also predicts a downward curvature in $1/\chi$ *vs.* T.

It is not too surprising that two different values of γ (0.7 and 0.9) are obtained from the same data. The two methods weight the data differently and as discussed above, the true critical region where γ is a constant has probably not been reached.

7.1.3 Positive nonlinear susceptibility

A peculiarity of the $T > T_C$ isotherms of Figure 7-1, which likely affects the determination of γ, is their negative slope as they approach $M^2 = 0$. This slope is proportional to the nonlinear susceptibility. For $M = \chi H + \chi_3 H^3$, χ is the linear susceptibility and χ_3 is the third-order nonlinear magnetic susceptibility. The slope of a $T > T_C$ isotherm in an M^2 vs. H/M Arrott plot as M^2 approaches zero is given by $-\chi^4/\chi_3$. For a normal ferromagnet, $\chi > 0$ while $\chi_3 < 0$ giving a positive slope for all $T > T_C$ isotherms. However in $La_{0.67}Ca_{0.33}MnO_3$ a negative slope is found which implies that $\chi_3 > 0$. This can also be seen in a plot of M *vs.* H, which is shown in Figure 7-1. A positive χ_3 produces the faster than linear increase in M with H which leads to an inflection point in the M *vs.* H curve due to the saturation of M for large H. This effect is not likely due to the sample preparation since it is seen in both the polycrystal and float-zone crystal samples. Arrott plots of $SrRuO_3$ (Appendix A) at similar temperatures do not show $\chi_3 > 0$, which indicates that the effect is not due to the measurement system. A more pronounced

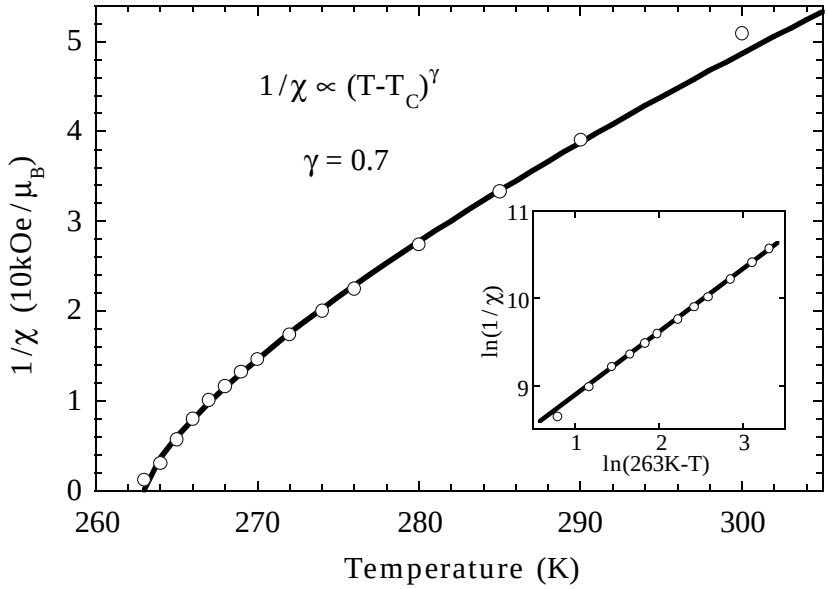

Figure 7-4. Inverse magnetic susceptibility, $1/\chi_0$ as a function of temperature for $La_{0.67}Ca_{0.33}MnO_3$ crystal. At each temperature, the value shown is H/M extrapolated to $H = 0$ as given by the intercept in Figure 7-1. Solid line is fit to $1/\chi_0 \propto (T/T_C - 1)^\gamma$ with $\gamma = 0.7$ and $T_C = 263K$.

inflection point has been observed in the double layer perovskite manganite $La_{1.4}Sr_{1.6}Mn_2O_7$ above T_C [169].

A positive χ_3 can be observed in a ferromagnet or spin glass during irreversible magnetization processes; for example, while increasing the magnetic field from a demagnetized state. However, once the material is magnetized at a high field, the curve of M vs. H for decreasing field almost always has a negative χ_3. The data in the inset of Figure 7-1 includes data for both increasing and decreasing fields, showing no signs of hysteresis [170].

Thus a positive χ_3 due to the irreversibility of a spin glass seems highly unlikely. More plausible explanations will be discussed in section 7.1.4.

7.1.4 Additional magnetic interaction

The unusual $\gamma < 1$ may be related to $\chi_3 > 0$. Both effects suggest an additional mechanism. There could, for instance, be additional magnetic interactions, such as an antiferromagnetic component to the coupling. A canted-antiferromagnet ground-state is expected theoretically from the double-exchange mechanism in conjunction with super-exchange [8], and has been found by neutron diffraction [139, 143] in the related compound $Pr_{0.67}Ca_{0.33}MnO_3$. If there is a competition between antiferromagnetic and ferromagnetic fluctuations in the paramagnetic state, the application of a magnetic field will favor ferromagnetism and thus induce a larger magnetic moment. This would explain the observed positive χ_3. The corresponding transition in the ordered state is called a metamagnetic transition. Competing magnetic interactions can also cause the downward curvature in $1/\chi$ *vs.* T seen in Figure 7-4. This is commonly observed in a ferrimagnet (*e.g.* $Gd_{0.67}Ca_{0.33}MnO_3$ described in section 5.1.2) where some strong interactions are antiferromagnetic, but near T_C a ferromagnetic susceptibility is observed. The canting of the moments by as much as 45° would still give 92% of the expected net moment, which is about that observed (section 4.1) at low temperatures for $La_{0.67}Ca_{0.33}MnO_3$.

A different but more general explanation for the unusual magnetic behavior observed in $La_{0.67}Ca_{0.33}MnO_3$ requires some additional mechanism which provides the stronger than mean field behavior, *i.e.* the ferromagnetic interaction strength appears to increase, beyond that predicted by the mean field approximation, as the magnetization increases. For instance, as T approaches T_C, the strength of the interaction increases, effectively increasing T_C. This causes the susceptibility to diverge faster than expected, providing

$\gamma < 1$. Also, at a constant $T > T_C$, as H is applied M increases, which induces stronger coupling (higher effective T_C) and therefore increasing the susceptibility in a nonlinear way: $\chi_3 > 0$.

This additional mechanism may be related to the ferromagnetic metal to paramagnetic insulator phase transition. $La_{0.67}Ca_{0.33}MnO_3$, like other materials which exhibit a metal-insulator phase transition, undergoes a static and even dynamic structural transition [151, 154, 171, 172]. The changes in the electronic and atomic structure should alter the magnetic coupling, *i.e.* the exchange J is not a constant, but a function of M or ρ. Specifically, since the metallic state has a lower volume than the insulating state, one might expect the magnetic coupling to strengthen as the material becomes more metallic.

The metallic character, conversely, is clearly associated with the magnetism as is predicted in the double exchange model. As the applied magnetic field (and hence the magnetization) increases, the material becomes more metallic. Not only does the resistivity decrease, but the metal-insulator transition (defined by a change in sign of $d\rho/dT$) is pushed to higher temperatures. If the induced metallic state promotes a further increase in the magnetization, a positive nonlinear susceptibility ($\chi_3 > 0$) and a rapidly diverging susceptibility ($\gamma < 1$) may be generated. Thus, the structural change may cause the magnetism to increase faster than that expected from the mean field model.

$La_{0.67}Ca_{0.33}MnO_3$ may have a smaller critical region than a normal ferromagnet because of these additional interactions. In typical ferromagnets, short range exchange interactions result in a short coherence length of the magnetic fluctuations. These fluctuations have low energy and can be observed relatively far from T_C. In $La_{0.67}Ca_{0.33}MnO_3$ additional electronic and lattice interactions may increase the fluctuation coherence length. With

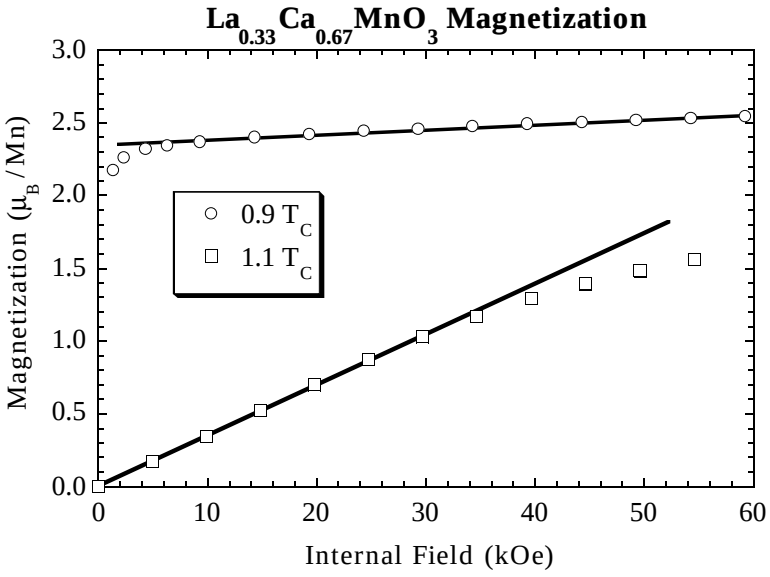

Figure 7-5. Magnetization in a magnetic field for a $La_{0.67}Ca_{0.33}MnO_3$ polycrystalline pellet at 0.9 and 1.1 T_C. The solid lines indicate the linear regions in each case.

more volume involved for each fluctuation, they will have higher energy and only observable very near T_C.

7.2 Magnetoresistance

To illustrate the need for the magnetoconductivity expression described in section 6.2.1.1 for the magnetoresistance, the two temperatures 0.9 T_C and 1.1T_C are considered first. The magnetization of a polycrystalline pellet at these two temperatures is shown in Figure 7-5. At T = 0.9 T_C, $M \approx M_0 + \chi H$ except in fields less than a few kOe when the material is not yet magnetically saturated. At T = 1.1 T_C, $M \approx \chi H$ is a good approximation particularly for H < 40 kOe. The films used in this study have been shown to have similar magnetic behavior as the bulk samples (chapter 4), but due to their small volume and the complication of the substrate provide less accurate magnetic

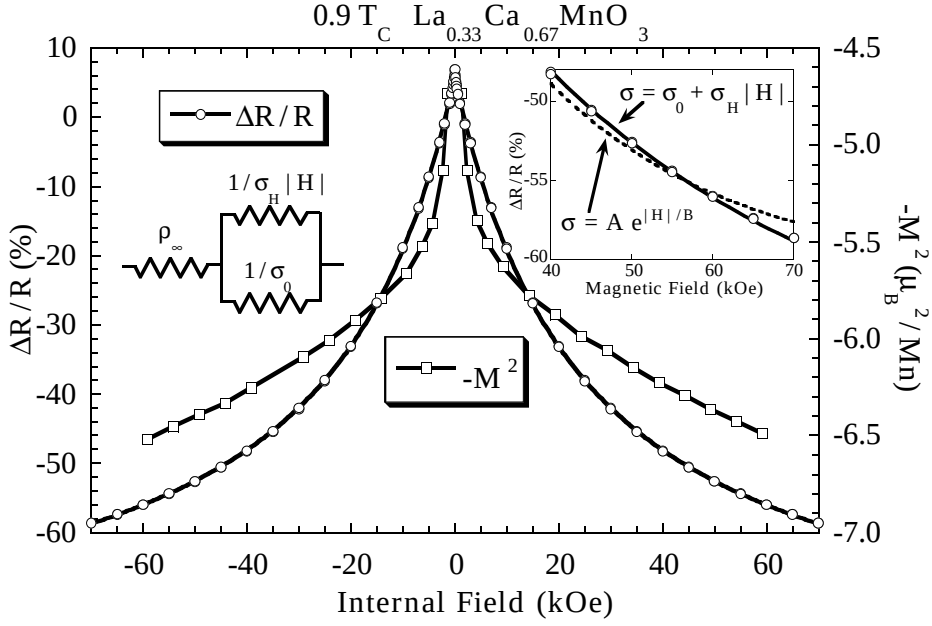

Figure 7-6. Magnetoresistance of $La_{0.67}Ca_{0.33}MnO_3$ film compared with $-M^2$ of a pellet, both at 0.9 T_C. The solid line for the magnetoresistance data shows the fit using the indicated equivalent circuit. The dashed line in the inset compares the exponential fit.

data. Therefore, in what follows, the magnetotransport on films is compared with magnetization measured on bulk (ceramic and crystal) samples.

The magnetoresistance, $\Delta R/R$, and M^2 as functions of internal field (making the demagnetization correction described above) are compared below and above T_C in Figure 7-6 and Figure 7-7. They are clearly related qualitatively, although there are marked differences at high fields as saturation is approached, particularly for $T < T_C$.

The saturation of the magnetoresistance is best described by the fit to a magnetoconductivity circuit (section 6.2.1.1), as if the magnetic field were opening channels of conductivity. This circuit assumes a linear *M vs. H*

(section 6.2.1.1). The resistivity is fit to $\rho = \rho_\infty + 1/\sigma$ where $\sigma = \sigma_0 + \sigma_{H^2}H^2$ for $T > T_C$, while for $T < T_C$, $\sigma = \sigma_0 + \sigma_H|H|$ is used. Each fit has three free parameters ρ_∞, σ_0, and σ_{H^2} or σ_H. If the magnetoconductivity is indeed proportional to M^2 as suggested above, then the nonlinearity of M *vs*. H (Figure 7-5) will slightly alter the fitting parameters, particularly ρ_∞.

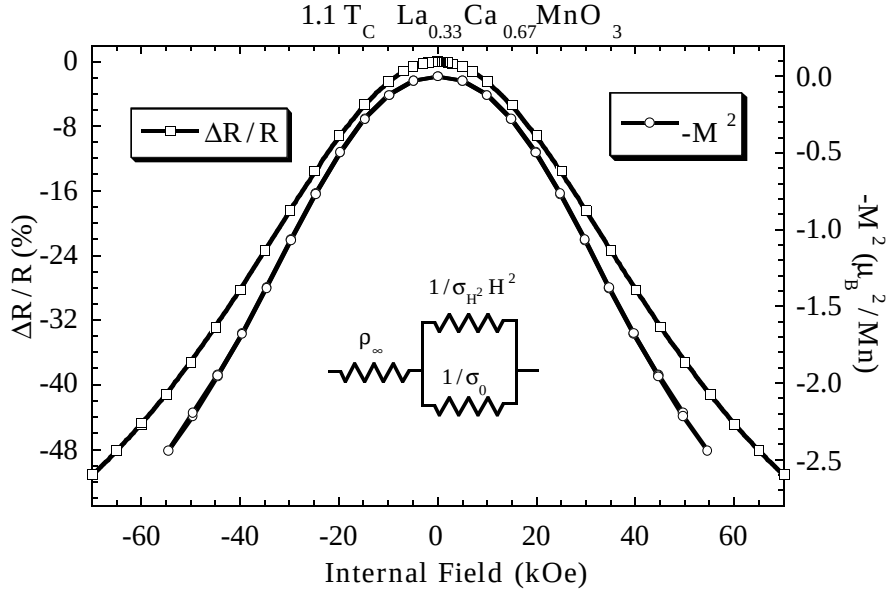

Figure 7-7. Magnetoresistance of $La_{0.67}Ca_{0.33}MnO_3$ film compared with $-M^2$ of a pellet, both at 1.1 T_C. The solid line for the magnetoresistance data shows the fit using the indicated equivalent circuit.

The exponential dependence of the resistivity first proposed by Hundley *et al*. [114] on the magnetization $\rho = \rho_E \exp[-M(H,T)/M_E]$ does not fit the magnetoresistance data as well above T_C as the fit described above. For $T > T_C$ and H small, $\rho \approx \rho_E \exp[-\chi H/M_E] \approx \rho_E(1 - \chi H/M_E)$ predicts a magnetoresistance linear in H while the observed magnetoresistance is quadratic (Figure 7-7). Below T_C the exponential fit is not at good as the magnetoconductivity circuit

(Figure 7-6), in so far as the *H* dependence is concerned; however, the exponential dependence upon *M* is found, as will be shown below.

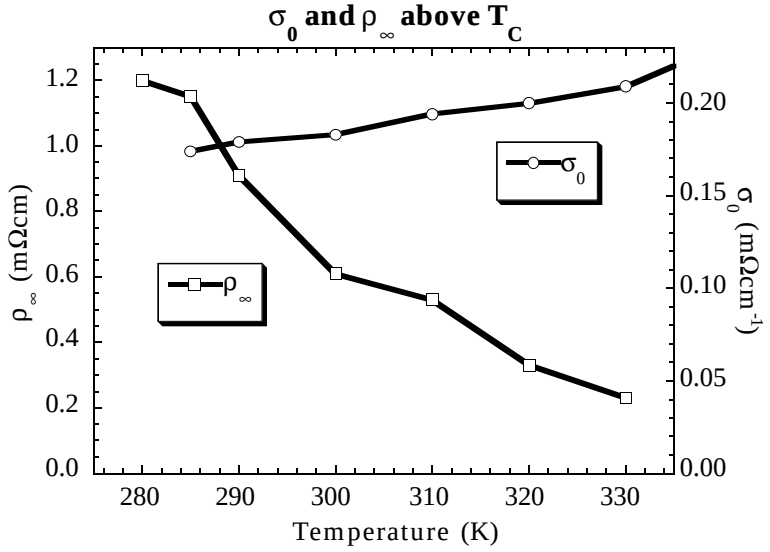

Figure 7-8. Fitting parameters σ_0 and ρ_∞ for $T > T_C$ in a $La_{0.67}Ca_{0.33}MnO_3$ film. The temperature dependence of these two parameters reflect the insulating behavior of the material.

7.2.1 Magnetoresistance scaling above T_C

The magnetoresistance data at various temperatures above T_C were fit to the expression $\rho = \rho_\infty + 1/(\sigma_0 + \sigma_{H^2}H^2)$. The resulting parameters σ_0 and ρ_∞ are shown in Figure 7-8. The parameter σ_0 remains relatively constant, slightly increasing as expected for a semiconductor. The significance of ρ_∞ will be discussed below.

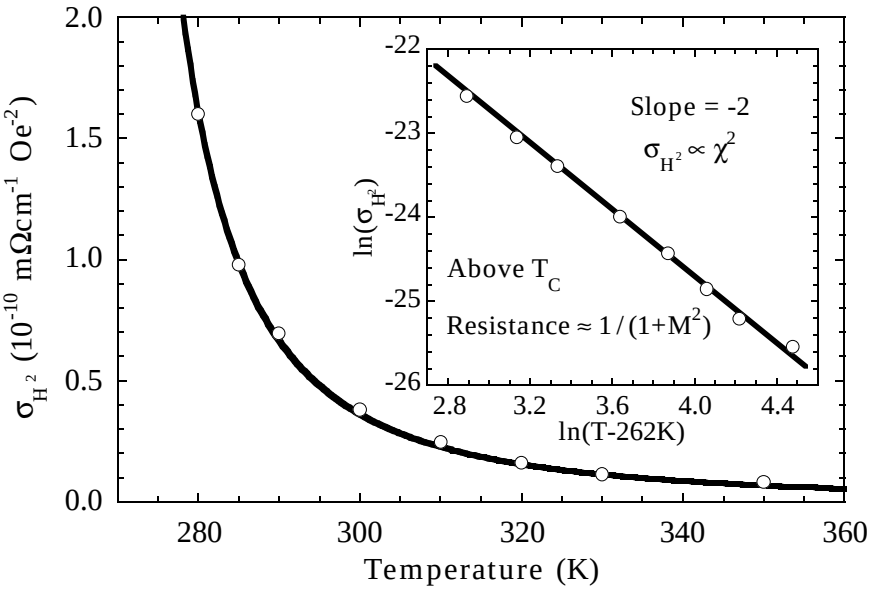

Figure 7-9. Fitting parameter σ_{H^2} as a function of temperature in a $La_{0.67}Ca_{0.33}MnO_3$ film for $T > T_C$. The temperature dependence of σ_{H^2} and the square of the susceptibility are the same, indicating a relationship between the magnetoconductance and M^2.

The parameter σ_{H^2}, which determines the magnetoresistance, is highly temperature dependent (Figure 7-9), diverging at T_C. The data can be fit with a critical exponent of -2.0 ± 0.1: $\sigma_{H^2}(T) = \sigma_{H^2}(2T_C)\,(T/T_C - 1)^{-2}$, where T_C = 262 K ± 1 K and $\sigma_{H^2}(2T_C) \approx 8 \times 10^{-13}$ Oe^{-2} mΩcm^{-1}. This result supports an M^2 dependence of the magnetoconductance (or magnetoresistance) since $M^2 \propto (T/T_C - 1)^{-2\gamma}$ above T_C, where, as experimentally determined above, $\gamma \approx 0.9$. Specifically, it is found that $\sigma(H,T) = \sigma_0 + \sigma_{H^2}(T)H^2 \approx \sigma_0 + \sigma_{M^2}M^2$. Using the Curie Weiss susceptibility from [103], $M = \chi H \approx 5 \times 10^{-4}$ (emu G^{-1} cm^{-3}) $\times$ $(T/T_C - 1)^{-1} H$, gives $\sigma_{M^2} = 3 \times 10^{-6}$ Oe^{-2} mΩcm^{-1}.

The related form $\rho \propto -M^2$ would also be consistent with our low field data since in low fields $\Delta\rho = -H^2 \sigma_{H^2}/\sigma_0^2$ and σ_0 is nearly constant with respect to temperature. This form was also observed above T_C in $La_{1-x}Sr_xCoO_3$ [165] and in small fields for lower T_C films [158] of $La_{0.7}Ca_{0.3}MnO_3$. In the temperature range of this experiment, $T > 1.01\ T_C$, $4\pi M < H$, so $B = H + 4\pi M \approx H$ and therefore not very temperature dependent. Thus the resistivity or conductivity is not proportional to B or B^2.

7.2.2 Magnetoresistance scaling below T_C

Below T_C, ρ_∞ can be interpreted as due to scattering processes which would persist if the moments were perfectly ordered. As shown in Figure 7-10, the resistivity in a infinite field, ρ_∞, follows the $A + BT^2$ fit to the low-temperature, $H = 0$, intrinsic resistivity described in section 4.2.1. In a true infinite field ($H = \infty$) one would expect the resistance to be continuous with a positive (metallic) slope as T increases through T_C. While there is a factor of 2 discrepancy between $\rho_\infty(T_C)$ extrapolated from above (Figure 7-8) and below (Figure 7-10) this is not unreasonable because two different fitting equations are used. Particularly above T_C, the fitting parameter ρ_∞ may not reflect the true $H = \infty$ resistivity because the nonlinearity of M upon H is not taken into account.

The parameter σ_0, which can be related to the resistivity in zero field $\rho(H = 0) \approx \rho_\infty + 1/\sigma_0$, describes the limiting field-dependent, spin-disorder scattering processes present as H approaches 0. Unlike ρ_∞, $1/\sigma_0$ diverges as the Curie temperature is approached. A critical exponent of about 1.8 (Figure 7-10) is found: $\sigma_0(T) \approx \sigma_0(0)\,(1 - T/T_C)^{1.8}$, where $\sigma_0(0) \approx 2 \times 10^{-3}$ mΩcm^{-1}.

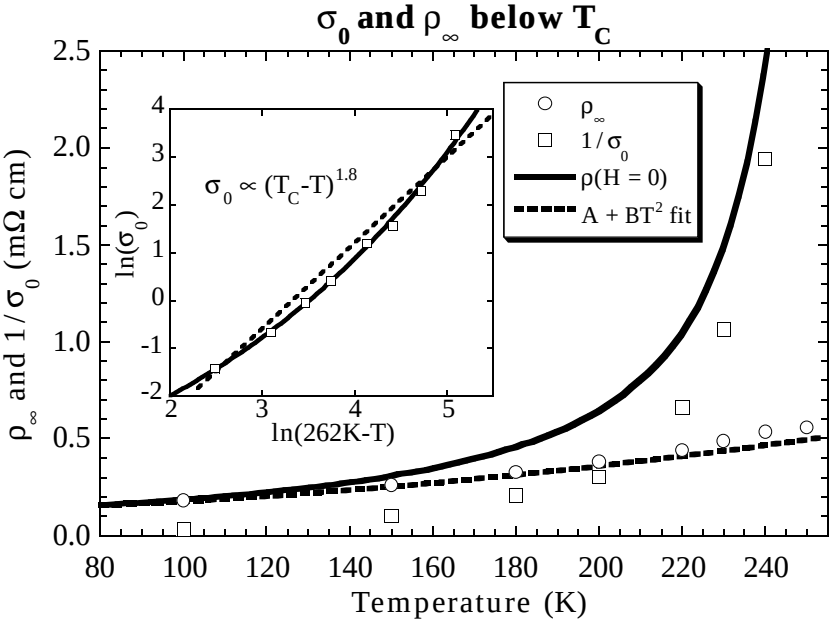

Figure 7-10. Fitting parameters σ_0 and ρ_∞ for $T < T_C$ in a $La_{0.67}Ca_{0.33}MnO_3$ film. ρ_∞ is governed by the $A + BT^2$ terms in the resistivity while σ_0 diverges at T_C. The inset shows σ_0 data fit with a $(T_C - T)^{1.8}$ power law (dashed line), and $\sigma \propto \exp(M/M_E)$ (solid line). The zero field resistivity $\rho(H = 0) = \rho_\infty + 1/\sigma_0$ is shown for comparison.

The parameter σ_H is more difficult to interpret than the other parameters. Although the magnetoresistance, $\Delta R/HR$ proportional to σ_H/σ_0^2, increases as T_C is approached, σ_H decreases. Thus the large magnetoresistance found below T_C is due to the divergence of $1/\sigma_0$ and not σ_H. The parameter σ_H does not always appear to vanish completely as T approaches T_C, making it difficult to fit to a $(1 - T/T_C)^n$ power law. Assuming T_C = 262K (determined from the critical properties of σ_{H^2} and σ_0) the exponent for σ_H is about 0.7.

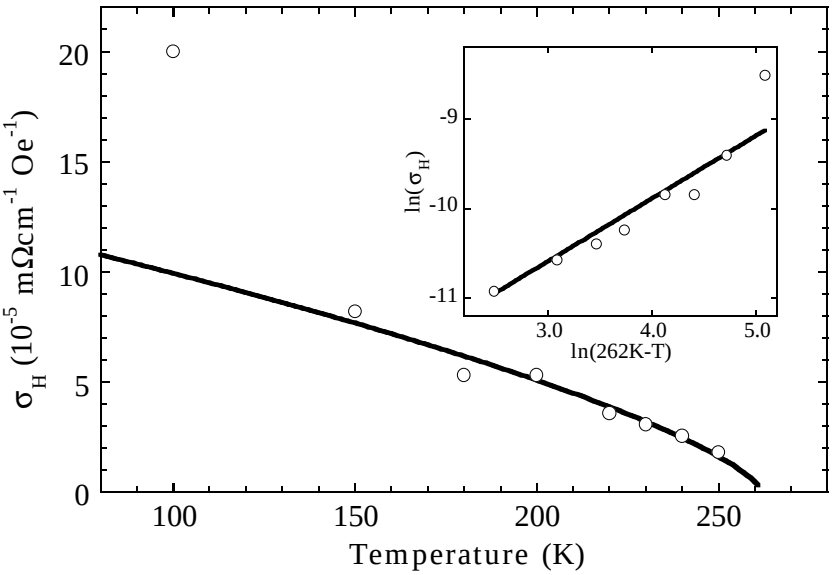

Figure 7-11. Fitting parameter σ_H as a function of temperature in a $La_{0.67}Ca_{0.33}MnO_3$ film for $T < T_C$. The solid line shows the best fit to the data using a critical exponent of 0.7.

There is no simple relationship between either the magnetoconductance or the magnetoresistance with M^2 below T_C because the measured scaling exponents do not agree with those predicted from an M^2 dependence as discussed in the following. Shown in Figure 7-5 is the magnetization below T_C which can be approximated with $M(H) = M_0 + \chi H$, and therefore $M^2 \approx M_0^2 + 2\chi M_0 H$. Assuming $\sigma(H,T) = \sigma_0 + \sigma_H H \approx \sigma_{M^2} M(H,T)^2$ as suggested above, then below T_C the following relations should hold: $\sigma_0 = \sigma_{M^2} M_0^2$ and $\sigma_H = 2\chi\sigma_{M^2} M_0$. The temperature dependence of M_0 and χ below T_C should be governed by the scaling exponents β and γ, via $M_0 \propto (1 - T/T_C)^{\beta}$ and $\chi \propto (1 - T/T_C)^{-\gamma}$ where experimentally $\beta = 0.3$ and $\gamma \approx 0.9$ (typical critical exponents are $\beta \approx 0.35$ and $\gamma \approx 1.2$). Thus one would expect the critical

exponent for σ_0 and σ_H to be 0.6 and -0.6 respectively. Experimentally, however $\sigma_0 \propto (1 - T/T_C)^{1.8}$ and $\sigma_H \propto (1 - T/T_C)^{0.7}$.

An M^2 dependence of the magnetoresistance (as opposed to the magnetoconductance) where $\rho \approx \rho_0 - \rho_M M^2 \approx (\rho_0 - \rho_M M_0^2) - 2\rho_M \chi M_0 H$ below T_C, is also inconsistent. For low fields $\rho = (\rho_\infty + 1/\sigma_0) - (\sigma_H/\sigma_0^2)|H|$ is found experimentally, which has a field dependent term (σ_H/σ_0^2), which varies as $(1 - T/T_C)^{-2.9}$. This is quite different from $2\rho_M \chi M_0$ which has a critical exponent of $\beta - \gamma \approx -0.6$.

Below T_C, in agreement with previous work [23, 107], the conductivity is exponentially dependent upon M. Removing the slowly varying contribution due to ρ_∞, this model predicts $\sigma(H,T) = \sigma_E \exp[M(H,T)/M_E] \approx \sigma_0 + \sigma_H H$. For $H = 0$ this reduces to $\sigma_0 = \sigma_E \exp[M_0(T)/M_E]$. The experimental relationship $M_0(T) \propto (1 - T/T_C)^\beta$ with $\beta = 0.3$ can be used to fit the magneto-resistance data. The higher quality of this fit compared to the M^2 fit is shown in Figure 7-10, with $M_E \approx 0.4\ \mu_B$ ($M_E = 1.0\ \mu_B$ in [107]) and $\sigma_E \approx 4 \times 10^{-3}$ mΩcm^{-1}.

An exponential dependence of the conductivity may suggest a tunneling mechanism is responsible. Tunneling conductivity depends exponentially on the length of the tunneling barrier. If, in some way, this barrier is decreased by an increase in the magnetization, then the conductivity will depend exponentially on M as observed for large M. Spin dependent tunneling is reported to be the mechanism of the large domain boundary magnetoresistance observed in these materials [140].

Furthermore, the temperature dependence of σ_H can also be explained with the exponential model. According to this model, the field dependent conductivity $\sigma_H = \frac{d}{dH}\sigma = \frac{d}{dH}\sigma_E e^{M/M_E} = \frac{\sigma_E \sigma_0}{M_E}\frac{dM}{dH} = \frac{\sigma_E}{M_E}\sigma_0 \chi$ (where

$\sigma_E \exp[M_0(T)/M_E] \approx \sigma_0$ is used) should have the same temperature dependence as $\sigma_0\chi$. Experimentally, $\sigma_0\chi$ has an approximate temperature dependence of $(1 - T/T_C)^{1.8\text{-}0.9}$, assuming γ' (susceptibility exponent for $T < T_C$) = γ. This is within experimental error of the critical exponent found (Figure 7-11) for σ_H (about 0.7).

7.2.3 Magnetoresistance scaling at T_C

At or very near T_C, the magnetic properties should be described by the critical exponent δ, where $M \propto H^{1/\delta}$ when $T = T_C$. The magnetoresistance data for T = 262 K $\approx T_C$ is shown in Figure 7-12, and can be fit to $\rho = \rho_\infty + 1/(\sigma_0 + \sigma_{H^n} H^n)$, where n is an additional free parameter. The data fit well with $n = 1.2 \pm 0.1$, where the variation of n arises from different ranges and weighting of the fit. Thus, if at T_C, the conductivity $\sigma \propto M^2$ then $\sigma \propto H^{2/\delta}$, or $\delta = 2/n$. This is clearly not the case since $2/n \approx 1.6$ while typically $\delta \approx 4.8$, or from the data presented above and the scaling relation $\delta = 1 + \gamma/\beta$ the value $\delta \approx 4.3$ is found.

The T = 262 K data fit well to the composite relation proposed by Sun *et al.* [23] $\sigma \propto M^2 \exp[M/M_E]$ combined with $H = M^\delta$. Above T_C this relation reduces to $\sigma \propto M^2$, which, as was shown above, is quite accurate. Below T_C, the exponential term dominates invalidating the simple $\sigma \propto M^2$ relationship.

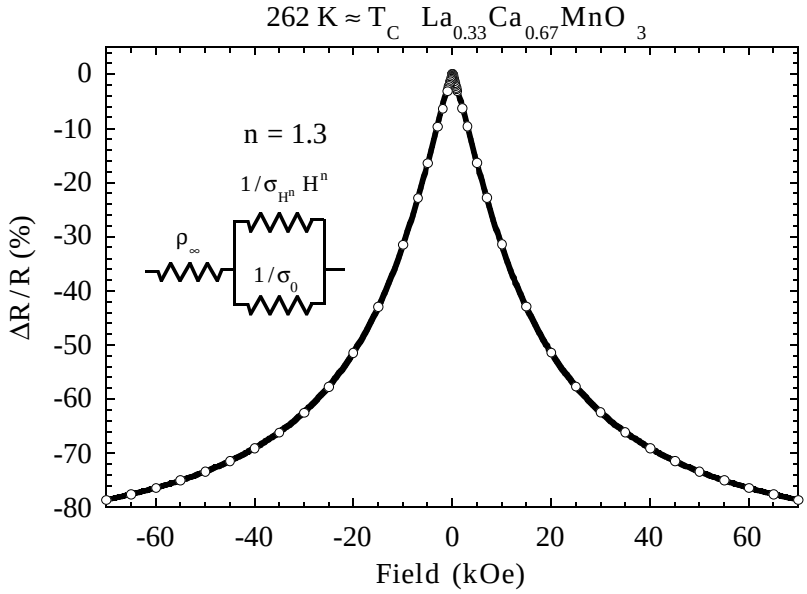

Figure 7-12. Magnetoresistance of $La_{0.67}Ca_{0.33}MnO_3$ film at 262 K ≈ T_C. The solid line shows the fit (for the full data on a linear scale) using the indicated equivalent circuit.

7.2.4 Relation to low temperature magnetoresistance

This qualitative correlation between the magnetization and the resistivity may also account for the intrinsic, small, linear magnetoresistance (Figure 4-8) found even at the lowest temperatures where the magnetization is nearly saturated. If at these low temperatures $\sigma = \sigma_0 + \sigma_{M^2}M^2$ then $\Delta\sigma/\sigma$ (or $\Delta\rho/\rho$) is given by $\Delta\sigma = 2\chi\sigma_{M^2}M_0H$. Since $\Delta\sigma = -\Delta\rho/\rho^2$, the susceptibility χ required to give the observed magnetoresistance is $\chi = -\Delta\rho/(2\rho^2\sigma_{M^2}M_0H) = 2.5 \times 10^{-4}$ emu/Oe cm^3 using the results from chapter 4 for $\Delta\rho/H = -1.5 \times 10^{-8}$ mΩcm/Oe, $\rho = 0.125$ mΩcm, and $M_0 = 3.4\ \mu_B$/Mn = 550 emu/cm^3. This is within a factor of three of the observed value (section 4.2.9, Figure 4-8) $\chi = 9 \times 10^{-5}$ emu/Oe cm^3. Similarly acceptable, is the exponential model

$\sigma = \sigma_E \exp[M(H,T)/M_E]$, which gives at low T and H, $\Delta\rho/H = -\chi\exp[-M_0/M_E]/M_E\sigma_E$; requiring $\chi = 32.9 \times 10^{-5}$ emu/Oe cm^3. A magnetoresistive model $\rho = (\rho_\infty + 1/\sigma_0) - (\sigma_{M^2}/\sigma_0^2)M^2$ giving $\Delta\rho = -2\chi\sigma_{M^2}M_0H/\sigma_0^2$ is significantly worse since it would predict $\chi = -\Delta\rho\sigma_0^2/(2\sigma_{M^2}M_0H) = 2 \times 10^{-7}$ emu/Oe cm^3.

In a similar manner, the correlation between the magnetization and the resistivity should contribute to the T^2 contribution (section 4.2.1.2) to the low temperature resistivity $\rho = R_0 + R_2T^2 + \ldots$. This is because the magnetization can be approximated with $M = M_0(1 - (T/\Theta)^2)$ for these temperatures (where $\Theta \approx 500$ K, section 4.1.1), giving $\rho(T) \propto -M(T) \propto T^2$. For the $\sigma = \sigma_0 + \sigma_{M^2}M^2$ model $\rho(T) - \rho(0) = -\rho^2(\sigma(T) - \sigma(0)) = 2\sigma_{M^2}\rho^2M_0^2(T/\Theta)^2 \approx 1.26 \times 10^{-7}$ mΩcm K^{-2} T^2. For the $\rho = \exp[-M(H,T)/M_E]/\sigma_E$ model $\rho(T) - \rho(0) = \exp[-M_0/M_E]/\sigma_E \times (T/\Theta)^2M_0/M_E \approx 1.14 \times 10^{-6}$ mΩcm K^{-2} T^2. Both of these proposed contributions are less than the observed value (section 4.2.1.2) $R_2 \approx 1.96 \times 10^{-5}$ mΩcm K^{-2}, suggesting that scattering mechanisms such as electron-electron, or electron-magnon scattering dominates the R_2T^2 term.

7.3 Conclusion

A scaling relation has been found that satisfactorily characterizes the magnetic and magnetoresistive properties of $La_{0.67}Ca_{0.33}MnO_3$ near T_C. However the scaling exponents, particularly $\gamma < 1$, show that critical scaling has not been reached even though the measurements reach 0.01 T/T_C where simple ferromagnets are expected to exhibit critical scaling.

An unusual positive nonlinear magnetic susceptibility, which does not disrupt the scaling, is also observed. The positive non-linear susceptibility and susceptibility exponent $\gamma < 1$ may result from the coupling of the

ferromagnetic and metal-insulator transitions, making the exchange J a function of M.

The scaling of both the H and T dependence of the magnetoconductance above T_C is consistent with a simple M^2 dependence of the conductivity. However, below or very near T_C this correlation predicts the observed H dependence but can not account for the T dependence. To fit these data, the model for the magnetoresistance needs to have an exponential dependence on the magnetization for large M, which reduces to M^2 for small M , such as that previously suggested by Sun *et al.* [23] $\sigma \propto M^2 \exp[M / M_E]$.

Appendix A. Critical Behavior and Anisotropy in Single Crystal $SrRuO_3$

Introduction

Strontium ruthenate, $SrRuO_3$, has many physical properties which make it unique among perovskite oxides. First, it is metallic in the undoped state [36, 126, 173-176]. This is even more unusual since the ruthenium in $SrRuO_3$ is in a high oxidation state; whereas many other metallic perovskites must be formed in reducing environments and therefore unstable in air at high temperatures. The remarkable chemical stability and simple chemical formula makes metallic $SrRuO_3$ quite attractive for use in epitaxial thin film heterostructures with other perovskite oxides when metallic layers are desired. Indeed, the nearly cubic $SrRuO_3$ [177] is often preferred over the more distorted $CaRuO_3$ when making structures such as electrodes for ferroelectrics or superconductor-normal metal-superconductor junctions.

The other striking feature of $SrRuO_3$ is its ferromagnetism with a reasonably high transition temperature (163 K) and large saturation moment ($> 1\mu_B$) [174, 175, 178, 179]. $SrRuO_3$ is the only ferromagnetic perovskite oxide of a 4*d* or 5*d* transition metal. Moreover, $SrRuO_3$ has the largest saturation moment known to arise from 4*d* electrons, making it more related to the iron group ferromagnetic metals (Fe, Co and Ni) than to the weak itinerant electron ferromagnets such as $ZrZn_2$. $SrRuO_3$ also has very strong cubic magnetic anisotropy, requiring magnetic fields in excess of 10 Tesla to saturate the magnetization in the hard directions. Such a strong anisotropy makes measuring even the simplest properties, such as saturation magnetization, difficult. It is the purpose of the present work to determine the magnetic properties of $SrRuO_3$ by measurements of magnetically-soft single crystals along the easy magnetic direction.

There have been several studies of $SrRuO_3$ in the past three decades, mostly on polycrystalline samples which are quite easy to prepare. $SrRuO_3$ has a very slightly distorted ($GdFeO_3$ type) perovskite structure. The deviation from perfect cubic perovskite is so small that it has often been undetected. The resistivity of polycrystalline, and epitaxial thin film $SrRuO_3$ shows a cusp in $d\rho/dT$ at the ferromagnetic Curie temperature T_C. This is commonly observed for metallic ferromagnets and is attributed to spin disorder scattering [125]. Reported T_C's tend to vary from 150K to 165K.

The saturation magnetization of $SrRuO_3$ has been both difficult to measure and interpret. Low spin Ru^{4+} in an octahedral coordination has four $4d$ electrons in the t_{2g} triply degenerate state, giving two paired and two unpaired electrons. Since the orbital component of angular momentum J will be quenched, $J = S = 1$ is expected. The measured Curie constant of the paramagnetic state is consistent with this model (expected: $\mu_{eff} = \sqrt{2}gJ(J + 1)\ \mu_B = 2.83\ \mu_B$; measured = $2.67\ \mu_B$ [175]). For a localized moment ferromagnet, the saturation magnetization M_S is predicted to be $M_S = gJ\ \mu_B = 2.0\ \mu_B$ for $SrRuO_3$. Measured values of M_S are much less. Polycrystalline $SrRuO_3$ reaches about $0.85\ \mu_B$ [175, 178, 179] in low fields but continues to increase in higher magnetic fields. At 125 kOe it was noted that M had reached $1.55\ \mu_B$ but had not yet saturated [178]. Early neutron diffraction derived a moment of $1.4 \pm 0.4\ \mu_B$ [178] with no evidence for any antiferromagnetic order (spin canting). Recent theoretical investigations predict incomplete band splitting and a large moment of about $1.6\ \mu_B$ [176, 180]. Early explanations for the low value of M_S included spin canting, band magnetism, and incomplete alignment of the magnetization due to magnetocrystalline anisotropy [178]. The present work shows that $SrRuO_3$ has a large saturation moment of $1.6\ \mu_B$ as predicted by these calculations.

Single crystals of $SrRuO_3$ can be grown from a $SrCl_2$ flux [36]. The resistivity of such crystals is consistent with the results on polycrystalline

samples. Magnetization and magnetic torque measurements of single crystals [181-183] showed that $SrRuO_3$ has a high cubic anisotropy with ⟨110⟩ (cubic cell) being the easy direction, with nearly square hysteresis loops. Some previous measurements reported for single crystals are questionable, for example, the measured value of $M_S = 1.1\ \mu_B$. In this work new magnetization data is shown to clarify these points.

Experimental

Single crystals of $SrRuO_3$ were grown by slow cooling in a $SrCl_2$ flux [36, 184]. Polycrystalline $SrRuO_3$ was prepared from stoichiometric quantities of $SrCO_3$ and Ru metal repeatedly reacted at 1260°C, and was used as the source material for crystal growth. The $SrCl_2$ was dried in air at 110°C. A mixture with approximate weight ratio 1:20 of $SrRuO_3$:$SrCl_2$ was melted in a platinum crucible with lid at 1260°C for 94 hrs. The sample was cooled to 800°C at 1°/hr and then to room temperature at ~40°/hr. Crystals of $SrRuO_3$ less than 1 mm in diameter were found at the bottom of the crucible after removing the flux with water. Most crystals were cubo-octahedron shaped and grew with a 3-fold symmetric axis (presumably [111]) perpendicular to the Pt surface. The (cubic) crystal orientation was determined by the symmetry of the faces. The actual orthorhombic symmetry [177] was confirmed by powder x-ray diffraction and Transmission Electron Microscopy.

Magnetization in fields up to 70 kOe was measured using a Quantum Design $MPMSR_2$ SQUID magnetometer. The samples were attached to a plastic straw with a small amount of Apiezon N vacuum grease. Samples were oriented on the straw visually using crystal faces which had obvious 2-, 3- and 4-fold rotational symmetry. At room temperature, the crystal can rotate in a large field to align a paramagnetic easy direction with the field. This was used as a final adjustment when aligning along the easy ⟨110⟩

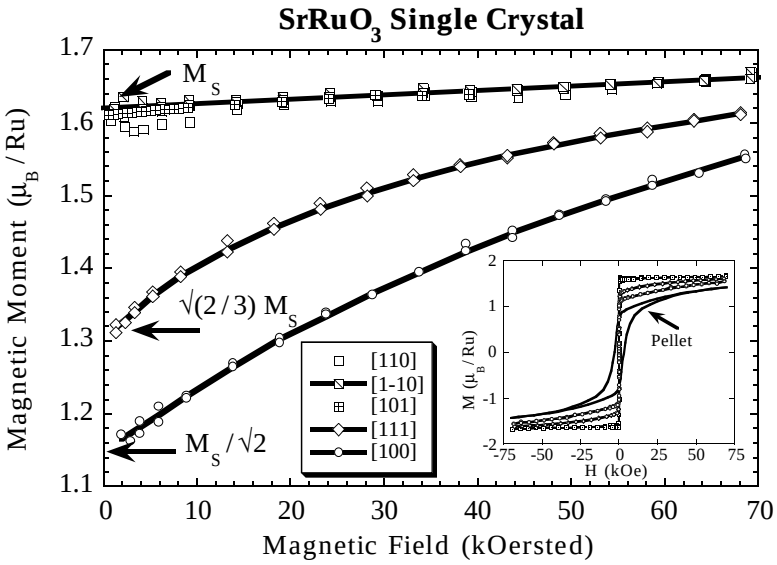

Figure A- 1. Magnetization at 5 K of $SrRuO_3$ single crystal along several crystallographic directions showing strong cubic but not uniaxial magnetocrystalline anisotropy. Inset shows the full hysteresis loop of the single crystal data along with that of a polycrystalline pellet for comparison.

directions. At low temperatures, the grease solidifies so the sample cannot rotate. The accuracy of the magnetization measurement was estimated by measuring a sphere of yttrium iron garnet described in section 3.2.1.1. For the measure-ments reported here, the sample holder was fixed at the rotation angle which gave the maximum magnetization. Several crystals were measured.

Results

Figure A- 1 shows hysteresis loops at 5 K for $SrRuO_3$ single crystal in various crystallographic directions and a polycrystalline pellet. The crystals have a low coercive field (≈ 10 Oe) compared to that of the polycrystalline pellet (3000 Oe). But more importantly, the crystals show very little hysteresis

while the pellet displays noticeable hysteresis even in fields greater than 40 kOe.

The rapid, linear approach to saturation (with respect to the applied field) found in all directions can be attributed to demagnetization. Until the sample becomes fully magnetized, the demagnetization field H_d is equal to the applied field H_a resulting in an internal field of zero ($H_i = H_a - H_d$). From this slope ($M = H_a / 4\pi N$), one can calculate the demagnetization factor N and therefore calculate the internal field. The measured demagnetization factors N, ($H_d = 4\pi NM$) are 0.25, 0.28, 0.31, 0.49, 0.66 for the [110], [1-10], [101], [100] and [111] directions respectively. These seem reasonable considering the shape of the crystals. Since a uniaxial magnetocrystalline anisotropy will also give a linear increase in M if H is applied along the hard direction, it is difficult to distinguish it from the effect of the demagnetization field in this study. Since the demagnetization field can be as large as a thousand Oersted, one can only conclude that the uniaxial anisotropy field is less than a thousand Oersted, which is considerably less than that (> 50 kOe) reported previously [182].

In the [110] direction $SrRuO_3$ rapidly approaches saturation and then remains relatively constant (square hysteresis loop), as is expected for a magnet with a magnetic field along the easy direction. The crystal was also measured in the [1-10] and [101] directions which would be equivalent by symmetry to the [110] if the crystals were cubic. Since the magnetization is the same along these ⟨110⟩ type directions, it can be concluded that the magnetic properties of single crystal $SrRuO_3$ are essentially cubic, *i.e.* only cubic magnetocrystalline anisotropy is detected. Beyond this initial saturation along the easy ⟨110⟩ directions, there is a small but measurable increase in the magnetization which is linear in magnetic field and has a slope of 6×10^{-7} μ_B/Oe.

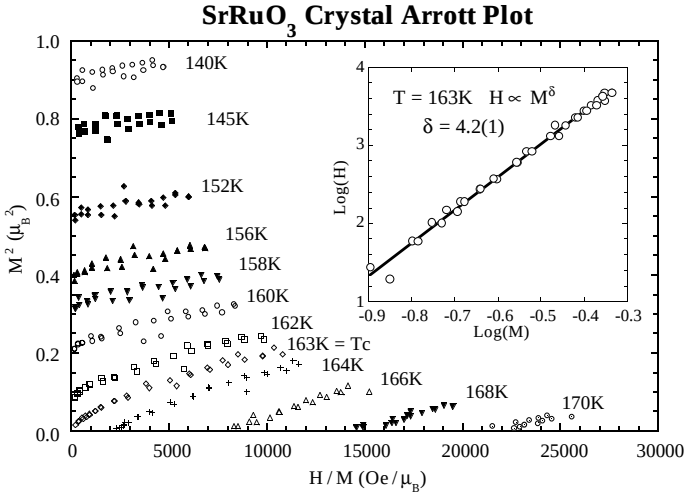

Figure A- 2. Arrott Plot of $SrRuO_3$ single crystal along easy [110] direction. Inset, critical isotherm (T = 163K ≈ T_C) on a log scale fit to $M^{\delta} \propto H$ with δ = 4.2.

The H = 0, T = 0 saturation moment M_S found along the easy ⟨110⟩ directions are about 1.62 μ_B/Ru. In the remnant state (H reduced to zero), the magnetization should lie along the nearest easy direction. Thus the expected remnant (H = 0) magnetization along the [100] or [111] direction is simply the cosine of the angle it makes with the closest ⟨110⟩ direction. For ⟨100⟩ the expected remnant magnetization is $M_S/\sqrt{2}$, and for ⟨111⟩ directions $\sqrt{(2/3)}M_S$ is expected. These are extremely close to the experimental values (Figure A- 1).

In the other primary directions, there is a nonlinear approach to saturation which is characteristic of materials with cubic anisotropy. The magnetocrystalline anisotropy constants K_1 and K_2 can be estimated from these magnetization curves [185]. The magnetocrystalline anisotropy energy E can be defined in terms of the cosine of the angle **M** makes with the three crystal axes: $\alpha_i = \mathbf{x}_i \bullet \mathbf{M}/M$. For a cubic material $E = K_1 (\alpha_1^2\alpha_2^2 + \alpha_2^2\alpha_3^2 + \alpha_3^2\alpha_1^2) +$

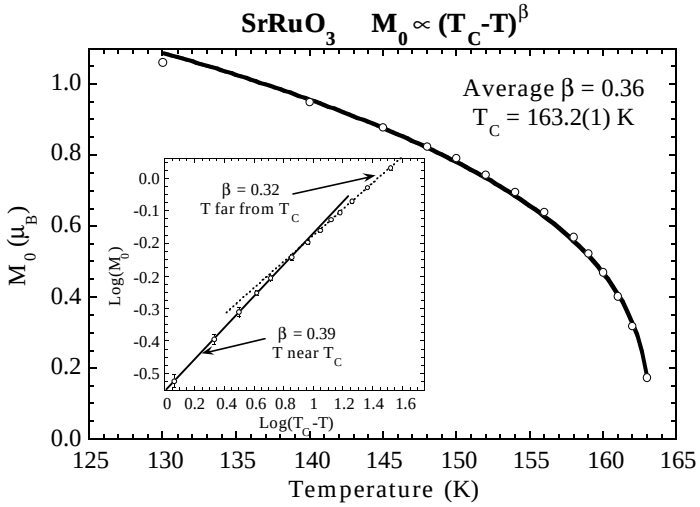

Figure A- 3. Zero field magnetization M_0 of $SrRuO_3$ single crystal along easy [110] direction. Solid line shows the fit to $M_0(T) \propto (1 - T/T_C)^{\beta}$ with $\beta = 0.36$. Inset showing the same data on a log plot. The critical exponent β appears to change from Heisenberg-like $\beta = 0.39$ near T_C to Ising-like $\beta = 0.32$ as T decreases.

$K_2 (\alpha_1^2\alpha_2^2\alpha_3^2) + \ldots$. In $SrRuO_3$ the magnetic easy axes are $\langle 110 \rangle$, which requires $K_1 < 0$. Similarly, $\langle 100 \rangle$ are the hard axes ($\langle 111 \rangle$ are intermediate) which implies $2.25|K_1| < K_2 < 9|K_1|$. The [100] magnetization should intersect that of the easy axis [110] at $H_a = -2K_1/M_S$. An extrapolation of the [100] *M vs. H* curve gives $-2K_1/M_S \approx 109$ kOe. Alternatively, the area between the [100] and the [110] *M vs. H* curves should be equal to $-K_1/4$. This method gives a value for $-2K_1/M_S \approx 96$ kOe. The area method can also be used with the [111] curve to estimate $2K_2/M_S \approx 540$ kOe.

In the easy [110] direction, *M vs. H* curves were measured for various temperatures and are shown in Figure A- 2 as M^2 vs. H/M (Arrott plot). The isotherms below T_C should be approximately linear and intersect $H/M = 0$ at M_0.

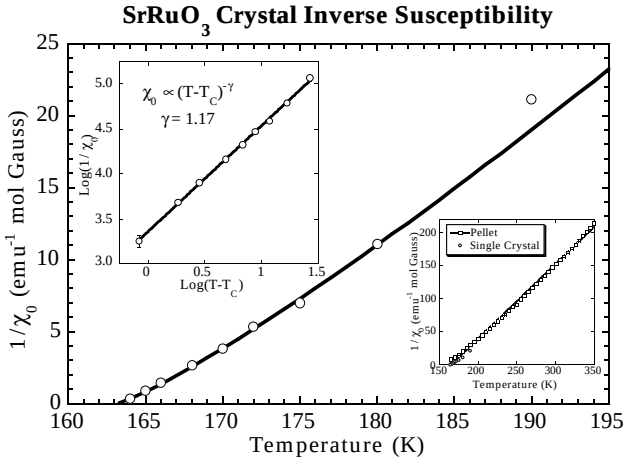

Figure A- 4. Zero field inverse susceptibility $1/\chi_0$ of $SrRuO_3$ single crystal along easy [110] direction. Solid line shows the fit to $1/\chi_0(T) \propto (1 - T/T_C)^{\gamma}$ with $\gamma = 1.17$ and $T_C = 163.2$ K. The inset shows the same data on a log plot.

From these $M_0(T)$, shown in Figure A- 3, the critical exponent $\beta \approx 0.36$ and $T_C = 163.2 \pm 0.2$ K can be estimated by fitting $M_0(T) \propto (1 - T/T_C)^{\beta}$ in the critical region. The fit with a single value for $\beta = 0.36$ is poor considering the apparent precision of the data. Closer to T_C, the data fit better with a larger $\beta \approx 0.39$ which is close to that predicted in the 3-*d* Heisenberg model ($\beta = 0.38$). Farther from T_C, the exponent is smaller, $\beta \approx 0.32$, near that predicted by the Ising model ($\beta = 0.33$). It is possible that this is due to a crossover from Heisenberg to Ising behavior at T decreases from T_C. A similar model has been proposed to explain measurements of thin film $SrRuO_3$ [73].

The $T > T_C$ isotherms of Figure A- 2 should intersect $M^2 = 0$ at $1/\chi(T, H = 0) = 1/\chi_0$. The critical exponent γ is then found from $1/\chi_0 \propto$

$(T/T_C - 1)^{\gamma}$. From these data (Figure A- 4) $\gamma = 1.17 \pm 0.02$ is estimated. The plot of $1/\chi$ vs. T should be close to linear for high temperatures.

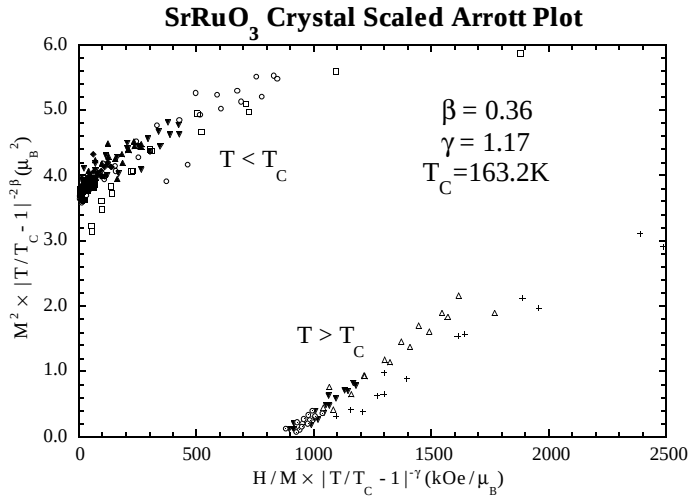

Figure A- 5. Scaled Arrott Plot of $SrRuO_3$ single crystal along easy [110] direction with $\beta = 0.36$ and $\gamma = 1.17$. Symbols are the same as those used in Figure A- 2.

The $M(H, T)$ data can be replotted using the scaling hypothesis [90] with $\beta = 0.36$ and $\gamma = 1.17$. According to the hypothesis, the magnetic equation of state in the critical region depends only on the scaled variables $H/|T_C/T - 1|^{\beta+\gamma}$ and $M/|T_C/T - 1|^{\beta}$. A plot of the scaled M^2 and scaled H/M, shown in Figure A- 5, will then have only two curves: one branch for the $T < T_C$ data and another for $T > T_C$. Not all the curves fit on a single line, this is due to the apparent change in β as discussed above.

The critical isotherm ($T = T_C$) should obey the relation $M^{\delta} \propto H$, where according to the scaling relation $\delta = \gamma/\beta + 1$. From the previously measured values of β and γ, the exponent δ is therefore expected to be 4.3 ± 0.5. This is in good agreement with the measured value (Figure A- 2) $\delta = 4.2 \pm 0.2$.

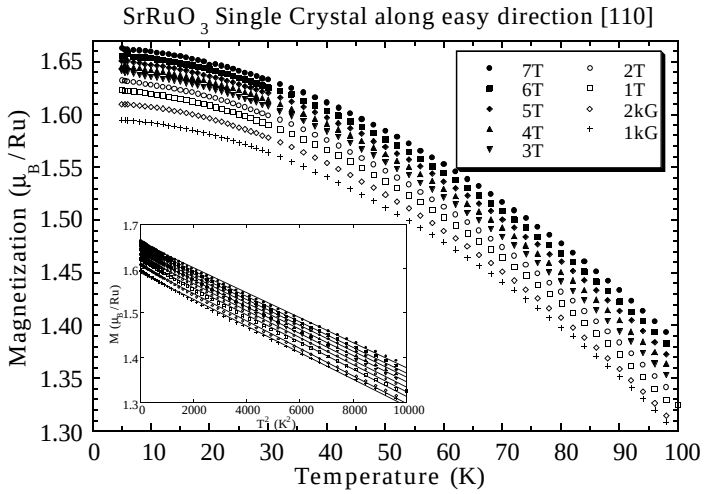

Figure A- 6. Magnetization as a function of temperature of $SrRuO_3$ single crystal along easy [110] direction. Inset shows the approximate T^2 dependence of the magnetization.

The temperature dependence of M along the easy direction is shown in Figure A- 6 for various applied fields. The demagnetization field of $4\pi NM \approx$ 800 Oe should be subtracted from the applied field to give the internal field. Between 5 K and 100 K, and for internal fields from 0.2 kOe to 68 kOe the magnetization is well approximated by $M = M_0(1 - (T/\Theta_2)^2)$ where M_0 and Θ_2 are fitting parameters. Other possible analyses are discussed below.

Discussion

The low temperature magnetization data (Figure A- 1) of bulk $SrRuO_3$ can be explained with ⟨110⟩ easy directions and a large cubic, but very little uniaxial, magnetocrystalline anisotropy. The low coercivity of the crystals (~10 Oe), compared to the 3 kOe coercivity found in polycrystalline samples,

provides highly reversible and square hysteresis curves. There is no indication of a magnetic multi-domain structure [183].

The cubic magnetocrystalline anisotropy in $SrRuO_3$ is very large, as reported previously [181, 183]. Typical values of K_1 for cubic 3-*d* ferromagnets are 100 times smaller than that found for $SrRuO_3$. Such large values of K_1 usually refer to uniaxial anisotropy, for instance in hexagonal materials, which is a lower order effect (K_1 refers to the first non-zero anisotropy constant). This large anisotropy probably results from the strong spin-orbit coupling of the heavy Ru atom, which also gives $SrRuO_3$ a strong Kerr effect [186].

From measurements along different ⟨110⟩ directions, no indication of uniaxial magnetocrystalline anisotropy [182] is found, although it is allowed from the orthorhombic symmetry. This might be expected since the crystallographic unit cell lengths [177] vary by only 0.03%, and the angles by 0.4% from the perfect cubic ones. The distortion from cubic is primarily due to a rotation of the RuO_6 octahedra, which alters the symmetry much more than the shape of the unit cell [177]. In the crystals reported here, the orthorhombic cell was confirmed using TEM. Because the unit cell is only slightly distorted, the few reports claiming cubic [184] or tetragonal [182] crystallographic symmetry without supporting evidence, should be reevaluated in this context. Significant uniaxial anisotropy reported in thin films of $SrRuO_3$ [187] may result from growth induced anisotropy, as was found in films of magnetic garnets used in magnetic bubble technology [188].

Due to the large magnetocrystalline anisotropy, the saturation moment of $SrRuO_3$ is difficult to measure. In directions other than ⟨110⟩ the magnetic moment does not saturate even in fields of several 10 kOe. The strain and small particle size of a polycrystalline sample apparently makes it even more difficult to saturate than the hard direction in a single crystal (Figure A- 1). Polycrystalline $SrRuO_3$ has a remnant magnetization ($H = 0$) of $M_S \approx 0.85\ \mu_B$,

which increases non-linearly past 1.55 μ_B (H = 125 kOe) [178]. Clearly a magnetically soft single crystal with H along the easy direction is needed to measure M_S. In a previous experiment [181] on single crystal $SrRuO_3$ with a square hysteresis loop, M_S = 1.1 μ_B at H = 0 was reported. However, that value of M_S is clearly too small since by 17 kOe it is smaller than the value for a polycrystalline sample [181]. Our measured value of M_S = 1.6 μ_B (H = 0) is consistent with the high field polycrystalline results.

The magnetic critical exponents measured here are in the range typically seen in large moment ferromagnets and expected theoretically for 3-dimensional ferromagnets. Experimental values for the critical exponent β in Fe, Ni and YIG [92] are 0.37 ± 0.02, which are near the theoretical values (Ising β = 0.33, Heisenberg β = 0.36). The related metallic ferromagnets $La_{0.5}Sr_{0.5}CoO_3$ [92] has β = 0.361. The apparent decrease in β as T decreases from T_C, may be due to the large magnetocrystalline anisotropy. A similar effect has been seen in thin film $SrRuO_3$ [187], where it is suggested that the magnetocrystalline anisotropy induces a crossover from Heisenberg to Ising behavior. The weak, itinerant electron ferromagnet $ZrZn_2$ has mean field critical exponents β = 0.5 [93]. The most prominent theory on itinerant electron ferromagnetism by Moriya [84, 85] predicts a $T_C^{4/3}$ - $T^{4/3}$ dependence on the magnetization, which is essentially β = 1.

The critical exponents γ and δ are also typical for large moment ferromagnets (Fe, Ni and YIG [92] γ = 1.2 ± 0.2) as opposed to those found for the weak, itinerant electron ferromagnet $ZrZn_2$ which has mean field critical exponents γ = 1.0 and δ = 3 [93]. The three dimensional Ising and Heisenberg models predict γ = 1.24, δ = 4.8 and γ = 1.39, δ = 4.8 respectively. The critical exponents measured here also obey the scaling relation $\delta = 1 + \gamma/\beta$.

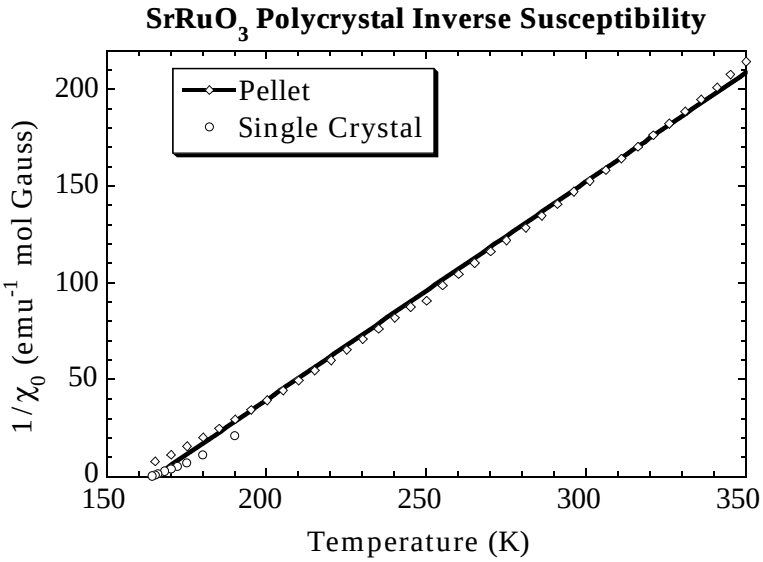

Figure A- 7. Inverse magnetic susceptibility ($1/\chi = M/H$) at H = 10 kOe of polycrystalline $SrRuO_3$ compared to the single crystal data from Figure A- 4. The solid line is the straight-line fit with T_C = 165K which demonstrates the slightly positive curvature of the data.

A positive curvature persists in the plot of $1/\chi$ *vs.* T (Figure A- 7) even at higher temperature where it should be linear for a Curie-Weiss ferromagnet. Such a curvature can be caused by a temperature independent term in the susceptibility $\chi = \chi_{Const} + C/(T - \Theta)$, where $C/(T - \Theta)$ is the Curie-Weiss susceptibility and is always positive ($T > \Theta$). A $\chi_{Const} < 0$ of about -4×10^{-4} emu G^{-1} mol^{-1} will provide the observed curvature, and has been independently observed elsewhere [175]. The temperature independent term χ_{Const}, should contain a positive contribution due to Pauli paramagnetism. This can be estimated from measurements of the linear term of the specific heat [176], giving $\chi_{Pauli} \approx +4 \times 10^{-4}$ emu G^{-1} mol^{-1}. The Landau diamagnetism should be

negative and for simple band structures is smaller than χ_{Pauli} (for free electrons $\chi_{Landau} = -\chi_{Pauli}/3$). The core diamagnetism can be estimated from tables of experimental values [76] giving $\chi_{Core} = -0.7 \times 10^{-4}$ emu G^{-1} mol^{-1}. The sum of these theoretical estimates $\chi_{Const} = \chi_{Pauli} + \chi_{Landau} + \chi_{Core}$ is, however, still positive while the experimental value appears to be negative. In the critical region, $1/\chi \propto (T/T_C - 1)^{\gamma}$ with $\gamma = 1.17$, provides a positive curvature in the plot of $1/\chi$ *vs.* T. Since the mean field exponent $\gamma = 1$ is expected to be valid far from T_C, some other mechanism must provide the effective $\gamma > 1$ observed at these higher temperatures.

Magnetic excitations which become thermally induced as the temperature is raised above $T = 0$ reduce the magnetization from the ground state value. The exponential decrease predicted by the mean field model has some qualitative value but is never in good agreement with experiment. Collective spin wave excitations and single particle (Stoner) excitations both decrease the magnetization according to a power law $M = M_S(1 - (T/\Theta_n)^n)$ which is in accord with experiments where $n \approx 2 \pm 1$ and Θ_n is of the order T_C.

The limiting low T, $H = 0$ behavior of collective, spin wave excitations (section 3.2.2.2.8) predicts $n = 3/2$ and for $SrRuO_3$, $\Theta_{3/2} \approx 2.42T_C = 400$ K. The Stoner theory of single (*k*-space) particle excitations (section 3.2.2.2.2) predicts $n = 2$ and $\Theta_2 \approx 1.41\ T_C$ (= 230 K for $SrRuO_3$). As the temperature and magnetic field is raised, these models require further corrections. For example, higher order corrections such as an additional $n = 5/2$ term in predicted in the spin wave theory. For $H \neq 0$, the low temperature spin-wave excitations become quenched which can have the effect of increasing the average value on n [97]. The generalized model of spin fluctuations in ferromagnets ([84] section

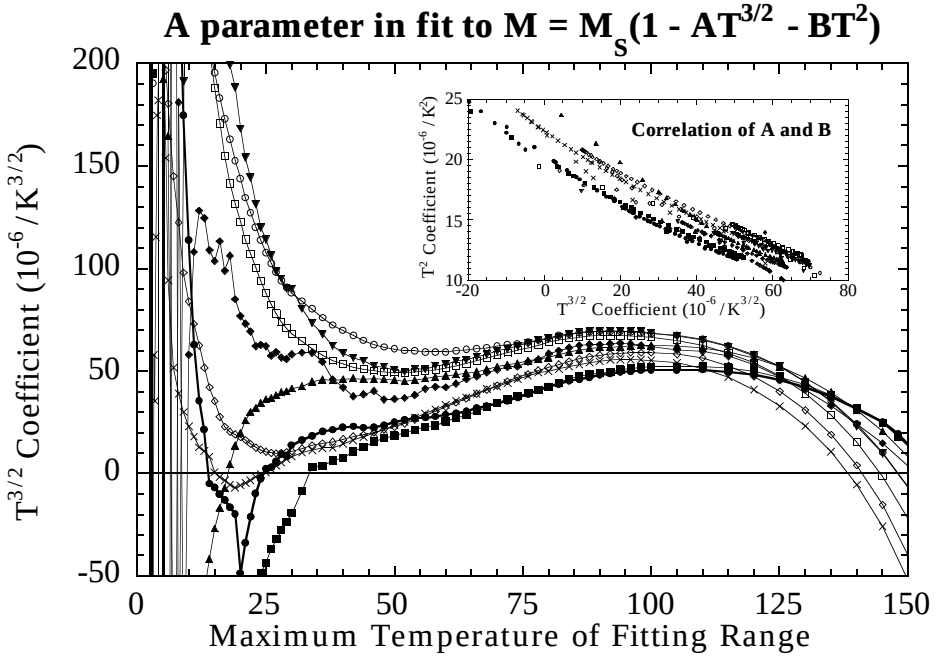

Figure A- 8. Variation of the $T^{3/2}$ parameter in fitting the magnetization data of single crystal $SrRuO_3$ to $M = M_S$ (1 - $AT^{3/2}$ - BT^2) as the fitting range is increased. The upper inset shows the correlation of the A and B parameters. In the region where A is relatively stable (around T_{max} = 60 K), A decreases as T_{max} is lowered. The symbols are the same as those used in Figure A- 9.

3.2.2.2.3) includes both types of interacting magnetic excitations and predicts $n = 3/2$ for $H = 0$, $T = 0$ but also $n \approx 2$ in calculations [86].

Experimental results on metallic ferromagnets with substantial saturation moments such as Fe, Ni [88, 189-192] and $La_{0.67}Sr_{0.33}MnO_3$ ([97], section 4.1.1) can display $n = 3/2$ consistent with the spin wave stiffness determined by neutron diffraction if significant corrections are included and only low temperature data is analyzed. In contrast "weak" itinerant-electron

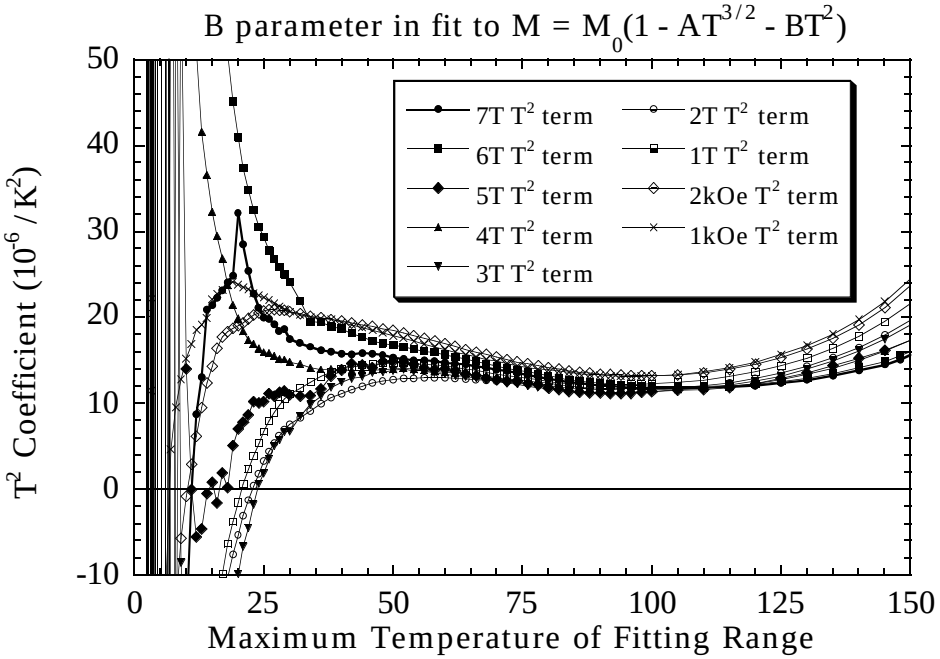

Figure A- 9. Variation of the T^2 parameter in fitting the magnetization data of single crystal $SrRuO_3$ to $M = M_S$ (1 - $AT^{3/2}$ - BT^2) as the fitting range is increased. In the region where B is relatively stable (around T_{max} = 60 K), B increases as T_{max} is lowered.

ferromagnets such as $ZrZn_2$, Ni_3Al and Sc_3In, show n = 2 [86, 193-195] over a wide temperature range.

As shown above (Figure A- 6) the magnetization of $SrRuO_3$ single crystal can be well described by $M = M_S(1 - (T/\Theta_n)^n)$ with n = 2 in the temperature range of reliable measurement, 5 K to 100 K. A fit with n = 3/2 in this temperature range is unsatisfactory.

If one assumes n = 2 arises from Stoner excitations and collective excitations result in n = 3/2, then one may expect the variation of

magnetization with temperature to fit with a combination of the $n = 2$ and $n = 3/2$ terms, $M = M_S (1 - AT^{3/2} - BT^2)$ [150] at low temperatures. Since an additional parameter is included, an improvement of the fit does not necessarily prove the significance of the added parameter. Furthermore, the functions $T^{3/2}$ and T^2 are very similar making the fitting parameters highly correlated.

The magnetization data for single crystal $SrRuO_3$ were fit to a polynomial expression $M = M_S (1 - AT^{3/2} - BT^2)$ from $T = 2$ K to $T = T_{max}$. As expected, the A and B parameters are highly correlated (Figure A- 8) with $\Delta B \approx 2.2 \times 10^{-5}$ K^{-2} - 0.2 K$^{-1/2}$ ΔA. The parameters A and B can then be plotted as a function of T_{max} (Figure A- 8 and Figure A - 9). For very low T_{max} (< 30 K) the fit is unstable since the difference in the magnetization at $T < T_{max}$ becomes comparable to precision of the measurement. Thus, the divergence of the fitting parameters at low T_{max} is an artifact, and not physical. At high temperatures, nearing the critical temperature, the polynomial expression is not expected to be valid, so the divergence at high T_{max} can also be ignored. The flat, linear region centered around T_{max} = 60K, is presumably the region where the fitting parameters may have physical meaning. From this region, A and B parameters can be extracted and extrapolated to the $T_{max} = 0$ K values for comparison with the theory. This analysis was done for fitting the magnetization data both to $M = M_S (1 - AT^{3/2} - BT^2)$ and $M = M_S (1 - BT^2)$.

Implicit in the use of $M = M_S (1 - AT^{3/2} - BT^2)$ is the assumption that these two terms are theoretical low temperature expansions, *i.e.* they should become more accurate as T approaches 0 K. As the temperature range for which the data is fit to this type of expression is decreased to lower temperatures, the fitting parameters should be stable, or only be slightly varying. In principle, the true low temperature form should gradually become more dominant, at the expense of the other terms, as the fitting range is decreased to lower temperatures.

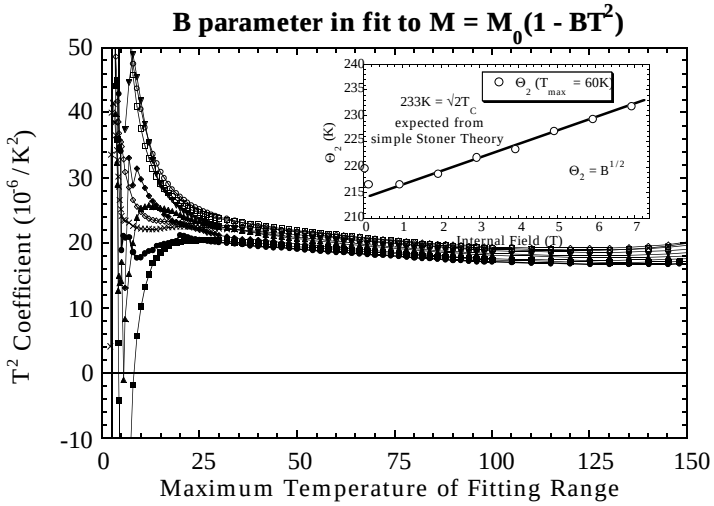

Figure A- 10. Variation of the T^2 parameter in fitting the magnetization data of single crystal $SrRuO_3$ to $M = M_S (1 - BT^2)$ as the fitting range is increased. The parameter B for this fit is more stable and constant than that shown in Figure A- 8. Inset, variation of Θ_2 in a magnetic field.

In fitting to the data on $SrRuO_3$ single crystal the B parameter (Figure A-9) is relatively stable and increases as lower temperature fitting ranges (T_{max}) are used. The A parameter (Figure A- 8) is not as stable and appears to decrease as T_{max} is lowered. If this trend were to continue, then the $T^{3/2}$ contribution would be very small at low temperatures. The removal of the $AT^{3/2}$ term further stabilizes the B parameter (Figure A- 10), and makes B more independent of T_{max} than with $AT^{3/2}$ included. Thus, from this analysis of the magnetization data, there is little evidence for a large $AT^{3/2}$ contribution to the magnetization. This is in contrast with measurements on thin film [186, 187] which show $T^{3/2}$ dominating over T^2.

The two corrections to the spin wave $T^{3/2}$ theory mentioned above (finite magnetic field and higher order $T^{(2n+1)/2}$ terms) may not adequately explain the data presented here. The applied magnetic field will suppress spin wave

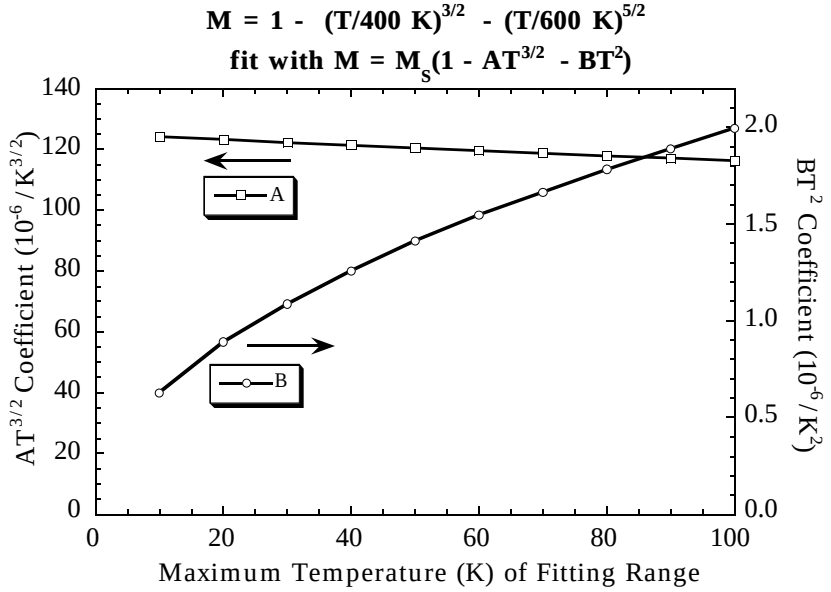

Figure A- 11. Variation of *A* and *B* fitting parameters in the hypothetical case where the true magnetization is given by $T^{3/2}$ and $T^{5/2}$ terms.

excitations for $T < g\mu_B H / k_B$, resulting in an effective $n > 3/2$. If this were a significant effect, the $T^{3/2}$ fitting parameter A should decrease as H is increased particularly as T_{max} approaches 0 K. Such a systematic decrease in A is not obviously apparent (Figure A- 8). One cannot however, exclude the demagnetization or anisotropy field which are present even when the applied $H = 0$.

If the true magnetization were a sum of $T^{3/2}$ and $T^{5/2}$ terms, $M/M_S = (1 - (T/400\text{ K})^{3/2} - (T/600\text{ K})^{5/2})$ for instance, the data would fit well to $M/M_S = (1 - AT^{3/2} - BT^2)$. The fitting parameters A and B as a function of T_{max} for this example are shown in Figure A- 11. The A parameter is relatively constant, increasing slightly as T_{max} approaches 0 K. In the limit T_{max} approaches 0 K, $A = 125 \times 10^{-6}$ K$^{-3/2}$ or $\Theta_{3/2} = 400.3$ K, which is very close to the true value of 400 K. The B fitting parameter is not nearly as stable and decreases as T_{max}

approaches 0 K. Since the exponent of the BT^2 fit (2) is smaller than 5/2, which is the exponent used in the example, a larger B is needed to fit the data at higher temperatures. Thus, a dramatically decreasing B as T_{max} approaches 0 K, is indicative of a fitting exponent (2 in this example) smaller than the true exponent (5/2 in this example).

The data on $SrRuO_3$ shows the opposite effect: B is relatively constant while A decreases as T_{max} approaches 0 K. This decrease of A indicates that the exponent 3/2 is smaller than the true exponent, and therefore, the addition of higher order terms to the spin wave form of the magnetization will not fully explain the data on $SrRuO_3$.

Positive B (and A) parameters can be converted to the Θ_n values used above via $\Theta_2 = B^{-1/2}$ and $\Theta_{3/2} = A^{-2/3}$. The Θ_2 values extracted from fits described above are shown as a function of the internal magnetic field in Figure A- 10. The values of $\Theta_2(H)$ extrapolated to $T_{max} = 0$ are 20 K less than the corresponding $\Theta_2(H)$ for T_{max} = 60 K. The single crystal Θ_2 parameters increase only slightly as the field is increased, about 2.6 K/Tesla. These values for Θ_2 are consistent with measurements of the field dependent heat capacity of polycrystalline $SrRuO_3$ (Figure B- 3) via the Maxwell relation $\left(\frac{\partial C_H}{\partial H}\right)_T = T\left(\frac{\partial^2 M}{\partial T^2}\right)_H$.

Conclusion

Various magnetic properties of single crystal $SrRuO_3$ along the magnetic easy direction have been measured. The saturation moment, $1.61\mu_B$/Ru, is larger than that reported previously for single crystal material but in accord with experiments on polycrystalline material and theoretical calculations. The crystals show extremely large cubic magnetocrystalline anisotropy while no substantial uniaxial magnetocrystalline anisotropy. The critical exponent

β changes from Heisenberg like 0.39 near T_C to Ising like 0.32 further from T_C. The susceptibility exponent γ = 1.17 persists to 2 T_C, where it is expected to decrease to 1. The magnetization from 5 K to 100 K is well described by $M = M_S(1 - (T/\Theta_n)^n)$ where $n \approx 2$. The addition of a $T^{3/2}$ term is not obviously significant.

Appendix B. Magnetic Excitations and Specific Heat in $SrRuO_3$

Low temperature magnetic excitations can be probed not only by measurements of the magnetization but also by the heat capacity. As will be discussed below, the two measurements are related via a Maxwell relation.

$SrRuO_3$ polycrystalline samples were prepared by repeated heating of a Ru and $SrCO_3$ mixture at 1260°C (seciton 2.1.1). Heat capacity data were taken using the relaxation method [102] (section 3.3). Constant field data were taken on a zero field cooled sample at 0 and 8 T, and in zero field after the application of an 8 T field. In addition, data at temperatures between 4 K and 5 K were taken at several intermediate fields.

Specific heat data taken in 0 T and 8 T applied magnetic field are shown in Figure B- 1. The zero field cooled and zero field remnant data are equal within experimental error. Between 3 K and 13 K both the 0 T and 8 T data appear to be well described by a straight line on this plot of c/T vs. T^2, suggesting that the specific heat can be described by $\gamma T+\beta T^3$. The parameter values from fitting the data in zero field are γ = 37 mJ mol^{-1} $K^{-2}$and β = 0.19 mJ mol^{-1} K^{-4}. This value of β corresponds to a Debye temperature of 371 K and is in good agreement with previous zero-field measurements [176, 196], while γ is about 20% larger than that found previously. The value of γ in zero field, 37 mJ mol^{-1} K^{-2}, is 4.6 times that expected of the bare density of states given by spin resolved band structure calculations [176]. The effect of demagnetization fields should be negligible since the correction to the specific heat is approximately proportional to T^3 but only about 0.1% of the measured value of β [197, 198].

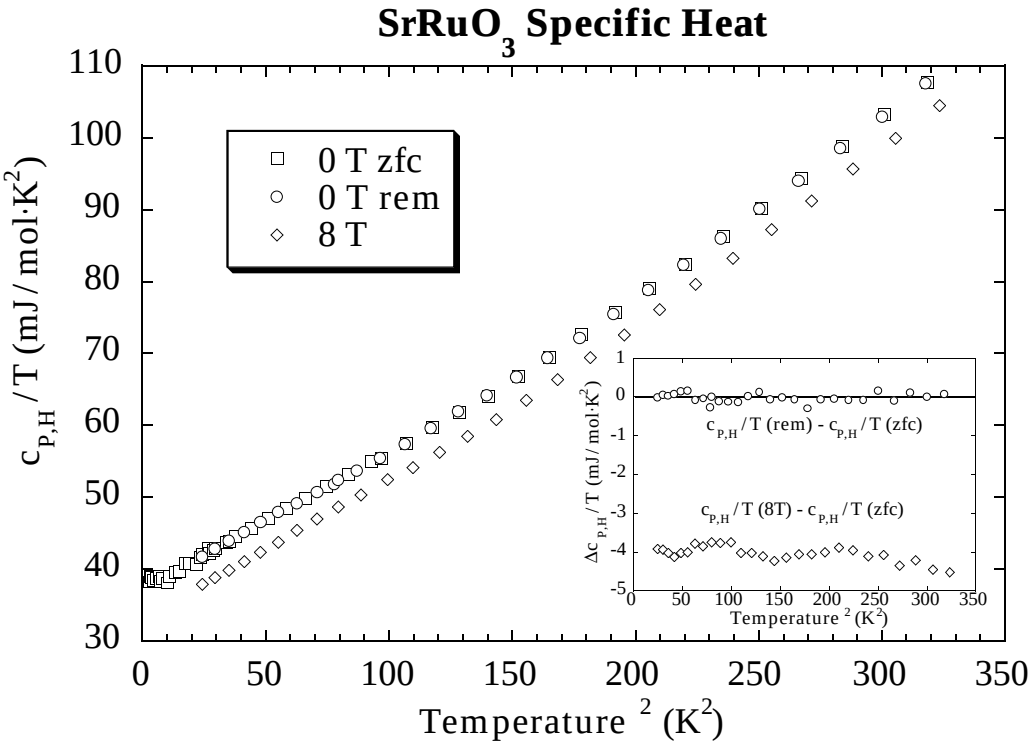

Figure B- 1 Heat capacity of $SrRuO_3$ cooled in zero field (zfc), in an 8 T magnetic field, and in zero field after being magnetized (rem). Inset, difference between the heat capacity measured after cooling in zero field with that in 8 T and the remnant magnetized state.

Above 13 K and below 3 K the data in Figure B- 1 deviate from a straight line. The deviation above 13K can be fit by an expression for the specific heat of a thermally activated Einstein (optical) phonon mode, with an Einstein temperature of Θ_E = 140 K. Both β and Θ_E are field independent within experimental error. The temperature range below 3 K is not large enough to draw conclusion about the functional form of the low-temperature upturn. A field independent term proportional to $T^3\ln(T)$ is expected from the non-spinwave spin fluctuations [91, 194, 199]. A Shottky anomaly due to free

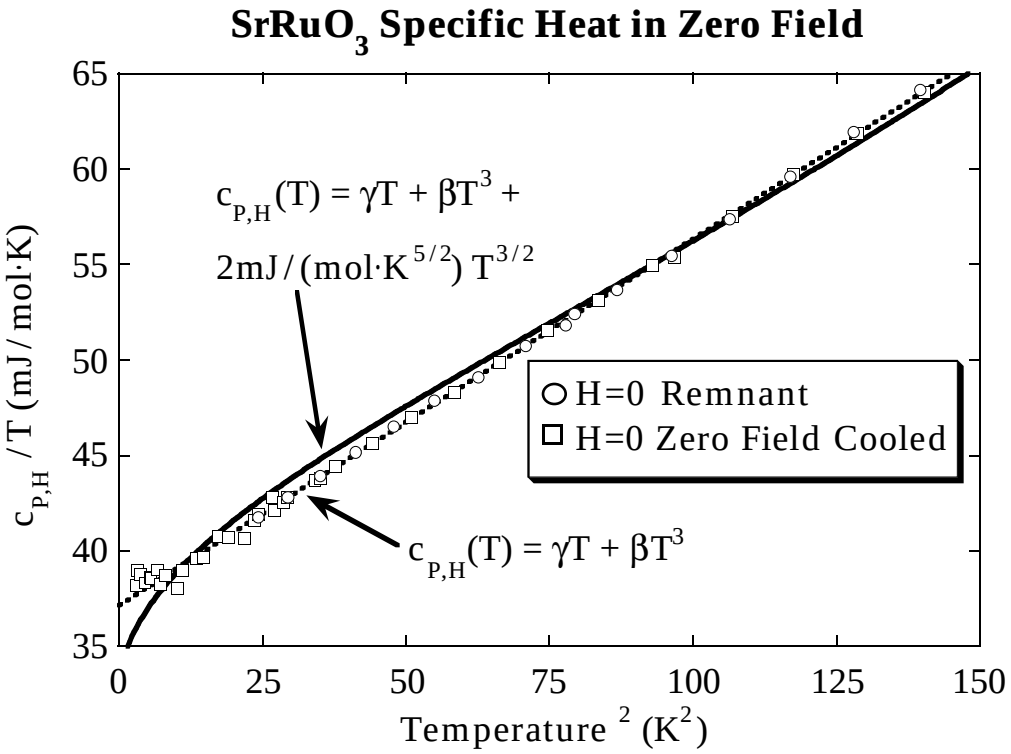

Figure B- 2. Zero field heat capacity data fit with two free parameters, γ and β. Solid line, including the $T^{3/2}$ contribution expected theoretically for spin waves (see text). Dashed line, without any $T^{3/2}$ contribution.

paramagnetic spins will give a low temperature upturn but should also be noticeable as Curie paramagnetism in magnetization measurements.

Adding a positive $T^{3/2}$ term to the model for the specific heat, as expected for pure spin wave excitations (3.2.2.2.8) [95], does not improve the fit (Figure B- 2). Assuming 6 nearest neighbors, spin 1, and T_C = 163 to determine J, this value is A = 2mJ mol^{-1} K$^{-5/2}$. Previous magnetization measurements on thin films suggest that this term is correct within a factor of 2 [186]. Using a functional form of $\gamma T + AT^{3/2} + \beta T^3$, the coefficient A is less than 1.2 (0 T zfc), 2.5 (8 T), and 0.6 (0 T rem) mJ mol^{-1} K$^{-5/2}$ for each of the three data sets in

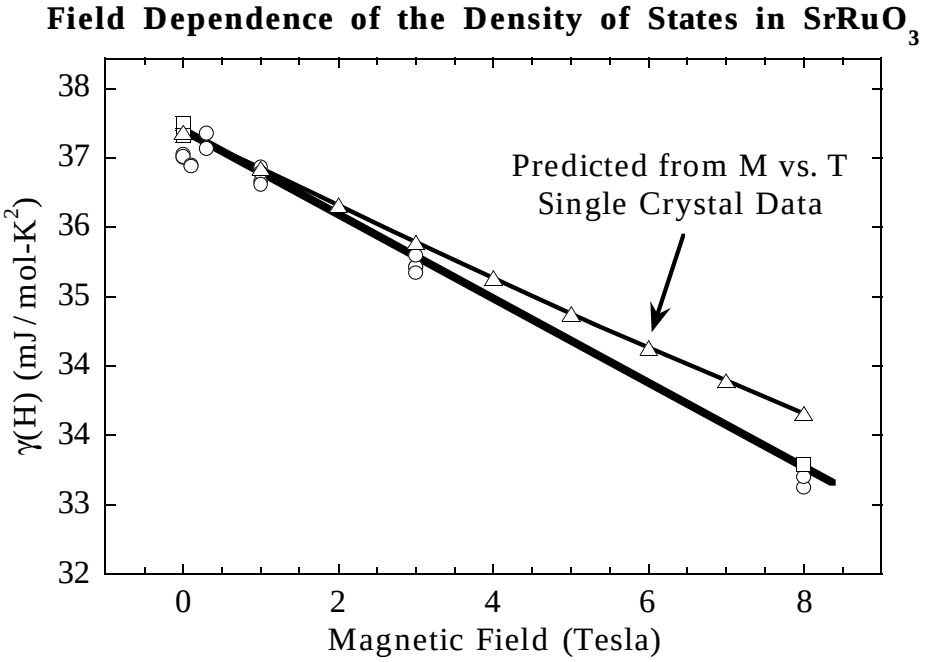

Figure B- 3. The linear term of the heat capacity γ as a function of magnetic field. Each circle is from a single $c_{P,H}$ datum between 4.3 and 5 K with phonons subtracted: $\gamma(H) = (c_{P,H}(T) - \beta T^3)/T$ with $\beta = 0.191$ mJ/mol·K^4. $\gamma(H)$ for each square was determined by fitting 15-20 data points between 6 and 12 K to: $c_{P,H}(T) = \gamma T + \beta T^3$. The triangles are calculated from the magnetization data of a single crystal.

Figure 3 at the 90% statistical confidence level. The $T^{3/2}$ term in Fe and Ni is quite small but has nevertheless been extracted from the heat capacity data [200-202].

The linear-T term, γ, is significantly depressed in an 8 T magnetic field. The inset to Figure B- 1 shows the difference between the zero-field cooled data in zero field and each of the other two data sets, plotted as $\Delta c / T$. The data

taken in 0 T after application of an 8 T field (circles) shows that the zero-field data are not hysteretic. On this plot of $\Delta c/T$, the 8 T data (diamonds) show that the only observed change in the specific heat is a decrease in the linear-T term.

To further understand the field dependence of γ, specific heat points between 4 K and 5 K at several intermediate fields were also taken. These data are shown in Figure B- 3 (open circles) as $\gamma(H) = (c(T,H) - \beta T^3)/T$ using the value of β measured at 0 T and 8 T. On the same plot, the open squares indicate the fitted value of γ from the three data sets in Figure B- 1. Figure B- 3 shows that the coefficient of the linear-T term in the specific heat decreases approximately linearly with applied magnetic field, H.

To summarize, the specific heat between 3 and 13 K can be described by $c(T,H) = (\gamma - \gamma' H)T + \beta T^3$.

Although the magnetization of polycrystalline $SrRuO_3$ is irreversible, the measured heat capacity is not. Therefore, the heat capacity originates from processes reversible with respect to a magnetic field, showing that the entropy associated with random domains is negligible. In this sense, the heat capacity is a better thermodynamic measure of the low-lying excitations. The magnetic field dependence of the heat capacity and the magnetization are related by the following Maxwell relation:

$$\left(\frac{\partial C_H}{\partial H}\right)_T = T\left(\frac{\partial^2 M}{\partial T^2}\right)_H \qquad (1)$$

According to equation 1, the first derivative of the heat capacity with respect to field gives information about the second derivative of the magnetization with respect to temperature. This relation is generally valid for an isotropic system as long as there are no irreversible processes involved and no PV work is done. Equation 1 is actually three equations since H and M

are vectors. Thus for an ideal, simple experiment, the sample would be very soft magnetically (no magnetic hysteresis) and the magnetic field would be aligned in the magnetic easy direction to keep M and H parallel. If possible, the magnetic and heat capacity experiments should be done on the same sample in the same direction; although, in principle different samples should give the same result since both M and C_P in a reversible sample should not depend on the microstructure. In order to use equation 1 to relate the reversible magnetization from the measured specific heat, it is assumed that effects due to the field dependence of the magnetocrystalline anisotropy are insignificant.

The simplest spin wave model (section 3.2.2.2.8) predicts a $T^{3/2}$ dependence of the magnetization at low temperatures:

$$\frac{M(H,T)}{M(H,0)} \approx 1 - \left(\frac{T}{\Theta_{\frac{3}{2}}(H)} \right)^{\frac{3}{2}} \tag{2}$$

with $\Theta_{3/2} \approx 2.42 T_C$ = 400K [95, 186] for $SrRuO_3$. Corrections due to $H \neq 0$ and $T > 0$ can also be calculated [95]. The Stoner/Wohlfarth theory of magnetism (section 3.2.2.2.2) [81] predicts a somewhat different temperature dependence:

$$\frac{M(H,T)}{M(H,0)} \approx 1 - \left(\frac{T}{\Theta_2(H)} \right)^2 \tag{3}$$

($\Theta_2 \approx \sqrt{2} T_C$ = 231K for $SrRuO_3$) due to single (*k*-space) particle excitations.

The Maxwell relation together with the observed magnetic field dependence of the specific heat above 4 K, $\gamma \sim HT$, implies that the second derivative of the magnetization with respect to temperature, $\left(\frac{\partial^2 M}{\partial T^2} \right)_H$, is a constant. This result is consistent with the dominant T^2 temperature dependence of the reversible discussed above.

In order to make quantitative comparisons between the specific heat data and the magnetization data, equation 1 can be integrated with respect to H

from $H = 0$ to $H = \Delta H$. Since magnetization data is not available at all fields, the integral is approximated to a finite sum with step size dH:

$$\frac{\Delta C_H(T)}{T\Delta H} \approx \frac{dH}{\Delta H}\sum_{n=0}^{\Delta H/dH-1}\frac{\partial^2 M(n\cdot dH,T)}{\partial T^2} \tag{4}$$

where $\Delta C_H(T)=C_H(T,H=\Delta H)-C_H(T,H=0)$. The two simplest physically plausible temperature dependencies of the reversible magnetization, T^2 (equation 3) or $T^{3/2}$ (equation 2), each correspond to a simple temperature dependence of $\frac{\Delta C_H(T)}{T\Delta H}$:

$$\frac{M(H,T)}{M(H,0)} \approx 1-\left(\frac{T}{\Theta_2(H)}\right)^2 \Rightarrow \frac{\Delta C_H(T)}{T\Delta H} = \frac{-2dH}{\Delta H}\sum_{n=0}^{\Delta H/dH-1}\frac{M(n\cdot dH,0)}{\Theta_2(n\cdot dH)^2} = Const. < 0 \tag{5}$$

$$\frac{M(H,T)}{M(H,0)} \approx 1-\left(\frac{T}{\Theta_{\frac{3}{2}}(H)}\right)^{\frac{3}{2}} \Rightarrow \frac{\Delta C_H(T)}{T\Delta H} = \frac{-3dH}{4\sqrt{T}\Delta H}\sum_{n=0}^{\Delta H/dH-1}\frac{M(n\cdot dH,0)}{\Theta_{\frac{3}{2}}(n\cdot dH)^{\frac{3}{2}}} \propto \frac{-1}{\sqrt{T}} \tag{6}$$

Since the $\frac{\Delta c_{P,H}(T)}{T\Delta H}$ data of Figure B- 1 are constant in temperature, these data can be fit to a T^2 dependence of the magnetization, but not by $T^{3/2}$ alone. Using the parameters from the fits to the magnetization data of single crystal $SrRuO_3$ (Appendix A) gives quantitative values for the constant $\frac{\Delta c_{P,H}(T)}{T\Delta H}$ = -0.42 mJ mol^{-1} K^{-2} T^{-1} (about 20% less than that measured by $\frac{\Delta c_{P,H}(T)}{T\Delta H}$). A field independent $\Theta_2(H)$ is consistent with γ decreasing linearly with magnetic field. Since the two measurements are on different types of samples with different orientations; nevertheless this result illustrates the potential for this method.

The failure to observe a $T^{3/2}$ dependence does not necessarily eliminate the possibility of spin wave excitations in $SrRuO_3$; the data could be easily described within the spin wave theory (section 3.2.2.2.8) if additional

corrections are included. Using these corrections, the predicted magnetization fit to T^n will necessarily have $n \approx 2$ to fit the data.

At low temperatures and finite fields, a gap is expected in the spin wave dispersion [95], predicting an exponential temperature dependence of the magnetization at the lowest temperatures. Combined with the spin wave $n = 3/2$, $H = 0$ form, this effectively increases n [97]. The inclusion of this gap affects the predicted $\frac{\Delta c_{P,H}(T)}{T\Delta H}$ primarily at low temperatures, as is shown in (Figure 3-11).

The linear term in the specific heat γ is usually interpreted in terms of the (nonmagnetic) electronic contribution to the specific heat. Spin fluctuations are predicted to enhance γ in ferromagnetic and nearly ferromagnetic metals [84]. For $\gamma = \gamma^{ele}(1 + \lambda^{e\text{-}p} + \lambda^{mag})$ where γ^{ele} is γ expected from band calculations and $\lambda^{e\text{-}p} \approx 0.5$ is the electron-phonon mass enhancement [176]. From these values $\lambda^{mag} \approx 3.1$, the electron-spin fluctuation mass enhancement, is estimated. Theoretically, in the presence of a magnetic field, spin fluctuations are suppressed and therefore γ will decrease [203, 204]. From equation 1, these spin fluctuations which cause the field dependence of γ are required to give a T^2 dependence of the magnetization, thereby unifying the two interpretations for the field dependence of γ. A decrease in the coefficient of the linear-T term, γ, has also been observed in the weak itinerant ferromagnets $ZrZn_2$ and Sc_3In [199, 205] (which also show a T^2 dependence of the magnetization).

In conclusion, the magnetic field dependence of the heat capacity provides a useful method for studying the low-lying excitations, and for determining the temperature dependence of the magnetization *via* thermodynamic relations. For a ferromagnetic substance the magnetic field dependence of the low-temperature heat capacity can be a more sensitive probe of the low-

energy magnetic excitations than the saturation magnetization, particularly for polycrystalline samples with large magnetocrystalline anisotropy such as $SrRuO_3$.

Like the magnetization measurements, the heat capacity measurements can be well described by a decrease in the magnetization proportional to T^n where $n \approx 2$. This can be understood by any of three mechanisms. First, if the corrections are included in the spin wave theory then an effective $n > 3/2$ is predicted. Second, single particle excitations are present. Third, the excitations interact (requiring a more generalized description [85]) to give an effective exponent $n \approx 2$.

The same phenomena can also be interpreted as a spin fluctuation enhancement of the electronic specific heat, which can be suppressed by a magnetic field.

The help of K. A. Moler for the heat capacity measurements is greatly appreciated.

References

[1] G. H. Jonker and H. van Santen, Physica **16**, 337 (1950).

[2] H. van Santen and G. H. Jonker, Physica **16**, 599 (1950).

[3] E. O. Wollan and W. C. Koehler, Phys. Rev. **100**, 545 (1955).

[4] J. Volger, Physica **20**, 49 (1954).

[5] J. B. Goodenough and J. M. Longo, in *Landolt-Börnstein Tabellen* (Springer, Berlin, 1970), Vol. III/4a.

[6] C. Zener, Phys. Rev. **82**, 403 (1951).

[7] P. W. Anderson and H. Hasegawa, Phys. Rev. **100**, 675 (1955).

[8] P.-G. deGennes, Phys. Rev. **118**, 141 (1960).

[9] S. Zhang, J. Appl. Phys. **79**, 4542 (1996).

[10] A. J. Millis, P. B. Littlewood, and B. I. Shraiman, Phys. Rev. Lett. **74**, 5144 (1995).

[11] A. J. Millis, B. I. Shraiman, and R. Mueller, Phys. Rev. Lett. **77**, 175 (1996).

[12] A. J. Millis, B. I. Shraiman, and R. Mueller, Phys. Rev. B **53**, 8434 (1996).

[13] C. B. Alcock, R. C. Doshi, and Y. Shen, Solid State Ionics **51**, 281 (1992).

[14] T. Kobayashi, H. Takizawa, T. Endo, T. Sato, and M. Shimada, J. Solid State Chem. **92**, 116 (1991).

[15] H. Taguchi, M. Nagao, and M. Shimada, J. Solid State Chem. **97**, 476 (1992).

[16] J. A. M. van Roosmalen, J. P. P. Huijsmans, and L. Plomp, Solid State Ionics **66**, 279 (1993).

[17] A. Hammouche, E. J. L. Schouler, and M. Henault, Solid State Ionics **28-30**, 1205 (1988).

[18] H. L. Ju, C. Kwon, Q. Li, R. L. Greene, and T. Venkatesan, Appl. Phys. Lett. **65**, 2108 (1994).

[19] J. Cho, M. Gomi, and M. Abe, Jpn. J. Appl. Phys. **29**, 1686 (1990).

[20] K. C. Chanara, T. Ohno, M. Kasai, and Y. Kozono, Appl. Phys. Lett. **63**, 1990 (1993).

[21] R. von Helmolt, J. Wecker, B. Holzapfel, L. Schultz, and K. Samwer, Phys. Rev. Lett. **71**, 2331 (1993).

[22] S. Jin, T. H. Tiefel, M. McCormack, R. A. Fastnacht, R. Ramesh, and L. H. Chen, Science **264**, 413 (1994).

[23] G. C. Xiong, Q. Li, H. L. Ju, S. N. Mao, L. Senapati, X. X. Xi, R. L. Greene, and T. Venkatesan, Appl. Phys. Lett. **66**, 1427 (1995).

[24] J. Z. Sun, L. Krusin-Elbaum, S. S. P. Parkin, and G. Xiao, Appl. Phys. Lett. **67**, 2726 (1995).

[25] S. Jin, M. McCormack, T. H. Tiefel, and R. Ramesh, J. Appl. Phys. **76**, 6929 (1994).

[26] S. Kawamata, N. Kobayashi, M. Ikebe, and Y. Muto, Physica B **148**, 130 (1987).

[27] G. C. Xiong, Q. Li, H. L. Ju, R. L. Greene, and T. Venkatesan, Appl. Phys. Lett. **66**, 1689 (1995).

[28] N. Furukawa, J. Phys. Soc. Jpn. **65**, 1174 (1996).

[29] P. Schiffer, A. P. Ramirez, W. Bao, and S.-W. Cheong, Phys. Rev. Lett. **75**, 3336 (1995).

[30] C. M. Varma, Phys. Rev. B **54**, 7328 (1996).

[31] N. Furukawa, J. Phys. Soc. Jpn. **63**, 3214 (1994).

[32] S. Zhang and Z. Yang, J. Appl. Phys. **79**, 7398 (1996).

[33] M. S. Hillery, D. Emin, and N.-L. H. Liu, Phys. Rev. B **38**, 9771 (1988).

[34] D. Emin, M. S. Hillery, and N.-L. H. Liu, Phys. Rev. B **35**, 641 (1987).

[35] A. World and K. Dwight, J. Solid State Chem. **88**, 229 (1990).

[36] R. J. Bouchard and J. L. Gillson, Mat. Res. Bull. **7**, 873 (1972).

[37] R. Czaya, Z. anorg. allgem. Chem. **375**, 61 (1970).

[38] G. J. Snyder and A. Simon, Angew. Chem. Int. Ed. **33**, 689 (1994).

[39] G. J. Snyder and A. Simon, J. Amer. Chem. Soc. **117**, 1996 (1995).

[40] G. J. Snyder and A. Simon, Adv. Mater. **6**, 374 (1994).

[41] G. J. Snyder, M. Gelabert, and F. J. DiSalvo, J. Solid State Chem. **113**, 355 (1994).

[42] G. J. Snyder, M. E. Badding, and F. J. DiSalvo, Inorg. Chem. **31**, 2107 (1992).

[43] F. J. DiSalvo, Current Opinion in solid state materials science **1**, 241-9 (1996).

[44] G. J. Snyder and A. Simon, Zeit. Kryst. **209**, 384 (1994).

[45] G. J. Snyder and A. Simon, Zeit. Natur. B **49**, 189 (1994).

[46] G. J. Snyder and A. Simon, J. Chem. Soc. (London) Dalton Trans. **1994** (1994).

[47] G. J. Snyder, H. Borrmann, and A. Simon, Zeit. Kryst. **209**, 458 (1994).

[48] G. J. Snyder and A. Simon, J. Alloys Compounds **223**, 65 (1995).

[49] T. M. Hayes and J. B. Boyce, in *Solid State Physics*, edited by H. Ehrenreich, F. Seitz and D. Turnbull (Academic, New York, 1982), Vol. 37, p. 173.

[50] J. Antoszewski, D. J. Seymour, and L. Faraone, J. Electr. Mater. **24**, 1255 (1995).

[51] F. M. Smits, The Bell System Technical Journal **1958**, 711 (1958).

[52] L. J. van der Pauw, Philips Res. Repts. **13**, 1 (1958).

[53] L. J. van der Pauw, Philips Tech. Rev. **20**, 220 (1958).

[54] D. K. C. MacDonald, in *Handbuch der Physik*, edited by S. Flügge (Springer Verlag, Berlin, 1953), Vol. 14.

[55] J. M. Ziman, *Electrons and Phonons* (Clarendon press, Oxford, 1960).

[56] N. W. Ashcroft and N. D. Mermin, *Solid State Physics* (Saunders, 1976).

[57] H. Frölich, Adv. Phys. **3**, 325 (1954).

[58] D. Emin and T. Holstein, Ann. Phys. **53**, 439 (1969).

[59] D. Emin, Phys. Rev. B **3**, 1321 (1971).

[60] T. Holstein, Ann. Phys. (N.Y.) **8**, 343 (1959).

[61] D. Emin and N. L. H. Liu, Phys. Rev. Lett. **42**, 71 (1979).

[62] D. Emin and N. L. H. Liu, Phys. Rev. B **27**, 4788 (1983).

[63] L. Friedman and T. Holstein, Ann. Phys. (N.Y.) **21**, 494 (1963).

[64] T. Holstein, Ann. Phys. (N.Y.) **8**, 325 (1959).

[65] D. Emin, Adv. Phys. **24**, 305 (1975).

[66] Shewmon, *Diffusion in solids* (Minerals Metals and Materials Society, Warrendale, PA, 1989).

[67] P. A. Cox, *The Electronic Structure and Chemistry of Solids* (Oxford University Press, Oxford, 1987).

[68] J. B. Goodenough, Progress in Solid State Chemistry **5, Chap. 4** (1970).

[69] N. F. Mott, *Conduction in non-Crystalline Materials* (Clarendon Press, Oxford, 1993).

[70] N. F. Mott and E. A. Davis, *Electronic Processes in non-Crystalline Materials* (Clarendon Press, Oxford, 1979).

[71] B. I. Shklovskii and A. L. Efros, *Electronic Properties of Doped Semiconductors* (Springer-Verlag, 1984).

[72] M. I. Klinger, J. Phys. C: Solid State Phys. **9**, 3955 (1976).

[73] L. Klein, J. S. Dodge, C. H. Ahn, G. J. Snyder, T. H. Geballe, M. R. Beasley, and A. Kapitulnik, Phys. Rev. Lett. **77**, 2774 (1996).

[74] A. P. Ramirez, P. Schiffer, S.-W. Cheong, C. H. Chen, W. Bao, T. T. M. Palstra, P. L. Gammel, D. J. Bishop, and B. Zegarski, Phys. Rev. Lett. **76**, 3188 (1996).

[75] Y. Tomioka, A. Asamitsu, Y. Moritomo, H. Kuwahara, and Y. Tokura, Phys. Rev. Lett. **74**, 5108 (1995).

[76] P. W. Selwood, *Magnetochemistry* (Interscience, New York and London, 1956).

[77] M. M. Schieber, *Experimental Magnetochemistry* (Wiley, New York, 1967).

[78] S. Shoner and J. Kovacs, (unpublished).

[79] T. Moriya, J. Magn. Magn. Mater. **100**, 261-271 (1991).

[80] E. C. Stoner, Proc. R. Soc. London Ser. A: **165**, 372 (1938).

[81] D. M. Edwards and E. P. Wohlfarth, Proc. R. Soc. London Ser. A: **303**, 127-137 (1968).

[82] E. C. Stoner, Acta Metallurgica **2**, 259 (1954).

[83] E. P. Wohlfarth, Phys. Lett. **3**, 17 (1962).

[84] T. Moriya, *Spin Fluctuations in Itinerant Electron Magnetism* (Springer Verlag, 1985).

[85] T. Moriya, in *Metallic Magnetism, Topics in Current Physics*, edited by H. Capellman (Springer, Berlin, 1987), Vol. 42, p. 15-55.

[86] G. G. Lonzarich and L. Taillefer, J. Phys. C: Solid State Phys. **18**, 4339 (1985).

[87] K. Adachi, K. Sato, and M. Takeda, J. Phys. Soc. Jpn. **26**, 631 (1969).

[88] E. P. Wohlfarth, in *Ferrmagnetic Materials*, Vol. 1, p. 1-70.

[89] W. Bao, C. Broholm, G. Aeppli, J. M. Honig, P. Metcalf, and S. F. Travino, Phys. Rev. B **54**, 3726 (1996).

[90] B. Widom, J. Chem. Phys. **43**, 3898 (1965).

[91] K. Makoshi and T. Moriya, J. Phys. Soc. Jpn. **38**, 10 (1975).

[92] R. Anders and W. von Hörsten, Phys. Dat. **20** (1984).

[93] M. Seeger, H. Kronmuller, and H. J. Blythe, J. Magn. Magn. Mater. **139**, 312 (1995).

[94] R. M. White and T. H. Geballe, in *Solid State Physics*, edited by H. Ehrenreich, F. Seitz and D. Turnbull (Academic, New York, 1979), Vol. 15.

[95] F. Keffer, in *Handbuch der Physik* (Springer Verlag, Berlin, 1966), Vol. 18, p. 1.

[96] G. S. Rushbrooke and P. J. Wood, Mol. Phys. **1**, 257 (1958).

[97] V. N. Smolyaninova, J. J. Hamilton, R. L. Greene, Y. M. Mukovskii, S. G. Karabashev, and A. M. Balbashov, Phys. Rev. B **55** (1997).

[98] M. Itoh, I. Natori, S. Kubota, and K. Motoya, J. Phys. Soc. Jpn. **63**, 1486 (1994).

[99] J. A. Mydosh, *Spin Glasses* (Taylor & Francis, London, 1993).

[100] H. Y. Hwang, S.-W. Cheong, P. G. Radaelli, M. Marezio, and B. Batlogg, Phys. Rev. Lett. **75**, 914 (1995).

[101] A. H. Morrish, *The Physical Principles of Magnetism* (John Wiley & Sons, New York, 1965).

[102] K. A. Moler, Thesis (Stanford University, 1995)

[103] G. J. Snyder, R. Hiskes, S. DiCarolis, M. R. Beasley, and T. H. Geballe, Phys. Rev. B **53**, 14434 (1996).

[104] H. L. Ju, J. Gopalakrishnan, J. L. Peng, G. C. X. Qi. Li, T. Venkatesan, and R. L. Greene, Phys. Rev. B **51**, 6143 (1995).

[105] R. von Helmolt, J. Wecker, K. Samwer, and K. Bärner, J. Magn. Magn. Mater. **151**, 411 (1995).

[106] I. O. Troyanchuk, JETP **75**, 132 (1992).

[107] T. M. Perekalina, T. A. Sivokon', S. A. Cherezyan, and I. É. Lipin'ski, Sov. Phys. Solid State **31**, 1524 (1989).

[108] R. Mahendiran, A. K. Raychaudhuri, A. Chainani, D. D. Sarma, and S. B. Roy, Appl. Phys. Lett. **66**, 233 (1995).

[109] S. E. Lofland, S. M. Bhagat, H. L. Ju, G. C. Xiong, T. Venkatesan, and R. L. Greene, (1995).

[110] M. Domínguez, S. M. Bhagat, S. E. Lofland, J. S. Ramachandran, G. C. Xiong, H. L. Ju, R. L. Greene, and T. Venkatesan, EuroPhysics **32**, 349 (1995).

[111] M. Domínguez, S. E. Lofland, S. M. Bhagat, A. K. Raychaudhuri, H. L. Ju, T. Venkatesan, and R. L. Greene, Sol. State Comm. **97**, 193 (1996).

[112] K. Kubo and N. Ohata, J. Phys. Soc. Jpn. **33**, 21 (1972).

[113] A. Urushibara, Y. Moritomo, T. Arima, G. Kido, and Y. Tokura, Phys. Rev. B **51**, 14103 (1995).

[114] M. F. Hundley, M. Hawley, R. H. Heffner, Q. X. Jia, J. J. Neumeier, J. Tesmer, J. D. Thompson, and X. D. Wu, Appl. Phys. Lett. **67**, 860 (1995).

[115] M. F. Hundley, J. J. Neumeier, R. H. Heffner, Q. X. Jia, X. D. Wu, and J. D. Thompson, J. Appl. Phys. **79**, 4535 (1995).

[116] J. Z. Liu, I. C. Chang, S. Irons, P. Klavins, R. N. Shelton, K. Song, and S. R. Wasserman, Appl. Phys. Lett. **66**, 3218 (1995).

[117] I. Mannari, Prog. Theor. Phys. **22**, 335 (1959).

[118] I. A. Campell and A. Fert, in *Ferromagnetic Materials*, edited by E. P. Wholfarth (North Holland, New York, 1982), Vol. 3, Chap. 9.

[119] K. Udea and T. Moriya, J. Phys. Soc. Jpn. **39**, 605 (1975).

[120] A. H. Thompson, Phys. Rev. Lett. **35**, 1786 (1975).

[121] Y. Tokura, A. Urushibara, Y. Moritomo, T. Arima, A. Asamitsu, G. Kido, and N. Furukawa, J. Phys. Soc. Jpn. **63**, 3931 (1994).

[122] Y. Tokura, A. Urushibara, Y. Moritomo, A. Asamitsu, Y. Tomioka, T. Arima, and G. Kido, J. Mater. Sci. Eng. B **31**, 187 (1995).

[123] N. F. Mott and E. A. Davis, *Electronic Processes in non-Crystalline Materials* (Clarendon Press, Oxford, 1971).

[124] J. M. D. Coey, M. Viret, and L. Ranno, Phys. Rev. Lett. **75**, 3910 (1995).

[125] M. E. Fisher and J. S. Langer, Phys. Rev. Lett. **20**, 665 (1968).

[126] S. C. Gausepohl, M. Lee, K. Char, and C. B. Eom, Phys. Rev. B **52**, 3459 (1995).

[127] P. G. deGennes and J. Friedel, J. Phys. Chem. Solids **4**, 71-77 (1958).

[128] C. Haas, Phys. Rev. **168**, 531 (1968).

[129] Methfessel and Mattis, in *Handbuch der Physik* (Springer Verlag, Berlin, 1968), Vol. 18, p. 389.

[130] S. von Molnár and S. Methfessel, J. Appl. Phys. **38**, 959 (1967).

[131] S. von Molnár, I. Terry, T. Penney, and P. Becla, Physica B **197**, 151 (1994).

[132] V. J. Folen and G. H. Stauss, in *Landolt-Börnstein Tabellen* (Springer, Berlin, 1970), Vol. III/4b.

[133] M. Böhm and A. Scharmann, in *Landolt-Börnstein Tabellen*, edited by O. Madelung (Springer, Berlin, 1982), Vol. III/17h.

[134] H. von Philipsborn, L. Treitinger, and M. Rubenstein, in *Landolt-Börnstein Tabellen* (Springer, Berlin, 1978), Vol. III/12b.

[135] M. R. Oliver, J. O. Dimmock, A. L. McWhorter, and T. B. Reed, Phys. Rev. B **5**, 1078 (1972).

[136] J. M. DeTeresa, M. R. Ibarra, J. Garcia, J. Blasco, C. Ritter, P. A. Algarabel, C. Marquina, and A. delMoral, Phys. Rev. Lett. **76**, 3392 (1996).

[137] G. J. Snyder, C. Booth, F. Bridges, R. Hiskes, S. DiCarolis, M. R. Beasley, and T. H. Geballe, Phys. Rev. B (1997).

[138] R. Pauthenet, J. Appl. Phys. **29**, 253 (1958).

[139] H. Yoshizawa, H. Kawano, Y. Tomioka, and Y. Tokura, Phys. Rev. B **52**, 13145 (1995).

[140] I. S. Jacobs, J. Phys. Chem. Solids **11**, 1 (1959).

[141] I. S. Jacobs, J. Phys. Chem. Solids **15**, 54 (1960).

[142] A. S. Yermolenko, Phys. Met. Metallogr. **50(4)**, 57 (1980).

[143] Z. Jirak, S. Krupicka, Z. Simsa, M. Dlouha, and S. Vratislav, J. Magn. Magn. Mater. **53**, 153 (1985).

[144] J. J. Melero, F. Bartolome, J. Bartolome, and R. Burriel, J. Magn. Magn. Mater. (unpublished).

[145] Z. Jirak, S. Krupicka, V. Nekvasil, E. Pollert, G. Villeneuve, and F. Zounova, J. Magn. Magn. Mater. **15-18**, 519 (1980).

[146] D. C. Worledge, G. J. Snyder, R. Hiskes, S. DiCarolis, M. R. Beasley, and T. H. Geballe, J. Appl. Phys. **80**, 5158 (1996).

[147] P. Shuk, L. Tichonova, and U. Guth, Solid State Ionics **68**, 177 (1994).

[148] H. Taguchi, M. Nagao, and M. Shimada, J. Solid State Chem. **82**, 8 (1989).

[149] V. Ambegaokar, B. I. Halperin, and J. S. Langer, Phys. Rev. B **4**, 2612 (1971).

[150] G. J. Snyder, R. Hiskes, S. DiCarolis, M. R. Beasley, and T. H. Geballe, Appl. Phys. Lett. **69**, 4254 (1996).

[151] S. J. L. Billinge, R. G. DiFrancesco, G. H. Kwei, J. J. Neumeier, and J. D. Thompson, Phys. Rev. Lett. **77**, 715 (1996).

[152] R. P. Sharma, G. C. Xiong, C. Kwon, R. Ramesh, R. L. Greene, and T. Venkatesan, Phys. Rev. B **54**, 10014 (1996).

[153] P. G. Radaelli, M. Marezio, H. Y. Hwang, S.-W. Cheong, and B. Batlogg, Phys. Rev. B **54**, 8992 (1996).

[154] C. H. Booth, F. Bridges, G. J. Snyder, and T. H. Geballe, Phys. Rev. B (1996).

[155] C. W. Searle and S. T. Wang, Can. J. Phys. **48**, 2023 (1970).

[156] Y. X. Jia, L. Lu, K. Khazeni, V. H. Crespi, A. Zettl, and M. L. Cohen, Phys. Rev. B **52**, 9147 (1995).

[157] L. D. Landau and E. M. Lifshitz, *Electrodynamics of Continuous Media* (Pergamon, Oxford, 1984).

[158] J. O'Donnell, M. Onellion, M. S. Rzchowski, J. N. Eckstein, and I. Bozovic, Phys. Rev. B (1996).

[159] J. N. Eckstein, I. Bozovic, J. O'Donnell, M. Onellion, and M. S. Rzchowski, Appl. Phys. Lett. (1996).

[160] G. Bergmann, Phys. Today **August 1979**, 25 (1979).

[161] J. E. Nunez-Regueiro and A. M. Kadin, Appl. Phys. Lett. **68**, 2747 (1996).

[162] J. Inoue and S. Maekawa, Phys. Rev. Lett. **74**, 3407 (1995).

[163] N. Furukawa, J. Phys. Soc. Jpn. **64**, 3164 (1995).

[164] N. Furukawa, J. Phys. Soc. Jpn. **64**, 2734 (1995).

[165] S. Yamaguchi, H. Taniguchi, H. Takagi, T. Arima, and Y. Tokura, J. Phys. Soc. Jpn. **64**, 1885 (1995).

[166] M. Jaime, M. B. Salamon, M. Rubinstein, R. E. Treece, J. S. Horwitz, and D. B. Chrisey, Phys. Rev. B **54**, 11914 (1996).

[167] R. H. Heffner, L. P. Lee, M. F. Hundley, J. J. Neumeier, G. M. Luke, K. Kojima, B. Nachumi, Y. J. Uemura, D. E. MacLaughlin, and S.-W. Cheong, Phys. Rev. Lett. **77**, 1869 (1996).

[168] J. F. Mitchell, D. N. Argyriou, C. D. Potter, J. D. Jorgensen, D. G. Hinks, and S. D. Bader, Mat. Res. Soc. Symp. Proc. **453** (1996).

[169] J. F. Mitchell, (unpublished).

[170] Lynn, Phys. Rev. Lett. **76**, 4046 (1996).

[171] P. G. Radaelli, D. E. Cox, M. Marezio, S.-W. Cheong, P. E. Schiffer, and A. P. Ramirez, Phys. Rev. Lett. **75**, 4488 (1995).

[172] J. L. García-Muñoz, M. Suaaidi, J. Fontcuberta, and J. Rodríguez-Carvajal, Phys. Rev. B **55**, 34 (1997).

[173] Y. Noro and S. Miyahara, J. Phys. Soc. Jpn. **27**, 518 (1969).

[174] M. Shikano, T.-K. Huang, Y. Inaguma, M. Itoh, and T. Nakamura, Sol. State Comm. **90**, 115 (1994).

[175] J. J. Neumeier, A. L. Cornelius, and J. S. Schilling, Physica B **198**, 324 (1994).

[176] P. B. Allen, H. Berger, O. Chauvet, L. Forro, T. Jarlborg, A. Junod, B. Revaz, and G. Santi, Phys. Rev. B **53**, 84393 (1996).

[177] C. W. Jones, P. D. Battle, and P. Lightfoot, Acta Ctyst. **C45**, 365 (1989).

[178] J. M. Longo, P. M. Raccah, and J. B. Goodenough, J. Appl. Phys. **39**, 1327 (1968).

[179] A. Callaghan, C. W. Moeller, and R. Ward, Inorg. Chem. **5**, 1572 (1966).

[180] D. J. Singh, J. Appl. Phys. **79** (1996).

[181] A. Kanbayasi, J. Phys. Soc. Jpn. **41**, 1876 (1976).

[182] A. Kanbayasi, J. Phys. Soc. Jpn. **41**, 1879 (1976).

[183] A. Kanbayasi, J. Phys. Soc. Jpn. **44**, 89 (1978).

[184] W. Bensch, H. W. Schmalle, and A. Reller, Solid State Ionics **43**, 171 (1990).

[185] B. D. Cullity, *Introduction to Magnetic Materials* (Addison-Wesley, Reading, Massachusetts, 1972).

[186] L. Klein, J. S. Dodge, T. H. Geballe, A. Kapitulnik, A. F. Marshall, L. Antognazza, and K. Char, Appl. Phys. Lett. **66**, 2427 (1995).

[187] L. Klein, (unpublished).

[188] A. H. Bobeck, *Magnetic Bubbles* (Elsevier, New York, 1975).

[189] R. Pauthenet, in *High Field Magnetism*, edited by M. Date (North-Holland, 1983), p. 77.

[190] B. E. Argyle, S. H. Charap, and E. W. Pugh, Phys. Rev. **132**, 2051 (1963).

[191] A. T. Aldred and P. H. Froehle, Int. J. Magn. **2**, 195-203 (1972).

[192] A. T. Aldred, Phys. Rev. B **11**, 2597 (1975).

[193] E. P. Wohlfarth and P. F. DeChatel, Physica **48**, 477-485 (1970).

[194] J. Takeuchi and Y. Masuda, J. Phys. Soc. Jpn. **46**, 468 (1979).

[195] S. M. Hayden and C. C. Paulsen, Physica B **166**, 201 (1990).

[196] J. J. Neumeier, private communication.

[197] P. M. Levy, Phys. Rev. **170**, 595 (1968).

[198] P. M. Levy and D. P. Landau, J. Appl. Phys. **39**, 1128 (1968).

[199] K. Ikeda and K. A. Gschneider, J. Magn. Magn. Mater. **30**, 273 (1983).

[200] J. A. Rayne and W. R. G. Kemp, Phil. Mag. **1**, 918 (1956).

[201] J. A. Rayne and B. S. Chandrasekhar, Phys. Rev. **122**, 1714 (1961).

[202] M. Dixon, F. E. Hoare, T. M. Holden, and D. E. Moody, Proc. R. Soc. London Ser. A: **285**, 561 (1965).

[203] S. Shioda, Y. Takahashi, and T. Moriya, J. Phys. Soc. Jpn. **57**, 3146 (1988).

[204] P. Hertel, J. Appel, and D. Fay, Phys. Rev. B **22**, 534 (1980).

[205] K. Ikeda and M. Yoshizawa, Physica B **165-166**, 203 (1990).